Spatially and temporally resolved mass distribution in PEMFCs studied by *operando* analytical methods

A Doctoral Thesis

Presented to Special Doctoral Program for Green Energy Conversion Science and Technology

Faculty of Engineering

The Integrated Graduate School of Medicine, Engineering, and Agricultural Science

University of Yamanashi

March, 2021

G18DTE06 Yu Kakizawa

Contents

Chapter 3 Oscillation mechanism based on *operando* $p(O_2)$ measurement using optical probes

Chapter 1

General Introduction

1.1 Background

Electricity is indispensable to our lives. Home appliances, communication tools, PCs, and other tools used both in private life and at work require electricity. However, conventional power generation methods emit CO_2, a greenhouse gas. Before the 21st century came, against the global warming, the Japanese government had been promoting nuclear power stations with no CO_2 emission [1]. In 2010, the ratio of the nuclear power in the total production of electricity in the country reached around 20%. However, in 2011, the Great East Japan Earthquake caused a meltdown of a nuclear reactor, and the safety of the nuclear power generation was questioned. In 2017, the ratio of the nuclear power in the production of electricity dropped to 3.1%. 80.8% of the Japan's power generation became from oil, coal, and LNG, therefore, the CO_2 emission accordingly and abruptly increased. Under this situation, the promotion of renewable energies, such as hydropower, wind power, solar power, and geothermal power, have been accelerated. However, the generation of renewable energies, based on the variable natural environment, is unstable [1]. Therefore, the social storage system of electricity is needed for the averaging of renewable energies. In order to solve this disadvantage, the rechargeable battery is commonly used, but it is not suitable for large-scale and long-term storages of electricity for various reasons, such as huge mass and volume and self-discharge. To compensate the use of batteries, hydrogen has been attracting attention in recent years. Hydrogen can be stably stored as a gas or liquid, and the transportation is relatively easy. At the present stage, hydrogen is generally produced from fossil fuels and biomass. Therefore, the CO_2

emission is inevitable upon the use of hydrogen. The ultimate clean system with zero CO_2 emission can be realized by the electrolysis of water to produce hydrogen, eventually used for the production of electricity [2].

Fuel cell is a device that converts chemical energy into electrical energy by supplying air (oxygen) and hydrogen first developed in 1839 [3]. Now, fuel cell is classified into four types: polymer electrolyte fuel cell (PEFC), solid oxide fuel cell (SOFC), molten carbonate fuel cell (MCFC), and phosphoric acid fuel cell (PAFC). The advantages of fuel cells are high efficiency, high power density (compactness), zero CO_2 emission, and quietness. Among the four types, PEFCs are used for vehicles and at residences because of low-temperature operation (50-100 ˚C), high energy conversion (40-60%), nearly zero pollutants, and simple structure [4,5]. Residential fuel cell system, "ENE-FARM" was released from Panasonic Co., Ltd in 2009. The use of ENE-FARM, cogenerating the electricity and heat for hot water, results in the conversion efficiency of 95%. Fuel cell vehicle (FCV), "MIRAI" started to sale by Toyota Motor Corp. in 2014, followed by "CLARITY FUEL CELL" by Honda Motor Co., Ltd. in 2016. At the end of 2020, a new type "MIRAI" was at the market.

1.2 Polymer electrolyte fuel cells (PEFCs)

Among fuel cells, PEFCs most attract attention and are actively studied. As shown in Fig. 1-1, a single PEFC is constructed by sandwiching a membrane electrode assembly (MEA) with flow channels, current collector plates, and end plates on both sides. MEA is composed of a polymer electrolyte membrane (PEM), catalyst layers (CLs), and gas diffusion layers (GDLs).

For membranes, proton exchange membranes (PEMs) and anion exchange membranes

(AEMs) exist. PEMs, perfluorosulfonated acid such as Nafion® (E. I. Du Pont Nemours & Company, Inc.) as an example, are widely used due to their high conductivity and mechanical stability at varies temperatures and humidities. PEFCs using PEMs are named proton exchange membranes fuel cells (PEMFCs). In recent years, AEMs have been actively studied due to the larger reaction rate for the oxygen reduction reaction (ORR) and to the potential use of non-precious metals. Fuel cells using AEMs are named anion exchange membranes fuel cells (AEMFCs).

Pt catalyst is highly dispersed and supported on a carbon support with high specific surface area, such as TEC10E50E of TANAKA KIKINZOKU KOGYO K. K. The Pt particle size is 2-5 nm. An ionomer binder is mixed with a Pt catalyst for the transfers of ions from/to the electrolyte membrane to/from Pt catalyst surface.

Carbon paper and carbon cloth are generally used, such as 29BC of SIGRACET® of SGL Carbon Group Co., Ltd., Germany and TGP-H060 of Toray Industries, Japan. In addition to gas permeability and conductivity, chemical and mechanical strengths are required. Polytetrafluoroethylene (PTFE) is added to the carbon fiber to improve water removal property. Micro porous layer (MPL) is commonly added at a GDL surface.

At the anode, hydrogen atoms are oxidized to protons (H^+) to produce electrons (e^-) on the catalyst surface as shown in equation 1-1. The protons and electrons move to the cathode through the PEM and the external electrical load, respectively. At the cathode, the ORR occurs as shown in equation 1-2. The overall reaction is shown in equation 1-3.

Anode reaction:	$H_2 \rightarrow 2\ H^+ + 2\ e^-$	(eq. 1-1)
Cathode reaction:	$1/2\ O_2 + 2\ H^+ + 2\ e^- \rightarrow H_2O$	(eq. 1-2)
Overall reaction:	$H_2 + 1/2\ O_2 \rightarrow H_2O$	(eq. 1-3)

The equilibrium cell voltage of a single PEMFC defined by the Nernst equation (eq. 1-4) is 1.23 V at the ambient temperature and pressure (25 ºC, 100 kPa).

Nernst equation: $$E = \frac{-\Delta \bar{g}(T)}{2 \cdot F} + \frac{R \cdot T}{2 \cdot F} \cdot \ln \frac{p_{H_2} \cdot p_{O_2}^{0.5}}{p_{H_2O}} \quad \text{(eq. 1-4)}$$

where $\bar{g}$ is the molar Gibbs free energy (J mol^{-1}), T temperature (K), F Faraday constant (96485 C mol^{-1}), R universal gas constant (J mol^{-1} K^{-1}), p partial pressure.

However, operating cell voltage of a single PEMFC is lower due to the overvoltages both at the anode and the cathode such as activation, ohmic, and concentration overvoltages as shown in Fig. 1-2. To reduce these overvoltages, catalyst, PEM and mass transport had been studied extensively. Understanding mass transport inside a PEMFC is especially important to improve the power generation performance and the durability in high current density. The mechanisms of various phenomena observed in the PEMFCs are also connected with mass transport. For analyzing mass transport, along with numerical simulations, *operando* analytical methods are essential using cells with practical structures.

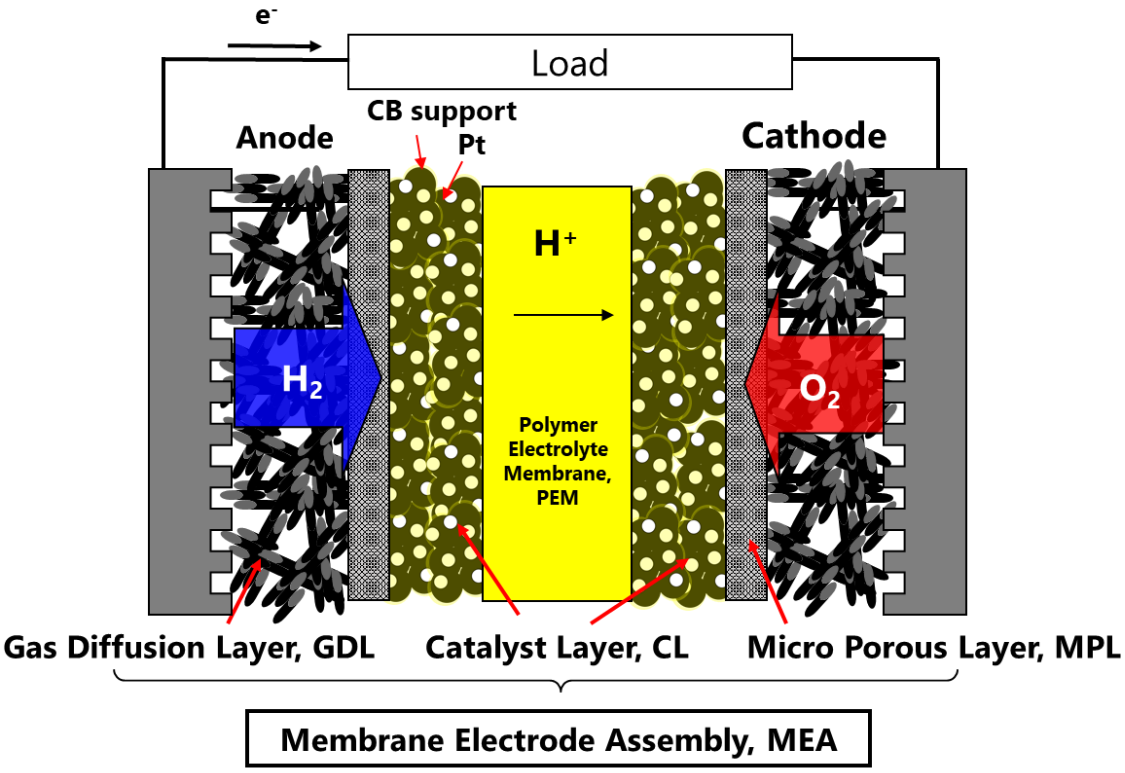

Fig. 1-1 Schematic illustration of PEMFC.

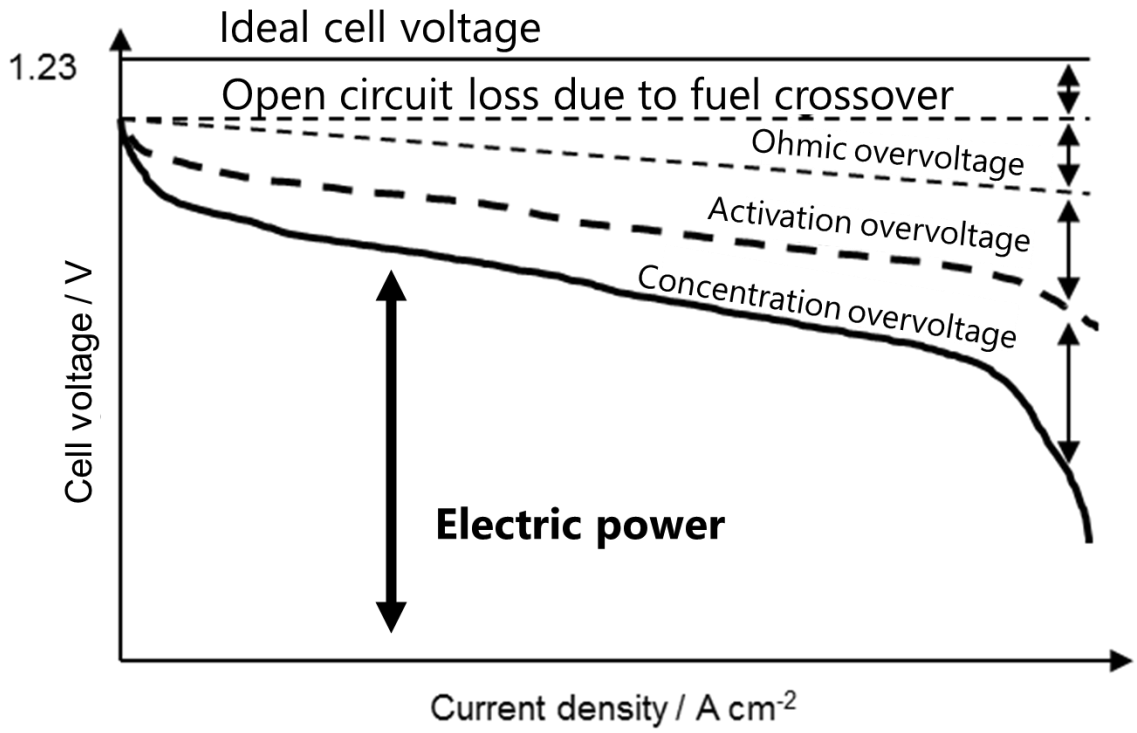

Fig. 1-2 Schematic illustration of typical polarization curve of single PEMFC.

1.3 Various *operando* measurements of reaction distribution inside proton exchange membrane fuel cell (PEMFC)

As described in chapter 1.1, the PEMFCs have already been commercialized. However, improving cell performance, durability and cost reduction are still mandatory for widely use. In order to improve the PEMFC performance and durability, understanding the inhomogeneous reaction distributions during power generation is necessary. Therefore, it is important to reveal the chemical (H_2, O_2, H_2O, CO_2, H_2O_2, etc.) and physical (temperature, current density, gas flux, pressure etc.) parameters inside the PEMFC during power generation. In order to obtain these parameters, *in-situ* and *operando* measurement techniques, including visualization, are investigated. Among these parameters, the distribution and generation of liquid water have been successfully visualized by magnetic resonance imaging [6–8], optical observation [9–17], X-ray imaging [18–23], and neutron radiography imaging [24–34]. To achieve an understanding of the distribution of oxygen partial pressure ($p(O_2)$) inside the fuel cell during cell operation, the group in the University of Yamanashi developed a nondestructive real-time/space visualization system [14,35–42]. On the other hand, numerical simulation of these parameter inside the PEMFC have been studied to elucidate the transport phenomena with various cell component and under different operating conditions [43–45]. The temperature distribution affects chemical kinetics and mass transports inside a PEMFC. The temperatures inside the MEAs have been measured by a thin film sensor [46], thermoelectric sensor [47], and thermograph [48]. The current density at the MEA in a single cell is also monitored to optimize the operating conditions and the cell designs with segmented current collectors [49–58] and by magnetomyography [59,60]. The degradation of carbon support material caused by start/stop cycle has been obtained by

the visualization of CO_2 [61]. Additionally, the numerical simulations of these parameters are conducted to elucidate the mass/energy transports with various cell components and under different operating condition [62,63]. The numerical simulation is widely used, especially in industrial fields. Although the numerical simulation is a powerful technique, unique phenomena have generally not been treated. Therefore, the experimental elucidation of those unique phenomena is very important.

1.4 Mechanisms to be investigated during power generation

A large number of gas starvation (hydrogen and oxygen) experiments have confirmed that the carbon support of the catalyst layer is corroded to CO_2 [64–66]. Gas starvation leads to the coalescence or loss of the catalyst on/from the electrode. The gas starvations are categorized to local gas starvation and overall gas starvation. In the overall gas starvation, the gas supply cannot meet the stoichiometric requirements of the fuel cell, as a result of which the external characteristics cannot follow the load changes due to the controller failure, variable load amplitude, or variable load speed during the load change. In the local gas starvation, uneven gas distribution on the surface of the electrode mainly due to the speed of gas transmission lagging behind the speed of current change, and there is no apparent performance on the external characteristics such as the output voltage of the fuel cell. The local gas starvation is frequently observed in the process of load change and is the main reason for the lifespan decay.

The hydrogen starvation is notorious as a major cause of the degradation of the CLs by the corrosion of carbon supports [67–69]. The reactions during the hydrogen starvation are $2H_2O \rightarrow O_2 + 4H^+ + 4e^-$ and $C + 2H_2O \rightarrow CO_2 + 4H^+ + 4e^-$, resulting in the most hazardous degradation of the catalytic layer. The corrosion of the carbon support can

result in the electrical isolation of the platinum particles, which accelerates the agglomeration of the catalyst particles; the catalyst surface area is accordingly reduced.

The oxygen starvation has also been studied since the 2000s as a cause of irreversible catalyst degradation [70]. When oxygen starvation occurs at the cathode, the possible abnormal reaction formula is $2H^+ + 2e^- \rightarrow H_2$. Especially in PEMFC stacks, this abnormal reaction is enhanced to the hydrogen pumping. The existence of both hydrogen and oxygen at the same electrode surface lead to the degradation of catalyst and support material. The increasing concentrations of hydrogen even represent a flammability risk.

The stability of PEMFCs during power generation is one of the most important issues especially for the operation at high current densities. Under certain conditions, the cell voltage and the current density become unstable and even fluctuated because of the instability of the reactions inside PEMFCs. Since the excess liquid water in a cell is one of the main sources of instability, the water management during power generation has been extensively studied [71,72]. The oscillation phenomena during power generation have been also reported in running PEMFCs [73–76]. The water generated by the power generation is continuously removed outside the fuel cell through the GDLs. However, when the water generation is too large, the flooding is inevitable. Materials must be developed, and the operating conditions and the cell configurations must be optimized.

For catalyst support, carbon is generally used. Recently, as alternative supports, ceramic materials have been developed, mainly for improving the durability [77–79]. Different support materials naturally change the chemical/physical properties of the catalyst layer, such as electroconductivity, mass transportation, and binder adsorption. The change in those parameters leads to the fuel cell performance [77–85]. Understanding the distributions of chemical/physical parameters with different supports is thus very

important for developing new supports.

1.5 Objectives

As described above, many unclear phenomena exist during power generation by PEMFCs. In my research, three selected mechanisms are analyzed by using *operando* measurement systems for $p(O_2)$ and liquid water by developing new analytical apparatuses.

In Chapter 2, oxygen starvation is focused on. The current-voltage (I-V) performance suddenly decreased as the oxygen concentration/partial pressure decreased even under a high oxygen utilization. The $p(O_2)$ distribution on the GDL during power generation is visualized in low oxygen concentration by using oxygen sensitive dye for the explanation of the mechanism.

In Chapter 3, a new mechanism of oscillation phenomena is presented. To elucidate the oscillation mechanism, a novel *operando* system for $p(O_2)$ by using optical probes was developed.

In Chapter 4, a liquid water distribution inside single PEMFCs were visualized by neutron imaging. The current-voltage (I-V) performance of a PEMFC with Pt catalyst formed on Nb-doped SnO_2 support (Pt/Nb-SnO_2) was lower than that with Pt/CB. The imaging of liquid water shed light on the difference in performances. Finally, these results are summarized, and suggest a feasibility of this study in Chapter 5.

References

[1] Japan's Energy White paper 2020, by "Ministry of Economy, Trade and Industry". https://www.enecho.meti.go.jp/about/whitepaper/2020pdf/

[2] Hydrogen energy white paper by New Energy and Industrial Technology Developed Organization (NEDO). https://www.nedo.go.jp/library/ne_hakusyo_index.html

[3] W. R. Grove, Philosophical Magazine and Journal of Science 13:84 (1838) 430–431.

[4] B. L. Yi, Fuel Cell-Principle, Technology & Application, Chemical Industry Press 238 (2003) 161–162.

[5] K. Rajashekara, A. K. Rathore, Electr. Power Compon. Syst. 43 (2015) 1376–1387.

[6] S. Tsushima, K. Teranishi, S. Hirai, Electrochem. Solid-State Lett. 7 (2004) A269–A272.

[7] S. Tsushima, T. Nanjo, S. Hirai, ECS Trans. 11 (2007) 435–443.

[8] K. W. Feindel, S. H. Bergens, R. E. Wasylishen, J. Power Sources 173 (2007) 86–95.

[9] K. Tüber, D. Pócza, C. Hebling, J. Power Sources 124 (2003) 403–414.

[10] X. G. Yang, F. Y. Zhang, A. L. Lubawy, C. Y. Wang, Electrochem. Solid-State Lett. 7 (2004) A408–411.

[11] K. Sugiura, M. Nakata, T. Yodo, Y. Nishiguchi, M. Yamauchi, Y. Itoh, J. Power Sources 145 (2005) 526–533.

[12] K. Sugiura, T. Shiramizu, T. Yamauchi, M. Yamauchi, S. Matsuzaki, N. Kada, Y. Itoh, ECS Trans. 12 (2008) 131–138.

[13] X. Liu, H. Guo, C. Ma, J. Power Sources 156 (2006) 267–280.

[14] K. Takada, Y. Ishigami, S. Horataka, M. Uchida, Y. Nagumo, J. Inukai, H. Nishide, M. Watanabe, Electrochemistry 79 (2011) 388–391.

[15] K. Takada, Y. Ishigami, J. Inukai, Y. Nagumo, H. Takano, H. Nishide, M. Watanabe, J. Power Sources 196 (2011) 2635–2639.

[16] I. S. Hussaini, C. Wang, J. Power Sources 187 (2009) 444–451.

[17] P. K. Sinha, P. P. Mukherjee, C. Y. Wang, J. Mater. Chem. 17 (2007) 3089–3103.

[18] S. J. Lee, N. Y. Lim, S. Kim, G. G. Parl, C. S. Kim, J. Power Sources 345 (2017) 67–77.

[19] F. Y. Zhang, S. G. Advani, A. K. Prasad, M. E. Boggs, S. P. Sullivan, T. P. Beebe, Electrochim. Acta. 54 (2009) 4025–4030.

[20] T. Sasabe, S. Tsushima, S. Hirai, K. Minami, K. Yada, ECS Trans. 25 (2009) 513–521.

[21] T. Sasabe, P. Deevanhxay, S. Tsushima, S. Hirai, J. Power Sources 196 (2011) 8197–8206.

[22] J. Lee, J. Hinebaugh, A. Bazylak, J. Power Sources 227 (2013) 123–130.

[23] M. A. Hickner, N. P. Siegel, K. S. Chen, D. N. McBrayer, D. S. Hussey, D. L. Jacobson, M. Arif, J. Electrochem. Soc. 153 (2006) A902–A908.

[24] Y. S. Chen, H. Peng, D. S. Hussey, D. L. Jacobson, D.T. Tran, T. Abdel-Baset, M. Biernacki, J. Power Sources 170 (2007) 376–386.

[25] H. Markötter, I. Manke, R. Kuhn, T. Arlt, N. Kardjilov, M. P. Hentschel, A. Kupsch, A. Lange, C. Hartnig, J. Scholta, J. Banhart, J. Power Sources 219 (2012) 120–125.

[26] Y. Wu, J. I. S. Cho, X. Lu, L. Rasha, T. P. Neville, J. Millichamp, R. Ziesche, N.

Kardjilov, H. Markötter, P. Shearing, D. J. L. Brett, J. Power Sources 412 (2019) 597–605.

[27] A. Turhan, K. Heller, J. S. Brenizer, M. M. Mench, J. Power Sources 180 (2008) 773–783.

[28] A. Z. Weber, M. A. Hickner, Electrochim. Acta. 53 (2008) 7668–7674.

[29] M. A. Hickner, N. P. Siegel, K. S. Chen, D. S. Hussey, D. L. Jacobson, J. Electrochem. Soc. 155 (2008) B294–B302.

[30] M. A. Hickner, N. P. Siegel, K. S. Chen, D. S. Hussey, D. L. Jacobson, M. Arif, J. Electrochem. Soc. 155 (2008) B427–B434.

[31] H. Murakawa, T. Ueda, T. Yoshida, K. Sugimoto, H. Asano, N. Takenaka, K. Mochiki, H. Iikura, R. Yasuda, M. Matsubayashi, Nucl. Instrum. Methods. Phys. Res. A 605 (2009) 127–130.

[32] M. A. Hickner, N. P. Siegel, K. S. Chen, D. S. Hussey, D. L. Jacobson, J. Electrochem. Soc. 157 (2010) B32–B38.

[33] J. J. Gagliardo, J. P. Owejan, T. A. Trabold, T. W. Tighe, Nucl. Instrum. Methods. Phys. Res. A 605 (2009) 115–118.

[34] P. Oberholzer, P. Boillat, A. Kaestner, E. H. Lehmann, G. G. Scherer, T. J. Schmidt, A. Wokaun, J. Electrochem. Soc. 160 (2013) F659–F669.

[35] J. Inukai, K. Miyatake, K. Takada, M. Watanabe, T. Hyakutake, H. Nishide, Y. Nagumo, M. Watanabe, M. Aoki, H. Takano, Angew. Chemie. 120 (2008) 2834–2837.

[36] J. Inukai, K. Miyatake, Y. Ishigami, M. Watanabe, T. Hyakutake, H. Nishide, Y. Nagumo, M. Watanabe, A. Tanaka, Chem. Commun. (2008) 1750–1752.

[37] Y. Ishigami, K. Takada, H. Yano, J. Inukai, M. Uchida, Y. Nagumo, T. Hyakutake,

H. Nishide, M. Watanabe, J. Power Sources 196 (2011) 3003–3008.

[38] Y. Ishigami, W. Waskitoaji, M. Yoneda, K. Takada, T. Hyakutake, T. Suga, M. Uchida, Y. Nagumo, J. Inukai, H. Nishide, M. Watanabe, J. Power Sources 269 (2014) 556–564.

[39] K. Nagase, T. Suga, Y. Nagumo, M. Uchida, J. Inukai, H. Nishide, M. Watanabe, J. Power Sources 273 (2015) 873–877.

[40] K. Takanohashi, M. Uchida, A. Iiyama, J. Inukai, J. Surf. Fin. Soc. Jpn. 68 (2017) 338–343.

[41] K. Nagase, H. Motegi, M. Yoneda, Y. Nagumo, T. Suga, M. Uchida, J. Inukai, H. Nishide, M. Watanabe, ChemElectroChem. 2 (2015) 1495–1501.

[42] K. Takanohashi, T. Suga, M. Uchida, T. Ueda, Y. Nagumo, J. Inukai, H. Nishide, M. Watanabe, J. Power Sources 343 (2017) 135–141.

[43] R. M. Rao, R. Rengaswamy, Chem. Eng. Sci. 61 (2006) 7393–7409.

[44] A. Manokaran, S. Pushpavanam, P. Sridhar, J Appl Electrochem 45 (2015) 353–363.

[45] A, Jarauta, P. Ryzhakov, Arch. Comput. Methods Eng. 25 (2018) 1027–1057.

[46] S. He, M. M. Mench, S. Tadigadap, Sensors and Actuators A 125 (2006) 170–177.

[47] G. Zhang, L. Guo, L. Ma, H. Liu, J. Power Sources 195 (2010) 3597–3604.

[48] A. Nishimura, K. Shibuya, M. Takeuchi, M. Hirota, S. Kato, Y. Nakamura, H. Tachi, M. Narito, J. Therm. Sci. Technol. 4 (2009) 438–452.

[49] L. A. Shneider, S. von Danhlen, M. H. Bayer, P. Boillat, M. Hildebrandt, E. H. Lehmann, P. Oberholzer, G. G. Sherer, A. Wokaun, J. Phys. Chem. C 114 (2010) 11998–12002.

[50] U. N. Shrivastava, K. Tajiri, M. Chase, J. Power Sources 299 (2015) 189–194.

[51] U. N. Shrivastava, K. Tajiri, J. Electrochem. Soc. 163 (2016) F1072–F1083.

[52] S. J. C. Cleghorn, C. R. Derouin, M. S. Wilson, S. Gottesfeld, J. Appl. Electrochem. 28 (1998) 663–672.

[53] J. Stumper, S. A. Campbell, D. P. Wilkinson, M. C. Johnson, M. Davis, Electrochim. Acta 43 (1998) 3773–3783.

[54] C. Wieser, A. Helmbold, E. Gülzow, J. Appl. Electrochem. 30 (2000) 803–807.

[55] M. M. Mench, C. Y. Wang, M. Ishikawa, J. Electrochem. Soc. 150 (2003) A1052–A1059.

[56] N. Noponen, J. Ihonen, A. Lundblad, G. Lindbergh, J. Appl. Electrochem. 34 (2004) 255–262.

[57] F. N. Büchi, A. B. Geiger, R. P. Neto, J. Power Sources 145 (2005) 62–67.

[58] T. V. Reshetenko, A. Kulikovsky, J. Electrochem. Soc. 163 (2016) F1100–F1106.

[59] J. R. Claycomb, A. Brazdeikis, M. Le, R. A. Yarbrough, G. Gogoshin, J. H. Miller, IEEE Trans. Appl. Supercond. 13 (2003) 211–214.

[60] H. Lustfeld, M. Reiβel, B. Steffen, J. Fuel Cell Sci. Technol. 4 (2009) 474–481.

[61] Y. Ishigami, I. Maeda, K. Takada, T. Hyakutake, T. Suga, J. Inukai, M. Uchida, Y. Nagumo, H. Niside, M. Watanabe, Electrochem. Solid-State Lett. 15 (2012) B51–B53.

[62] Y. Ishigami, W. Wakitoaji, M. Yoneda, K. Takada, T. Hyakutake, T. Suga, M. Uchida, M. Watanabe, J. Power Sources 269 (2014) 556–564.

[63] K. Nagase, H. Motegi, M. Yoneda, Y. Nagumo, T. Suga, M. Uchida, J. Inukai, H. Nishide, M. Watanabe, ChemElectroChem 2 (2015) 1495–1501.

[64] Y. Bao, H. Ming, J. Automot Safe Energy 2 (2011) 91–100.

[65] Q. Shen, M. Hou, X. Yan, D. Liang, Z. Zang, L. Hao, Z. Shao, Z. Hou, P. Ming, B. Yi, J. Power Sources 179 (2008) 292–296.

[66] C. Wang, S. Wang, J. Zhang, L, Jianqiu, J. Wang, M. Ouyang, Prog Chem 27 (2015) 424–435.

[67] R. Borup, J. Meyers, B. Pivovar, Y. S. Kim, R. Mukundan, N. Garland, D. Myers, M. Wilson, F. Garzon, D. Wood, P. Zelenay, K. More, K. Stroh, T. Zawodzinski, J. Boncella, J. E. McGrath, M. Inaba, K. Miyatake, M. Hori, K. Ota, Z. Ogumi, S. Miyata, A. Nishikata, Z. Siroma, Y. Uchimoto, K. Yasuda, K. I. Kimijima, N. Iwashita, Chem. Rev. 107 (2007) 3904–3951.

[68] J. C. Kurnia, A. P. Sasmito, T. Shamim, Appl. Energy 252 (2019) 113416.

[69] Z. Y. Liu, B. K. Brady, R. N. Carter, B. Litteer, M. Budinski, J. K. Hyun, D. A. Muller, J. Electrochem. Soc. 155 (2008) B979–B984.

[70] N. Yousfi-Steiner, P. Moçotéguy, D. Candusso, D. Hissel, J. Power Sources 194 (2009) 130–145.

[71] N. Yousfi-Steiner, P. Moçotéguy, D. Candusso, D. Hissel, A. Hernandez, A. Aslanides, J. Power Sources 183 (2008) 260–274.

[72] W. Schmittinger, A. Vahidi, J. Power Sources 180 (2008) 1–14.

[73] D. G. Sanchez, D. G. Diaz, R. Hiesgen, I. Wehl, K. A. Friedrich, J. Electroanal. Chem. 649 (2010) 219–231.

[74] D. G. Sanchez, A. Ortiz, K. A. Friedrich, J. Electrochem. Soc. 160 (2013) 636–644.

[75] P. A. García-Salaberri, D. G. Sánchez, P. Boillat, M. Vera, K. A. Friedrich, J. Power Sources 359 (2017) 634–655.

[76] J. R. Atkins, S. C. Savett, S. E. Creager, J. Power Sources 128 (2004) 201–207.

[77] Y. Senoo, K. Kakinuma, M. Uchida, H. Uchida, S. Deki, M. Watanabe, RSC Adv., 4 (2014) 32180.

[78] Y. Chino, K. Taniguchi, Y. Senoo, K. Kakinuma, M. Hara, M. Watanabe, M. Uchida, J. Electrochem. Soc. 162 (2015) F736-F743.

[79] Y. Chino, K. Kakinuma, D. A. Tryk, M. Watanabe, M. Uchida, J. Electrochem. Soc. 163 (2016) F97-F105.

[80] T. Kuroki, K. Sasaki, H. Kusada, Y. Teraoka, ECS Extended abstract (2004).

[81] A. Masao, S. Noda, F. Takasaki, K. Ito, K. Sasaki, Electrochem. Solid-State Lett., 12 (2009) B119–B122.

[82] F. Takasaki, S. Matsuie, Y. Takabatake, Z. Noda, A. Hayashi, Y. Shiratori, K. Ito, K. Sasaki, J. Electrochem. Soc., 158 (2011) B1270–B1275.

[83] Y. Takabatake, Z. Noda, S. M. Lyth, A. Hayashi, K. Sasaki, Int. J. Hydrogen Energy, 39 (2014) 5074–5082.

[84] Y. Nakazato, M. Nagamine, Z. Noda, J. Matsuda, S. M. Lyth, A. Hayashi, K. Sasaki, J. Electrochem. Soc., 165 (2018) F1154–F1163.

[85] S. Matsumoto, D. Kawachino, Z. Noda, J. Matsuda, S. M. Lyth, A. Hayashi, K. Sasaki, J. Electrochem. Soc., 165 (2018) F1164–F1175.

Chapter 2

Visualization of the oxygen partial pressure during power generation with low oxygen concentrations simulating oxygen starvation

2.1 Introduction

The local reactant starvation is a condition, in which a reactant supply at the inlet is sufficient to support the load current, but the reactant concentration in some zones within the active area is near zero. The hydrogen starvation of PEMFC is well known as a major cause of the degradation of the CLs by the corrosion of carbon supports [1–3], whilst the oxygen starvation has also been studied since the 2000s as a cause of irreversible catalyst degradation [4]. To understand the oxygen starvation, previous studies were proceeded by measuring the potential and current distributions or by conducting the numerical simulation [5–8]. Yousfi-Steiner reported that an oxygen starvation induced a decrease of the cathode potential even lower than that of the equilibrium potential of a hydrogen electrode [4]. Liu et al. measured the current distribution in detail to study the starvation behavior of a single cell [9]. The fuel cell exhibited different current density distributions in the starvations of hydrogen and oxygen. In the hydrogen starvation, the current density of the starved region decrease to zero with the non-starved region little impacted, whereas the oxygen starvation made all the fuel cell influenced, and zero current regions were not observed [9]. During the production of excess liquid water inside a PEMFC, the starvation of oxygen is also known to occur [4,10–12]. At low oxygen concentration in air (< 6%), Mousa et al. reported the existence of hydrogen at the cathode in a PEMFC stack, presumably due to hydrogen pumping through the membrane [13]. During cell operation at higher current densities with a larger generation of water, the oxygen starvation could be even more important. The low stoichiometry operation is one of the factors which can

give rise to local reactant-starvation conditions.

So far, the current density distribution has been studied by using segmented single cells. When the oxygen starvation occurs at the cathode, a possible abnormal reaction at the cathode is $2H^+ + 2e^- \rightarrow H_2$ [14]. In spite of the low cathode potential reported [4], the hydrogen evolution at the cathode had not been fully discussed. For the numerical simulations during the oxygen distribution under the oxygen starvation, the hydrogen evolution due to the low potential at the cathode has neither been taken into consideration [5–8]. In other words, the $p(O_2)$ distribution having been obtained by the numerical simulations might be underestimated. The $p(O_2)$ distribution during oxygen starvation needs to be experimentally obtained.

In this chapter, a single-serpentine PEMFC was used for the power generation at the oxygen concentration ($\Phi(O_2)$) of 3, 5, and 10% in air, simulating an oxygen starvation using a single cell. The I-V performances at low oxygen concentrations of $\Phi(O_2)$ = 3 and 5% in air significantly lowered than that at $\Phi(O_2)$ = 10% at the same oxygen utilization. During power generation, the $p(O_2)$ distribution was directly visualized on the cathode side. At low $\Phi(O_2)$ and high oxygen utilization (U_{O2}), $p(O_2)$ on the GDL near the outlet of the gas flow channel was observed to be 0 kPa. The importance of the hydrogen evolution during the oxygen starvation especially in a stack is also discussed.

2.2 Experimental

2.2.1 Visualization system

Figure 2-1 shows a schematic illustration of a PEMFC for the $p(O_2)$ visualization with the gas flow channels mimicking those of the standard cell of the Japan Automobile Research Institute (JARI). For the visualization, the cathode endplate was made of

transparent quartz for the irradiation of a laser light onto and the emission from the oxygen-sensitive dye film coated on the GDL surface. The single-serpentine gas flow channels on the cathode side with a depth and width of 1 mm and a length of 1430 mm was machined through a stainless-steel plate, which was then gold plated. This plate also served as a current collector. The catalyst coated membrane consisted of a Nafion membrane (NRE 211, 25 μm thickness, DuPont, U.S.A.) sandwiched by layers of commercial Pt catalysts supported on carbon black (Pt/CB) (46.3 wt%-Pt, TEC10E50E, Tanaka Kikinzoku Kogyo K.K., Japan) mixed with a Nafion solution (5wt% Nafion D-521, DuPont). GDLs with MPLs were 29BC of SIGRACET® (SGL Carbon Group Co., Ltd., Germany). The gas flow channel on the anode side was machined into a graphite plate.

For visualizing $p(O_2)$ in the single cell during power generation, a dye solution was prepared by mixing an oxygen-sensitive complex, tetrakis[pentafluorophenylporphyrinato]platinum (PtTFPP) (absorption peaks at 400, 520, 540 nm and an emission peak at 650 nm as shown in Fig. 2-2) and a poly(1-trimethylsilyl-1-propyne) (polyTMSP), an oxygen permeable polymer matrix [15, 16]. Luminescence from the dye under irradiation is quenched with oxygen as shown in the Jablonski diagram shown in Fig. 2-3. The ground state of PtTFPP is excited to a singlet excited state by an excitation light. The singlet PtTFPP changes to the triplet PtTFPP through the intersystem crossing procedure. The energy is transferred to the triplet-state oxygen. Therefore, the emission intensity of PtTFPP decreases. As soon as PtTFPP returns to the ground state, triplet oxygen transits to singlet oxygen. The partial pressure of water gave no influence on the emission [17]. The influence of temperature on emission was very small, namely -0.5% K^{-1} [17]. It should be noted that the emission intensity was attenuated by the

excitation light [17, 24]. Therefore, the dye was pretreated by the laser light for the stabilization, and the $p(O_2)$ data were corrected by the decreasing coefficient of the emission when needed.

Oxygen sensitive dye solution was sprayed uniformly onto the GDL surface at the cathode flow channel to form a dye film with a thickness of approximately 2 μm [18, 19]. Figure 2-4 shows the optical setting of the visualization system. A diode laser was used for a bundled light with a wavelength of 407 nm. This blue light was diffused, guided by mirrors, and irradiated onto the dye film on the GDL in the fuel cell. The emission from the dye film inside the fuel cell was filtered (> 610 nm) and reached the charge coupled device (CCD) camera. All images were captured in a dark room.

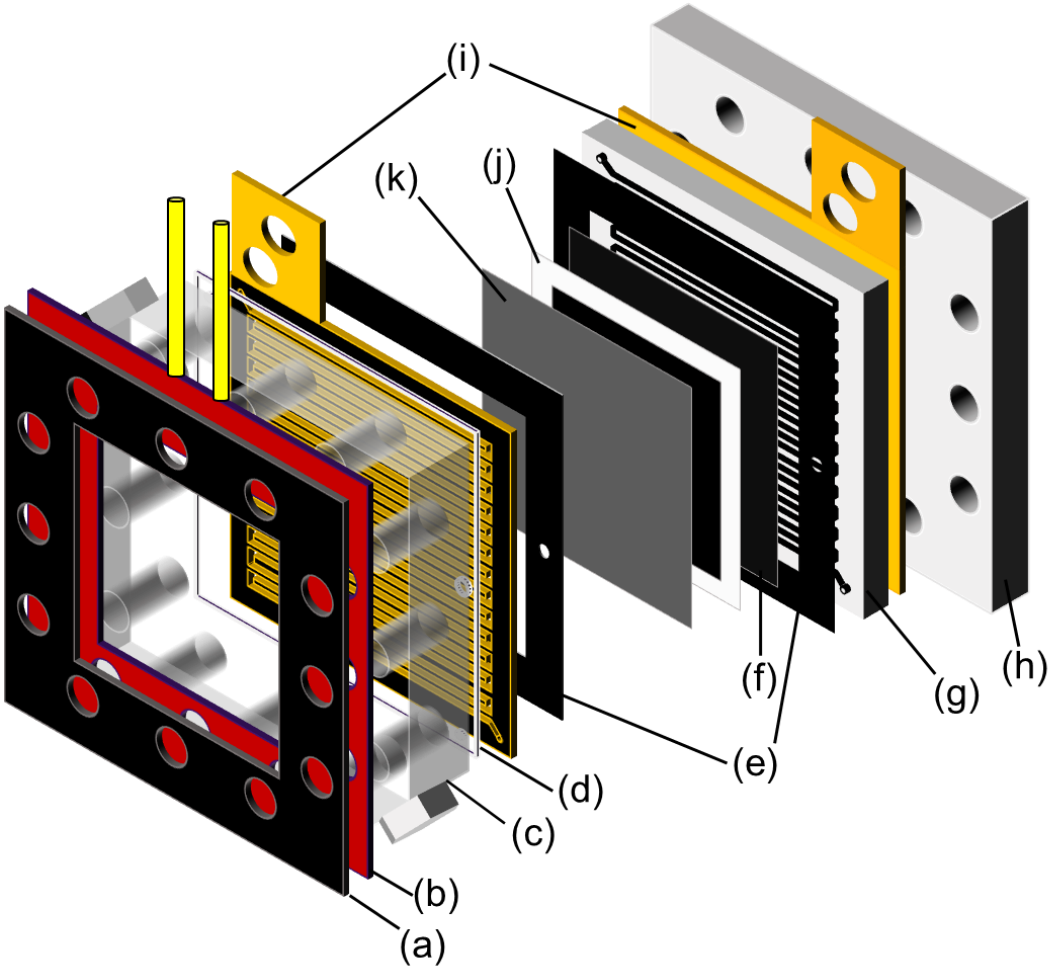

Fig. 2-1 Schematic illustration of the fuel cell. (a): cover of the cathode heater, (b): cathode heater, (c): transpatent SiO_2 endplate, (d): transparent PFA-film, (e): gasket, (f): GDL, (g): channel plate, (h): endplate, (i): current collector, (j): catalyst coated membrane (CCM), (k): GDL with dye on the surface.

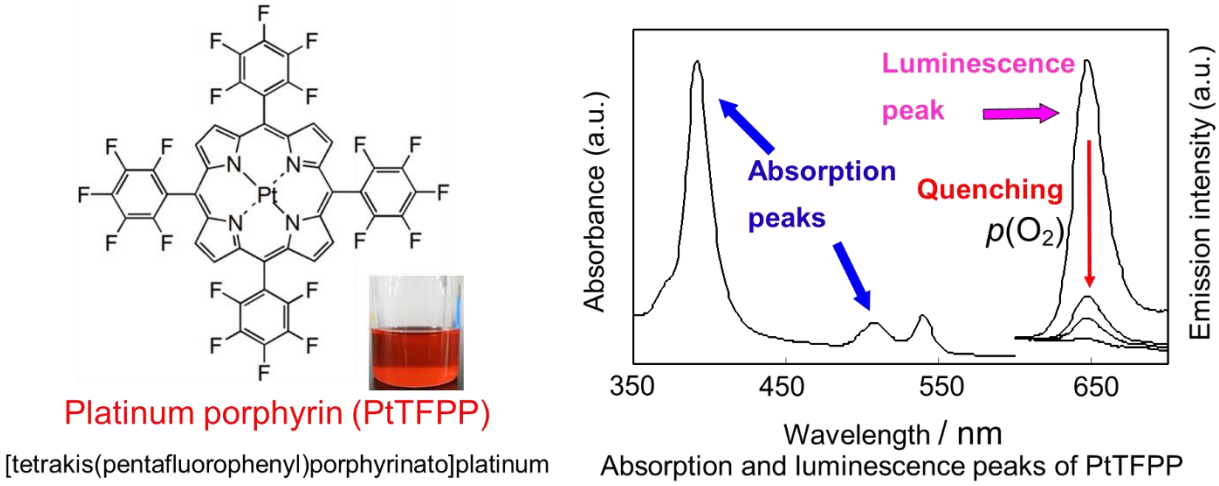

Fig. 2-2 Oxygen sensitive dye for visualizing $p(O_2)$ on the GDL surface at the cathode. (a): Structure of PtTFPP as $p(O_2)$ senser. (b): The absorttion peaks and emission peak of PtTFPP. The emission intensity of PtTFPP decreases when $p(O_2)$ increases around PtTFPP.

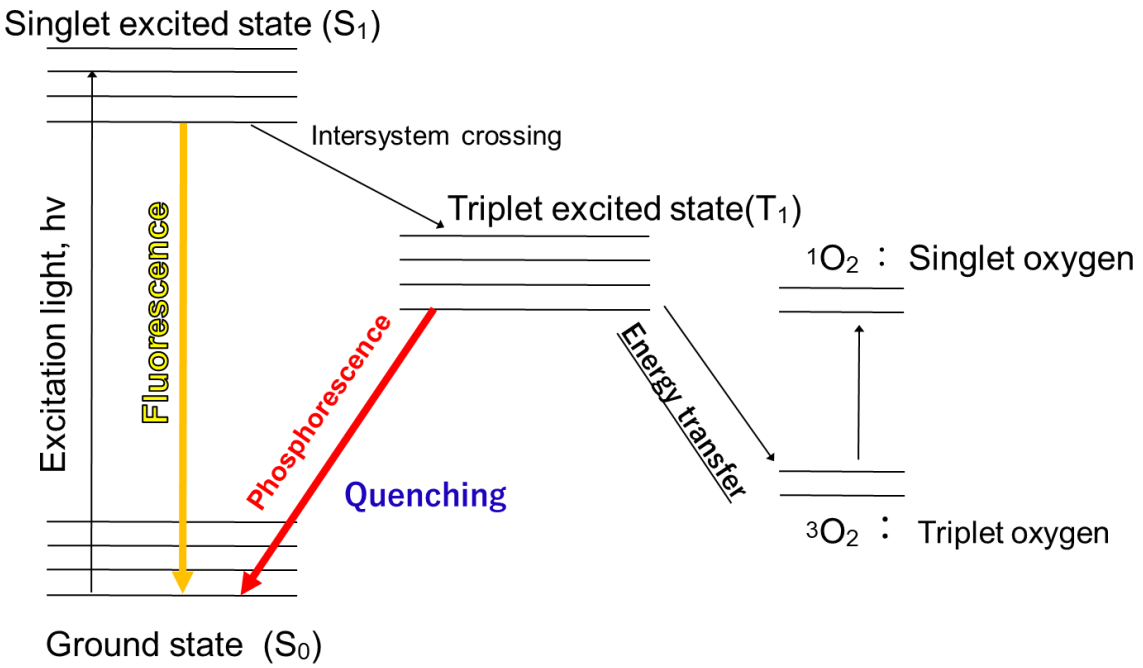

Fig. 2-3 Jablonski diagram of PtTFPP.

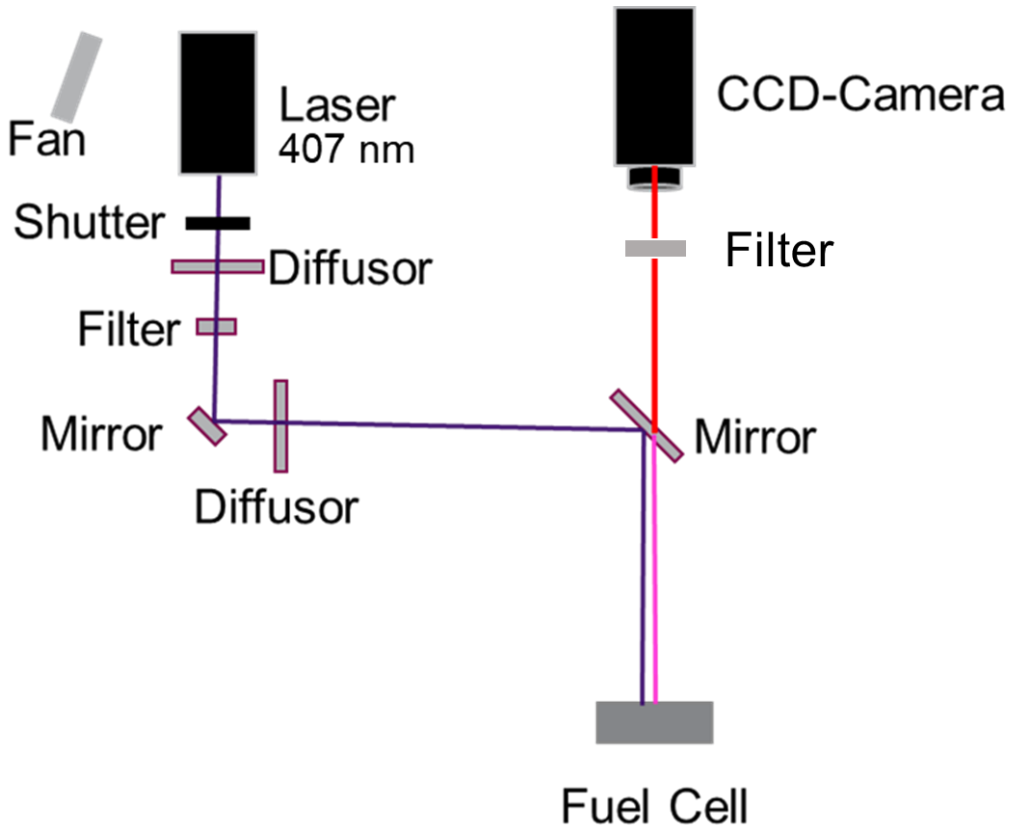

Fig. 2-4 Schematic drawing of the visualization system with a diode laser, diffusors, mirrors, a fuel cell, filters, and a CCD-camera.

2.2.2 Calibration curves for oxygen partial pressure ($p(O_2)$)

The calibration curve was assigned at each pixel of the CCD camera (250,000 pixels) before the cell operation [20, 21]. For the calibration, mixed gases of air, nitrogen, and water vapor with different $p(O_2)$ were introduced to the anode and cathode. A similar method of diluting air for studying the oxygen starvation was previously reported [13, 22]. The cell temperature and relative humidity (RH) were set to 80 ºC and 42%, respectively. The oxygen concentrations were tuned at $\Phi(O_2)$ = 10, 5, and 3%. The gas flow rate at the anode and cathode sides was set to 100 mL min^{-1} under ambient pressure. For each $\Phi(O_2)$, a different calibration curve was prepared. The calibration curve and images of each $\Phi(O_2)$ are shown in Figs. 2-5, 2-6 and 2-7.

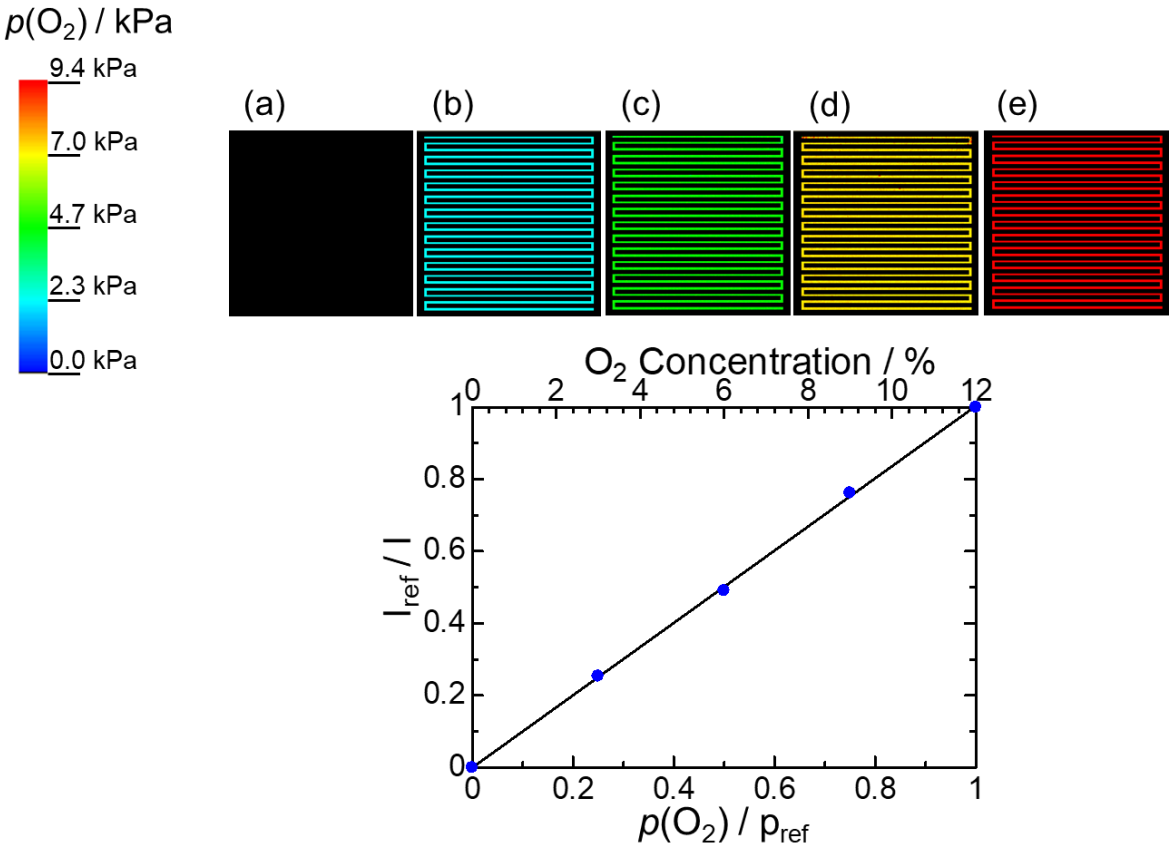

Fig. 2-5 Images at different $p(O_2)$ for calibration and averaged Stern-Volmer plots for the visualization at $\Phi(O_2)$ = 10 %.

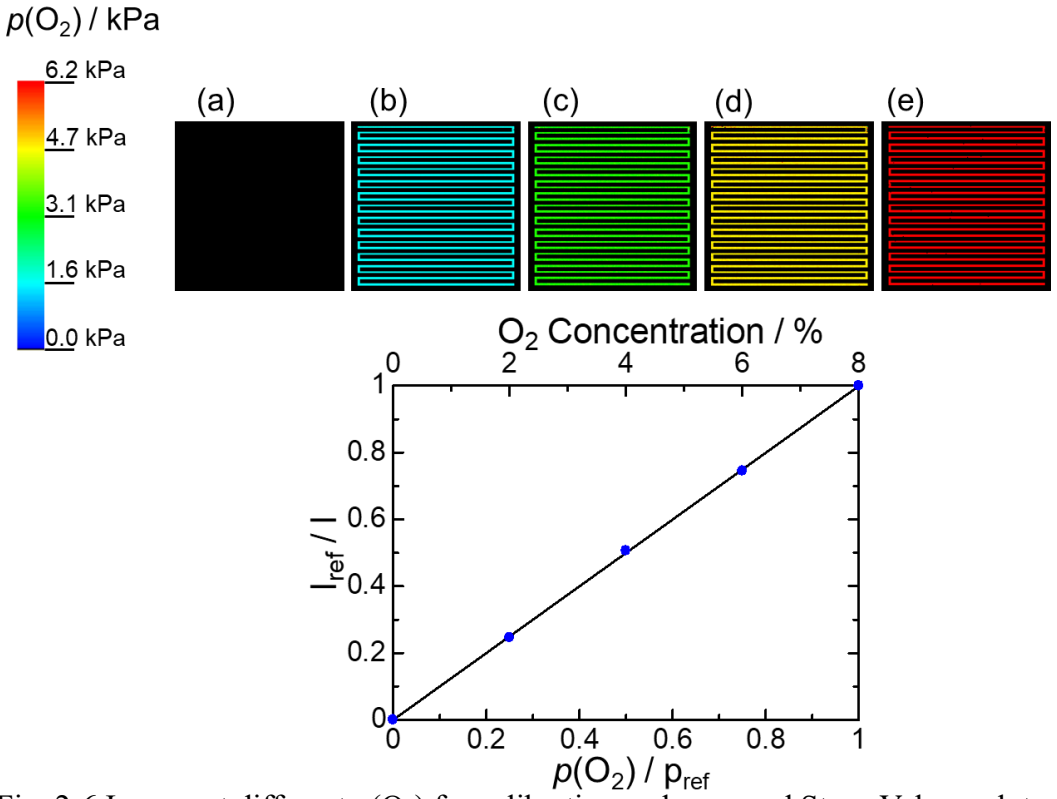

Fig. 2-6 Images at different $p(O_2)$ for calibration and averaged Stern-Volmer plots for the visualization at $\Phi(O_2) = 5\%$.

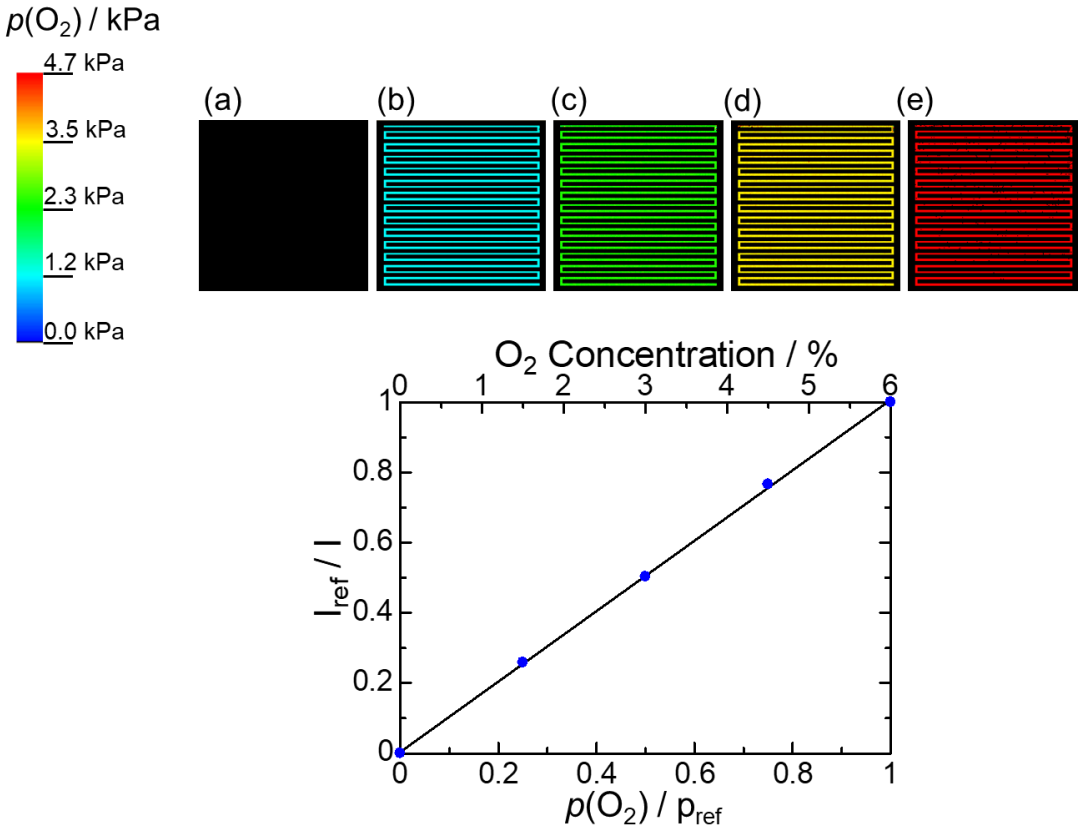

Fig. 2-7 Images at different $p(O_2)$ for calibration and averaged Stern-Volmer plots for the visualization at $\Phi(O_2) = 3$ %.

2.2.3 Power generation and cyclic voltammetry

The cell conditioning was executed at 80 °C and the above-mentioned relative humidities with an air gas flow rate of 1000 mL min^{-1} on the cathode side and a hydrogen gas flow rate of 249 mL min^{-1} on the anode side. The current density was set by a load station (LN-1000A-G7, Keisoku Giken) to 0.8 A cm^{-2}, held at least for 14 hours until the voltage changes were below 2 mV h^{-1}. The I-V curves at the different oxygen concentration were obtained at 80 °C with an air flow rate of 200 mL min^{-1} on the cathode and a hydrogen flow rate of 100 mL min^{-1} on the anode. The current density at each step set by the load station was held for 10 minutes, and the voltage was monitored.

The cyclic voltammetry (CV) on the cathode was carried out with a potentiostat (PGSTAT302N, Metrohm Autolab B.V.). The hydrogen and nitrogen gas flow rates on the anode and the cathode, respectively, were set to 200 mL min^{-1}, but the nitrogen gas was stopped during the CV measurements. The cycles were repeated between 0.075 and 1.00 V (vs. the hydrogen electrode) with a scan rate of 20 mV s^{-1}. Before the measurement, four cleaning cycles were performed.

2.2.4 $p(O_2)$ visualization

During cell operation, the cell temperature was set at 80 °C under ambient pressure. The hydrogen flow rate at the anode was 100 mL min^{-1} humidified at 88% RH. The air flow rate at the cathode was 200 mL min^{-1} at different $p(O_2)$ of 7.8 ($\Phi(O_2)$ = 10%), 3.9 ($\Phi(O_2)$ = 5%), and 2.3 kPa ($\Phi(O_2)$ = 3%), humidified at 42% RH. After changing the current density, the cell conditions were kept for 10 min before the visualization. One image was obtained in 0.8 to 10 s depending on the emission intensity. With a total exposure time of at least 60 s, the images were accumulated and averaged. The emissions of the acquired

images were converted to $p(O_2)$ using the calibration curves.

2.3 Results and discussion

2.3.1 I-V performance depending on the oxygen concentration

Figure 2-8 shows the I-V curves at $\Phi(O_2)$ = 10, 5, and 3%, where the stoichiometries of hydrogen:oxygen were 1:0.39, 1:0.19, and 1:0.11, respectively. Below 0.6 V, the cell performance suddenly decreased at all $\Phi(O_2)$. The voltage decreased rapidly at lower $\Phi(O_2)$, most significantly at $\Phi(O_2)$ = 3%; at 0.054 A cm^{-2}, the voltage abruptly dropped to 0.28 V. The starvation of oxygen had large negative influences on the I-V performance. The electrochemical surface areas obtained by CV measurements were 69.9 and 67.6 m^2 g^{-1} before and after the visualization, respectively, showing little change. Therefore, the degradation of the catalysts was negligible.

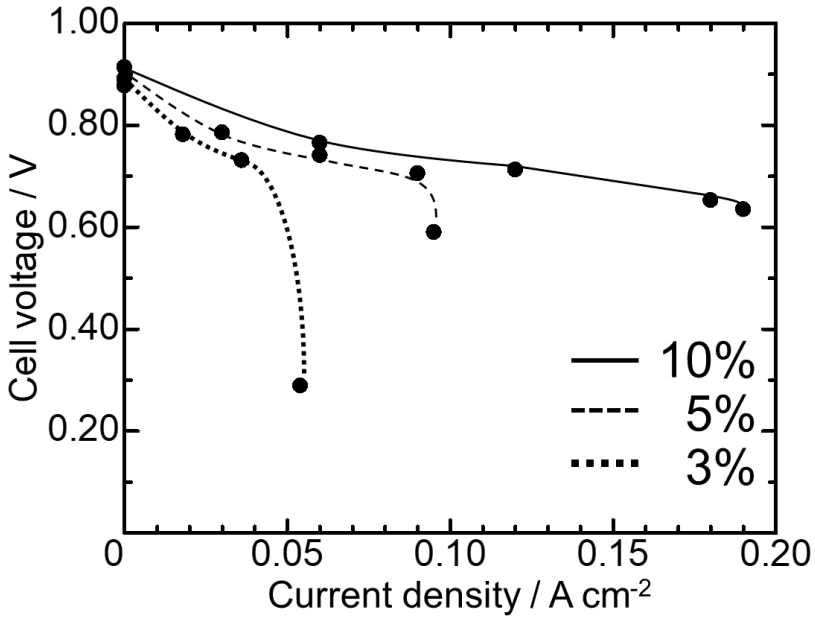

Fig. 2-8 I-V curves during cell operation at $\Phi(O_2)$ = 10, 5,and 3%. The lines are guides to the eyes.

2.3.2 Visualization images of $p(O_2)$ distribution during power generation

Figures 2-9, 2-10, and 2-11 show the $p(O_2)$ images obtained during cell operation at $\Phi(O_2)$ = 10, 5, and 3%, respectively. The top left corner in each image is of the gas inlet of the single serpentine gas flow channel, and the bottom right corner of the gas outlet. The colors shown in the images represent $p(O_2)$ on the GDL surface and are defined with the associated color bar. Figure 2-9(a) shows $p(O_2)$ at 0 A cm^{-2} (U_{O2} = 0%). The slight change in color starting from the gas inlet at the top left (ca. 9 kPa) to the gas outlet at the bottom right of the cell was caused by the pressure loss [3, 10, 18] by ca. 1 kPa of $p(O_2)$, corresponding to ca. 10 kPa of air inside the cell. Figure 2-9(b) shows the visualization image obtained at 0.06 A cm^{-2} and U_{O2} = 30.5%. A decrease in $p(O_2)$ is clearly visible by the change of color along the gas flow channel; the color along the gas flow channel changes from red-orange (ca. 9 kPa) near the gas inlet to yellow (ca. 7 kPa) near the middle of the cell, then to light green (ca. 5 kPa) near the gas outlet of the cell. Figure 2-9(c) shows the visualization images at 0.12 A cm^{-2} (U_{O2} = 60.9%). Compared to the image in Fig. 2-9(b), $p(O_2)$ in Fig. 2-9(c) decreased at an earlier stage along the gas flow channel. Figures 2-9(d) and 2-9(e) show the visualization image at 0.18 A cm^{-2} (U_{O2} = 91.4%) and 0.19 A cm^{-2} (U_{O2} = 96.5%), respectively. The decrease in $p(O_2)$ was the largest along the flow channel length at 0.19 A cm^{-2}, and $p(O_2)$ became ca. 0.3 kPa at the outlet. Figures from 2-10(a) to 2-10(e) show the images obtained at 0 (U_{O2} = 0%), 0.03 (U_{O2} = 30.5%), 0.06 (U_{O2} = 60.9%), 0.09 (U_{O2} = 91.4%), and 0.095 A cm^{-2} (U_{O2} = 96.5%), respectively, at $\Phi(O_2)$ = 5%. The U_{O2} values were set to the same as those for $\Phi(O_2)$ = 10%. The pressure loss at 0 A cm^{-2} was ca. 0.6 kPa of $p(O_2)$ or ca. 10 kPa of air. Compared with Fig. 2-9, it is understood that as the U_{O2} increased, the consumption of O_2 proceeded closer to the inlet. Figure 2-10(e) shows the image obtained at 0.095 A cm^{-2} or U_{O2} = 96.5%.

Theoretically, there should be oxygen remaining inside the gas flow channel at the outlet with ca. 0.2 kPa, but the color in the last one third along the gas flow channel changed to black, which indicated $p(O_2)$ = 0 kPa on the GDL surface. The distribution of $p(O_2)$ on the GDL at $\Phi(O_2)$ = 10% was very different from that at $\Phi(O_2)$ = 5% with the same U_{O2} of 96.5%, where $p(O_2)$ at the outlet was ca. 0.3 kPa (Fig. 2-9(e)). Therefore, nearly the last third of the CL did not generate power at $\Phi(O_2)$ = 5%, which is later discussed. As previously demonstrated by the simultaneous visualization of $p(O_2)$ on the GDL surface and on the upper gas flow channel wall [22], there is a possibility that oxygen still remained in the gas flow channel. Figure 2-11 shows the images obtained at 0 (U_{O2} = 0%) (a), 0.018 (U_{O2} = 30.5%) (b), 0.036 (U_{O2} = 60.9%) (c), and 0.054 A cm^{-2} (U_{O2} = 91.4%) (d), respectively, at $\Phi(O_2)$ = 3%. The pressure loss was ca. 0.3 kPa of $p(O_2)$, or ca. 10 kPa of air, as well as at $\Phi(O_2)$ =10 and 5%. Figure 2-11(d) (0.054 A cm^{-2}, U_{O2} = 91.4%) is striking; the latter two thirds of the image are in black, or $p(O_2)$ = 0 kPa, on the GDL surface. The cell was not able to be operated at U_{O2} = 96.5%.

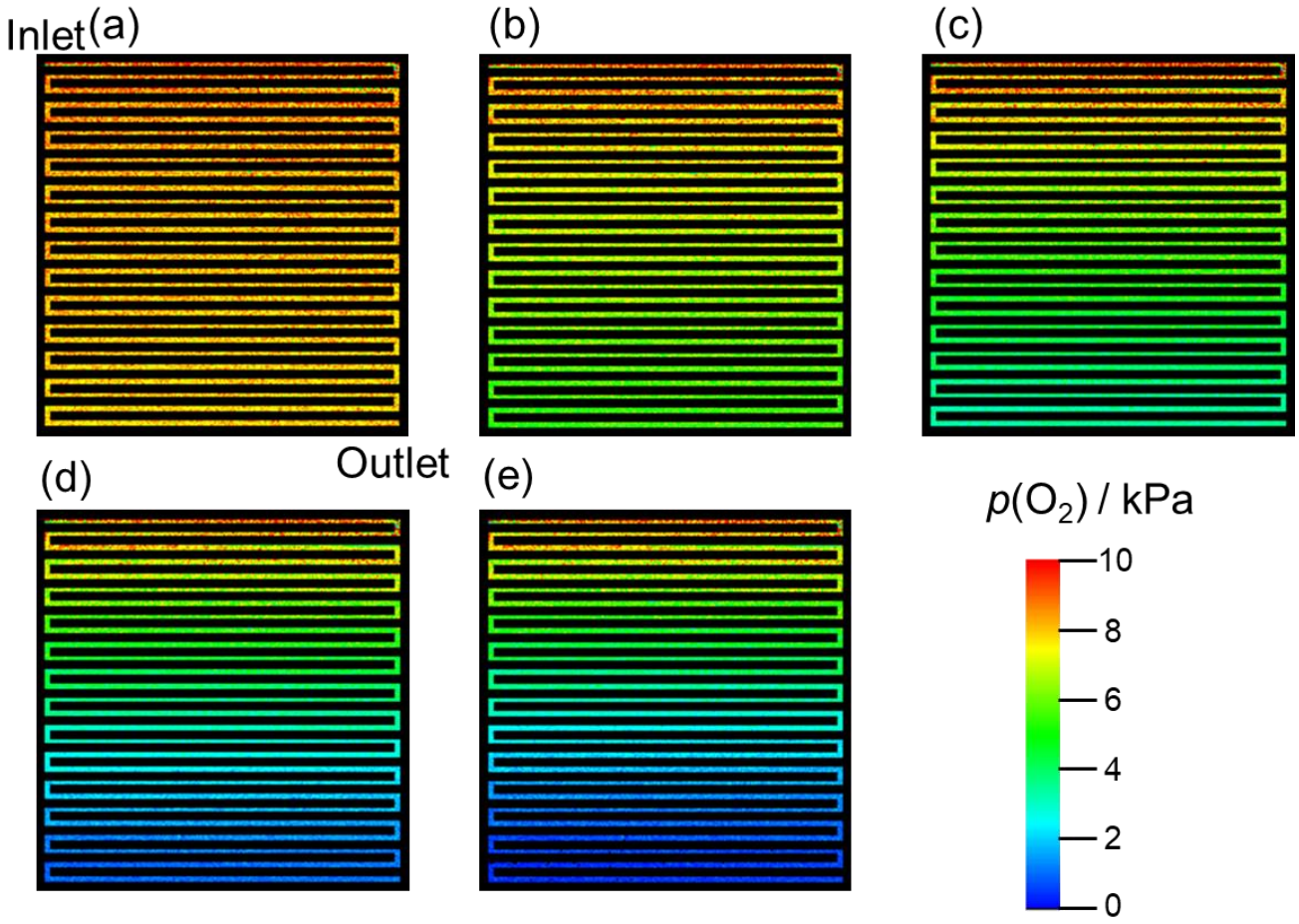

Fig. 2-9 Images of $p(O_2)$ on the GDL surface at the cathode at $\Phi(O_2)$ = 10% during cell operation (T = 80 °C, air flow rate = 200 mL min^{-1}, hydrogen flow rate = 100 mL min^{-1}, ambient pressure) at 0 (U_{O2} = 0%) (a), 0.06 (U_{O2} = 30.5%) (b), 0.12 (U_{O2} = 60.9%) (c), 0.18 (U_{O2} = 91.4%) (d), and 0.19 A cm^{-2} (U_{O2} = 96.5%) (e). Associated color bar indicates $p(O_2)$.

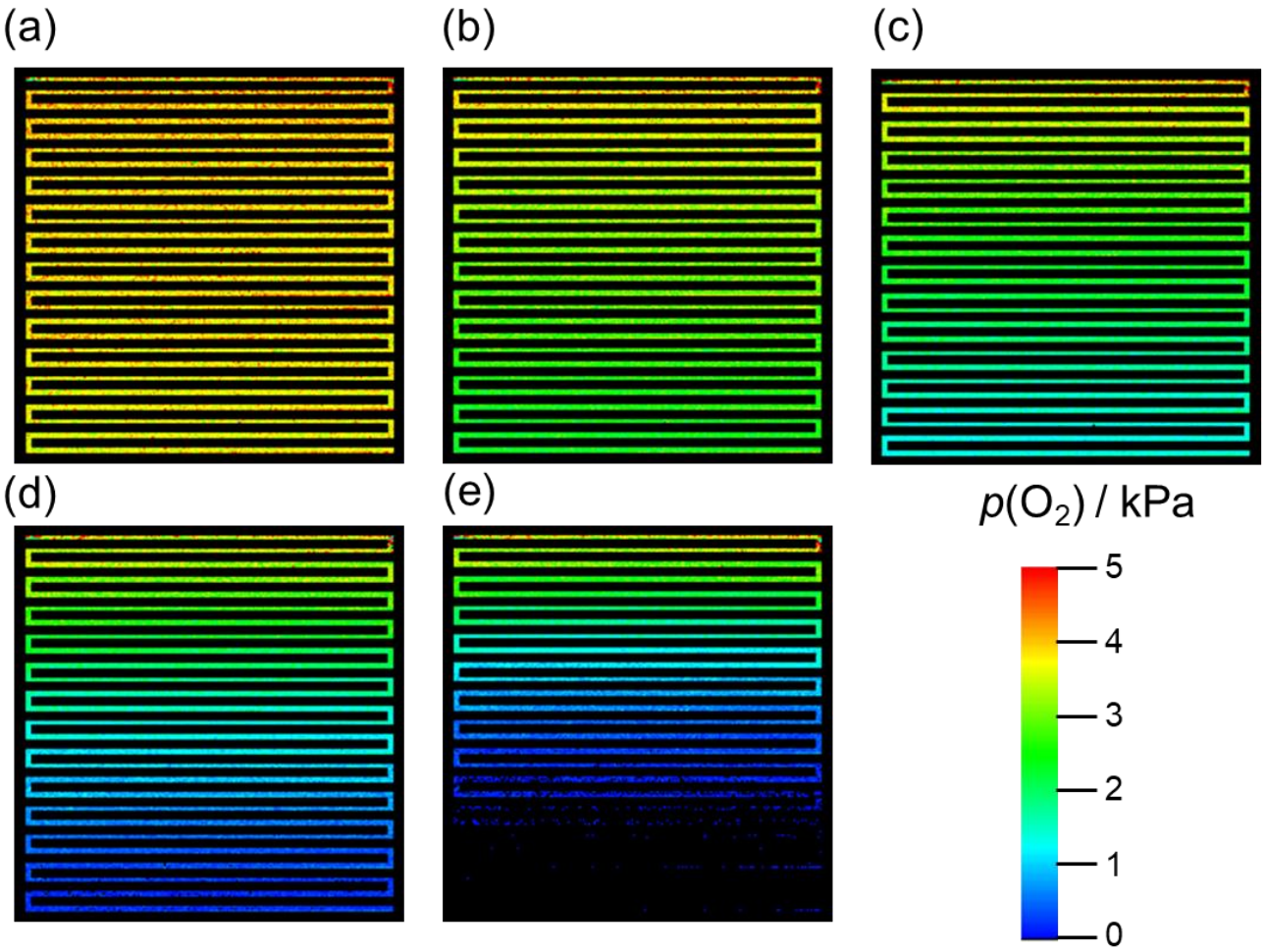

Fig. 2-10 Images of $p(O_2)$ on the GDL surface at the cathode at $\Phi(O_2)$ = 5% during cell operation (T = 80 ºC, air flow rate = 200 mL min^{-1}, hydrogen flow rate = 100 mL min^{-1}, ambient pressure) at 0 (U_{O2} = 0%) (a), 0.03 (U_{O2} = 30.5%) (b), 0.06 (U_{O2} = 60.9%) (c), 0.09 (U_{O2} = 91.4%) (d), and 0.095 A cm^{-2} (U_{O2} = 96.5%) (e). Associated color bar indicates $p(O_2)$.

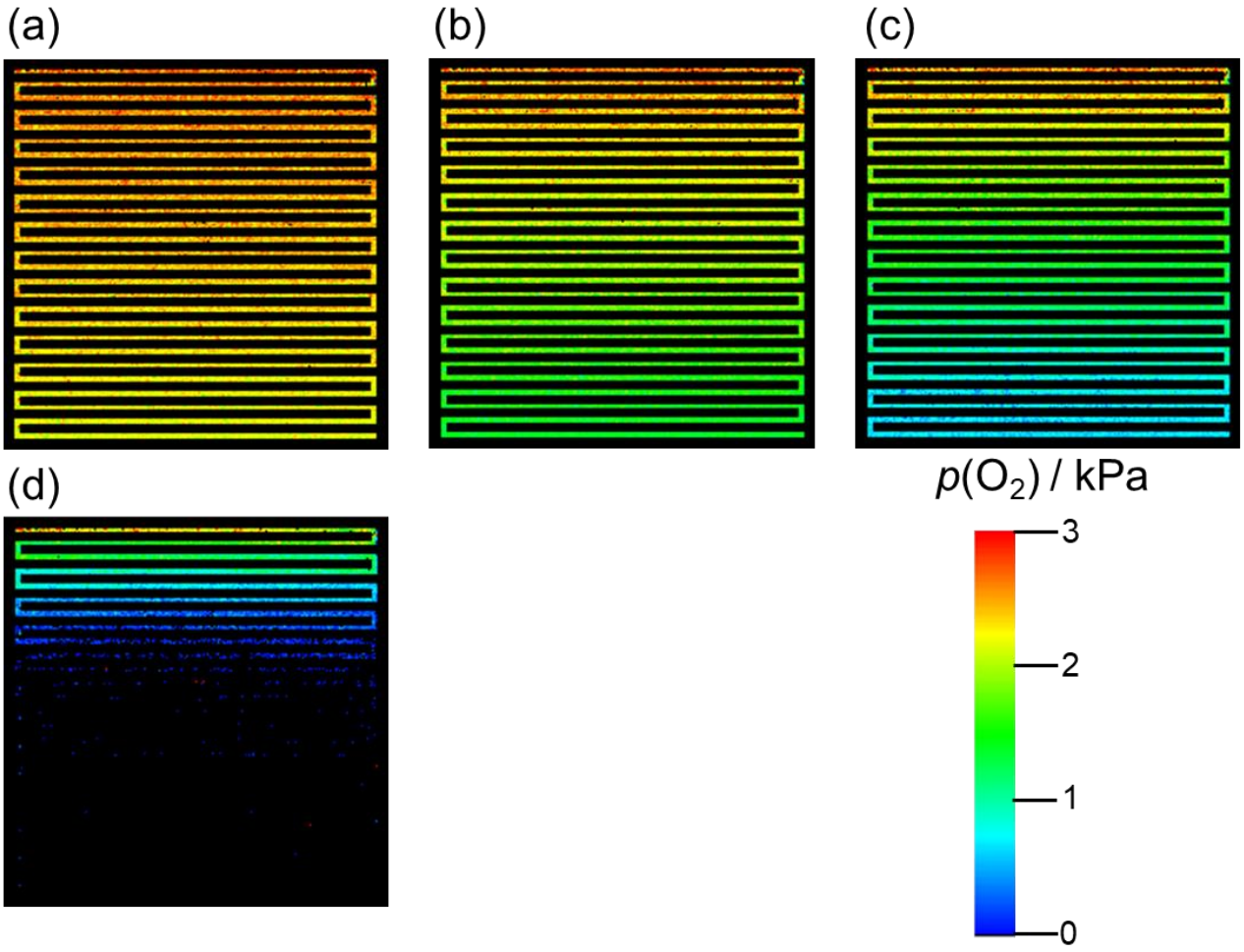

Fig. 2-11 Images of $p(O_2)$ on the GDL surface at the cathode at $\Phi(O_2)$ = 3% during cell operation (T = 80 °C, air flow rate = 200 mL min^{-1}, hydrogen flow rate = 100 mL min^{-1}, ambient pressure) at 0 (U_{O2} = 0%) (a), 0.018 (U_{O2} = 30.5%) (b), 0.036 (U_{O2} = 60.9%) (c), 0.054 A cm^{-2} (U_{O2} = 91.4%) (d). Associated color bar indicates $p(O_2)$.

Figure 2-12 shows the continuous line plots of $p(O_2)$ on the GDL surface in the middle of the flow channel with a width of a pixel (ca. 120 mm) along the flow channel length from the inlet to the outlet at $\Phi(O_2) = 10$ (a), 5 (b), and 3% (c) at different current densities. The black line represents $U_{O2} = 0\%$, the red line 30.5%, the orange line 60.9%, the green line 91.4% and the blue line 96.5%. $p(O_2)$ values showed 1 to 2 kPa scattering due to the geometrical effects of the flow channel and the GDL [18, 24]. It is noticeable that the trends of these line plots of $p(O_2)$ under $U_{O2} = 0$, 30.5, and 60.9% represented by black, red and orange lines, respectively, are similar at different $\Phi(O_2)$ values. However, these trends started to differ at $U_{O2} \geq 91.4\%$. The decrease of $p(O_2)$ along the gas flow channel became more pronounced from $\Phi(O_2) = 10\%$ to $\Phi(O_2) = 3\%$.

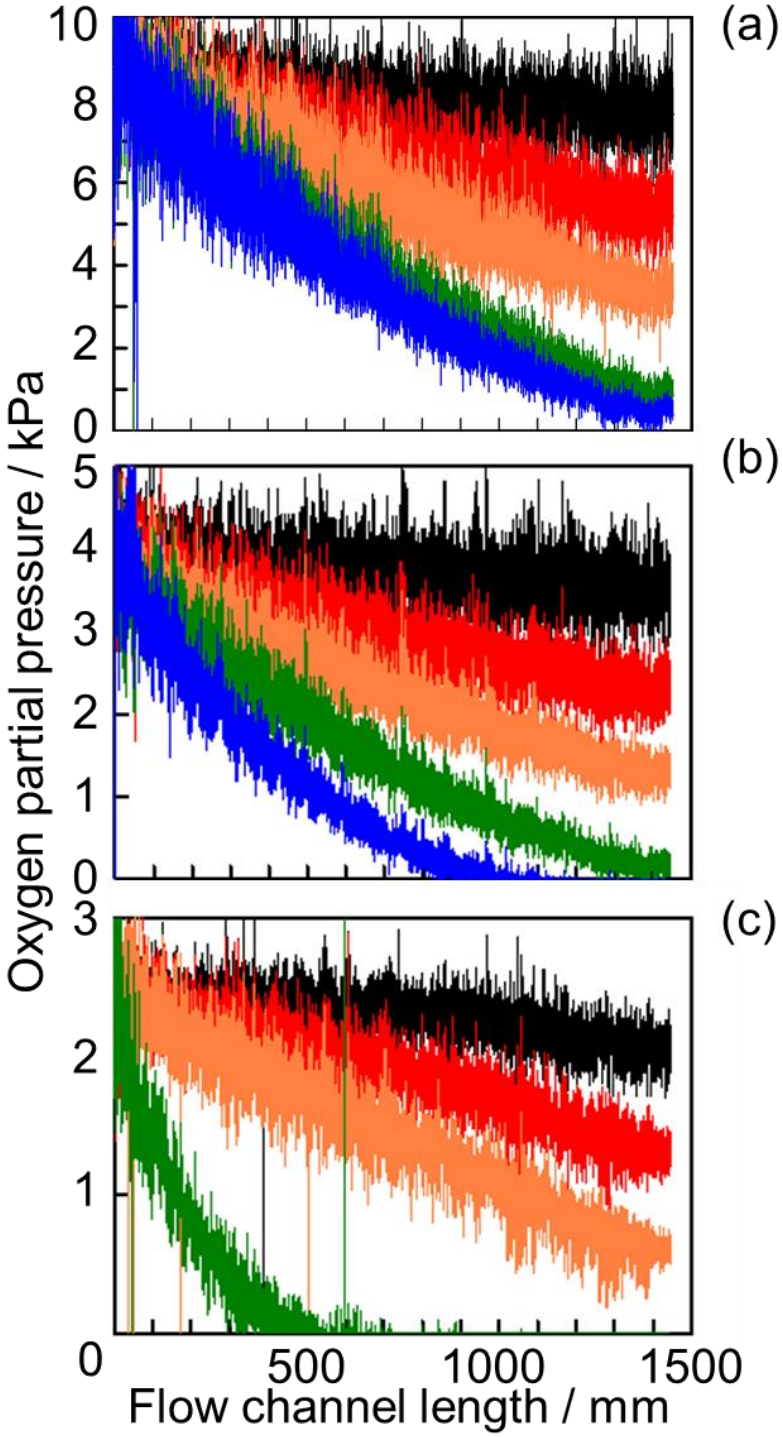

Fig. 2-12 $p(O_2)$ plotted along the flow channel length. The black lines represent U_{O2} = 0%, the red lines U_{O2} = 30.5%, the orange lines U_{O2} = 60.9%, the green lines U_{O2} = 91.4% and the blue lines U_{O2} = 96.5%.$\Phi(O_2)$ = 10 (a), 5 (b), and 3% (c).

Figure 2-13 shows the trendlines of the line plots derived from Fig. 2-10. These trendlines were normalized by the averaged values of the first 100 data points of each step along the flow channel length. The large decrease of $p(O_2)$ is clearly seen at the early stage along the flow channel length at lower $\Phi(O_2)$.

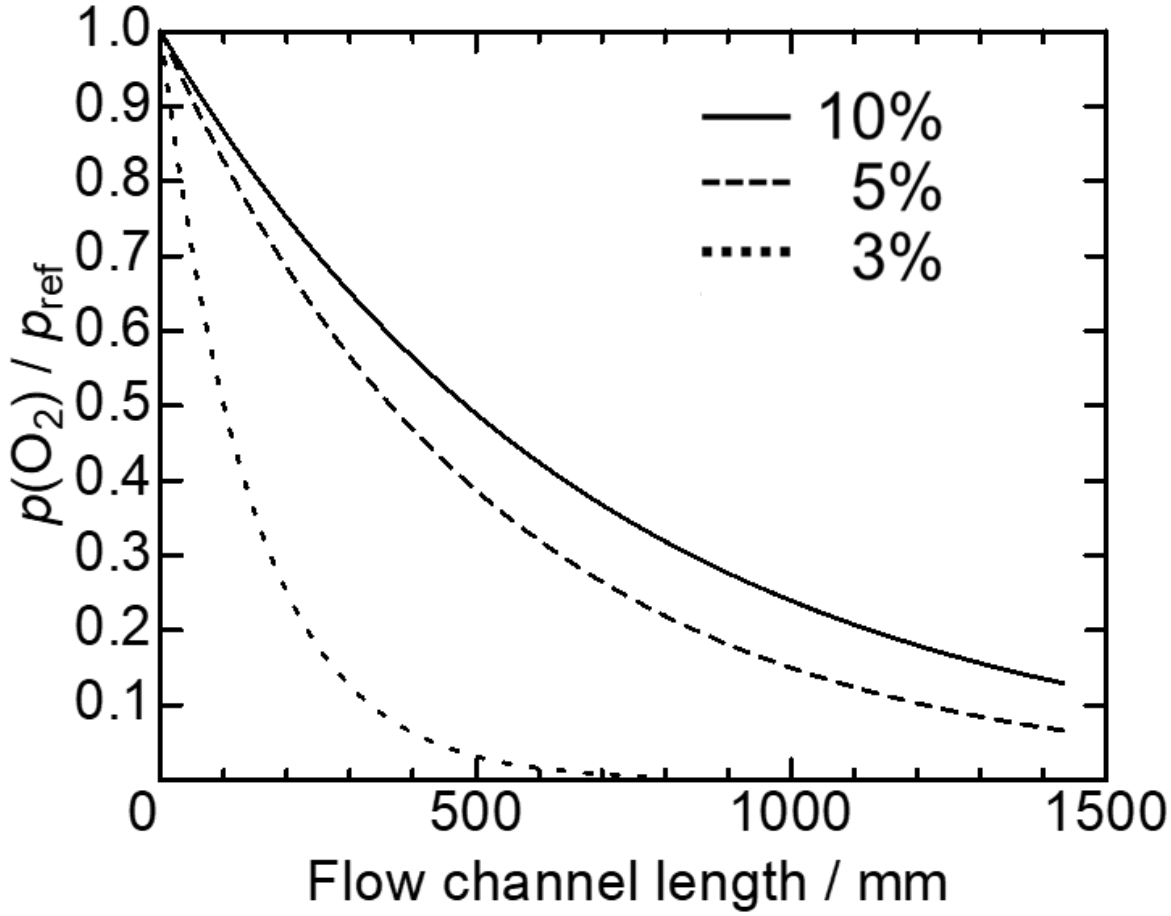

Fig. 2-13 Normalized trendlines of line plots derived from Fig. 2-9 at $\Phi(O_2)$ = 10, 5, and 3%. U_{O2} = 91.4%.

Figure 2-14 schematically illustrates the oxygen and hydrogen partial pressures along the flow channel lengths. At low $\Phi(O_2)$ ($\leq$ 5%), oxygen became to be consumed at the earlier stage along the flow channel length, and at high U_{O2} ($\geq$ 91.4%), $p(O_2)$ near the outlet became 0 kPa on the GDL surface (Figs. 2-9 and 2-10). To understand $p(O_2)$ = 0 kPa on the GDL surface near the outlet, the linear sweep voltammetry (LSV) was conducted (Fig. 2-15) for determining the effect of the cross leakage of hydrogen from the anode through the membrane to the cathode. The temperature and humidity were the same as those during cell operation. For the LSV, nitrogen was supplied to the cathode, and hydrogen to the anode. The flow rates of both gases were set at 200 mL min^{-1}. The amount of the hydrogen cross leak was measured as 0.028 mL min^{-1} cm^2, similar to the value previously reported (< 0.02 mL min^{-1} cm^2) [25]. The oxygen consumption caused by this hydrogen cross leakage would be only 0.07-0.7% of that existed in the diluted air, therefore, the influence of the hydrogen cross leakage on the oxygen consumption at the cathode was expected to be very small. In addition, the amount of oxygen cross leakage is significantly lower, 1/10 to 1/100 of that of hydrogen. The gas cross leakage could not explain $p(O_2)$ = 0 kPa on the GDL surface.

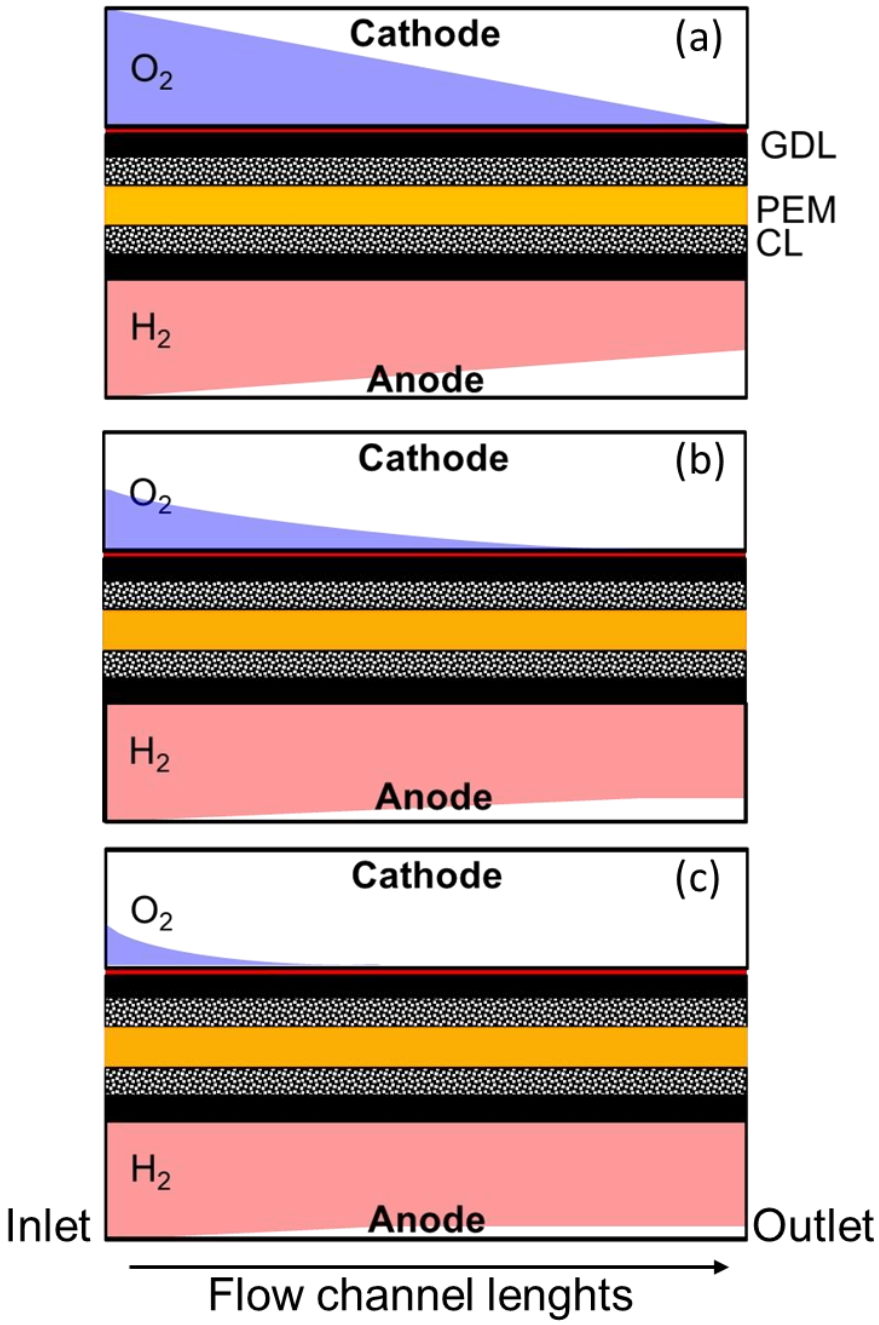

Fig. 2-14 Schematic illustrations of the concentrations of oxygen at the cathode and hydrogen at the anode along the channel lengths. $\Phi(O_2)$ = 10 (a), 5 (b), and 3% (c).

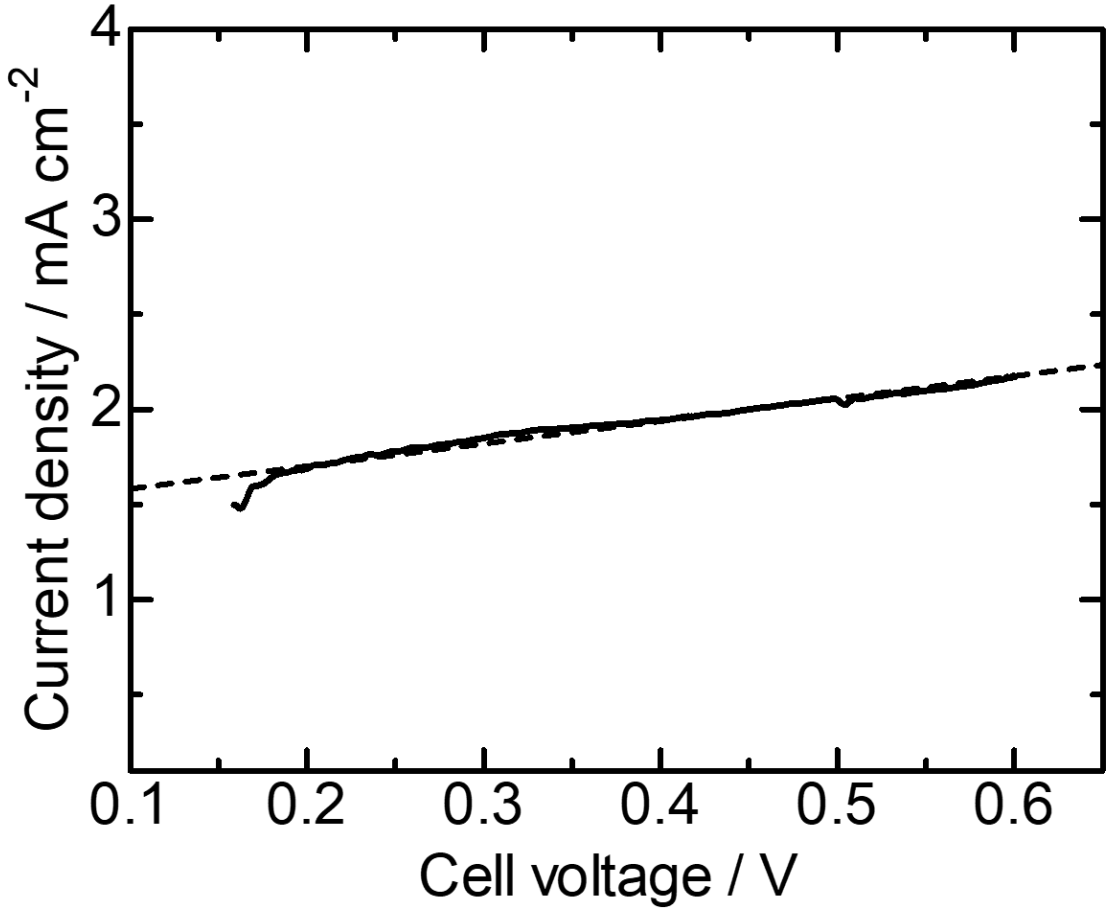

Fig. 2-15 Linar sweep voltanmetory. The cell temperature was 80 ºC, and the RHs at the cathode and anode were 42 and 88%, respectively.

Since the area for the power generation shifted near to the inlet, the electrochemical potential at the MEA near the outlet might be lowered. In an MEA using a gas diffusion electrode, hydrogen evolution and the oxidation current of the generated hydrogen gas are often observed at potentials lower than ca. 0.1 V (vs. hydrogen electrode) [9]. Therefore, a possibility is that the potential decreased to 0.1 V or less at the MEA near the outlet, and the hydrogen evolution occurred at the cathode, which chemically/electrochemically consumed oxygen near the outlet [9]. Previously, the zero current regions were not observed during oxygen starvation in a segmented cell [9]. Considering the hydrogen evolution at the cathode, it is reasonably understood that the regions exist where the current density is not 0 A cm^{-2} [26] but $p(O_2)$ = 0 kPa (this study).

Based on the previous results discussing the differences of $p(O_2)$ on the GDL and in the gas flow channel [27], a possibility of the coexistence of oxygen and hydrogen in the flow channel at the cathode is not negligible, which might cause not only a performance drop but also an operational instability and a danger for the cell damage presumably triggered by the unexpected chemical reaction, or local combustion, directly with hydrogen and oxygen. Actually, in a fuel cell stack, Mousa et al. detected a hydrogen concentration of 6.3% at the cathode outlet at $\Phi(O_2)$ = 5% and that of 9.4% at $\Phi(O_2)$ = 3% [13]. They explained the existence of those large amounts of hydrogen at the cathode outlet by proposing a mechanism of hydrogen pumping through the membrane to the cathode [13]. In our case in a single cell, the hydrogen pumping could not occur because of no energy supply for the pumping.

The visualized images of $p(O_2)$ inside a single cell (Figs. 2-9 ~ 2-11) in this study might be depicting the situation that could occur prior to the hydrogen pumping inside fuel cell stacks during oxygen starvation. The consumption of oxygen at the cathode significantly

reduced the performance of a single cell (Fig. 2-13). In the areas of an MEA not exposed to oxygen, the CL is expected to be susceptible to degradation. For example, Yamashita et al. reported the effect of oxygen starvation on the degradation of Pt catalysts supported on carbon at the cathode upon hydrogen start-up [28]. The oxidation reaction of carbon by water proceeded by local electrochemical cells arising due to a limited access of hydrogen needed for the reduction of Pt oxides. Within a fuel cell stack, the area in which oxygen starvation occurs in a single cell might prohibit the current flow at the identical areas of the other cells. Therefore, there is a possibility that the oxygen starvation in a single cell could drastically lower the performance of the entire stack. The oxygen starvation could be a larger problem in stacks operated at high current densities.

2.4 Conclusion

The $p(O_2)$ distribution at low $\Phi(O_2)$ on the GDL surface at the cathode inside a PEMFC was visualized by a nondestructive real-time/space monitoring system. It was shown that $p(O_2)$ decreased along the flow channel length. The decrease of $p(O_2)$ along the flow channel length at U_{O2} of 0, 30.5, and 60.9% were similar at $\Phi(O_2)$ = 10, 5 and 3% but started to differ at U_{O2} ≥91.4%. The low $\Phi(O_2)$ and high U_{O2} lead to a significant decrease of $p(O_2)$ near the outlet. At very low $\Phi(O_2)$ and very high U_{O2}, there was no oxygen present on the GDL surface near the gas outlet possibly because of a generation of hydrogen at the cathode due to the local low voltage. Accordingly, at lower $\Phi(O_2)$ and high U_{O2}, the starvation of oxygen lowered the cell performance of a single cell. Experimentally, the hydrogen evolution at the cathode prior to the hydrogen pumping from the anode was evidenced by showing areas on the GDL where $p(O_2)$ = 0 kPa. The effects should be more pronouncedly on the performance, stability, and durability, as well as safety, of fuel cell stacks.

References

[1] R. Borup, J. Meyers, B. Pivovar, Y. S. Kim, R. Mukundan, N. Garland, D. Myers, M. Wilson, F. Garzon, D. Wood, P. Zelenay, K. More, K. Stroh, T. Zawodzinski, J. Boncella, J. E. McGrath, M. Inaba, K. Miyatake, M. Hori, K. Ota, Z. Ogumi, S. Miyata, A. Nishikata, Z. Siroma, Y. Uchimoto, K. Yasuda, K. I. Kimijima, N. Iwashita, Chem. Rev. 107 (2007) 3904–3951.

[2] J. C. Kurnia, A.P. Sasmito, T. Shamim, Appl. Energy 252 (2019) 113416.

[3] Z. Y. Liu, B. K. Brady, R. N. Carter, B. Litteer, M. Budinski, J. K. Hyun, D. A. Muller, J. Electrochem. Soc. 155 (2008) B979–B984.

[4] N. Yousfi-Steiner, P. Moçotéguy, D. Candusso, D. Hissel, J. Power Sources 194 (2009) 130–145.

[5] S. B. Beale, U. Reimer, D. Froning, H. Jasak, M. Andersson, J. G. Pharoah, W. Lehnert, J. Electrochem. Energy Convers. Storage 15 (2018) 1–7.

[6] A. Manokaran, S. Pushpavanam, P. Sridhar, J. Appl. Electrochem. (2015) 353–363.

[7] K. Mitsuda, H. Nishiguchi, Electrochemistry 78 (2010) 757–763.

[8] M. Gerard, J. P. Poirot-Crouvezier, D. Hissel, A. M. Marie-Cecile Pera, B. Bador, J Fuel Cell Sci Technol 7 (2010) 361–369.

[9] Z. Liu, L. Yang, Z. Mao, W. Zhuge, Y. Zhang, L. Wang, J. Power Sources 157 (2006) 166–176.

[10] K. Takanohashi, T. Suga, M. Uchida, T. Ueda, Y. Nagumo, J. Inukai, H. Nishide, M. Watanabe, J. Power Sources 343 (2017) 135–141.

[11] K. Takada, Y. Ishigami, J. Inukai, Y. Nagumo, H. Takano, H. Nishide, M. Watanabe, J. Power Sources 196 (2011) 2635–2639.

[12] K. Nagase, T. Suga, Y. Nagumo, M. Uchida, J. Inukai, H. Nishide, M. Watanabe, J. Power Sources 273 (2015) 873–877.

[13] G. Mousa, J. DeVaal, F. Golnaraghi, Int. J. Hydrogen Energy 39 (2014) 21154–21164.

[14] H. Chena, X. Zhaoa, T. Zhanga, P. Peib, Energy Convers. Manag. 182 (2019) 282–298.

[15] K. Asai, Y. Amao, Y. Iijima, I, Okura, H. Nishide, J. Thermophys. Heat Transfer 16 (2002) 109–115.

[16] T. Masuda, E. Isobe, T. Higashimura, J. Am. Chem. Soc. 105 (1983) 7473–7474.

[17] J. Inukai, K. Miyatake, K. Takada, M. Watanabe, T. Hyakutake, H. Nishide, Y. Nagumo, M. Watanabe, M. Aoki, H. Tanano, Angew. Chem. Int. Ed. 47 (2008) 2792–2795.

[18] T. Hyakutake, H. Taguchi, J. Kato, H. Nishide, M. Watanabe, Macromol. Chem. Phys. 210 (2009) 1230–1234.

[19] T. Hyakutake, Y. Ishigami, J. Kato, J. Inukai, K. Miyatake, H. Nishide, M. Watanabe, Macromol. Che. Phys. 212 (2011) 42–47.

[20] J. Inukai, K. Miyatake, Y. Ishigami, M. Watanabe, T. Hyakutake, H. Nishide, Y. Nagumo, M. Watanabe, A. Tanaka, Chem. Commun. (2008) 1750–1752.

[21] Y. Ishigami, K. Takada, H. Yano, J. Inukai, M. Uchida, Y. Nagumo, T. Hyakutake, H. Nishide, M. Watanabe, J. Power Sources 196 (2011) 3003–3008.

[22] A. M. Niroumand, H. Homayouni, J. DeVaal, F. Golnaraghi, E. Kjeang, J. Power Sources 322 (2016) 147–154.

[23] K. Nagase, H. Motegi, M. Yoneda, Y. Nagumo, T. Suga, M. Uchida, J. Inukai, H. Nishide, M. Watanabe, ChemElectroChem. 2 (2015) 1495–1501.

[24] K. Takanohashi, M. Uchida, A. Iiyama, J. Inukai, J. Surf. Fin. Soc. Jpn. 68 (2017) 338–343.

[25] "DupontTM Nafion® NR211 and NR212 Ion Exchange Materials", https://www.fuelcellstore.com/spec-sheets/chemours-nafion-211-212-spec-sheet.pdf (October 20, 2020).

[26] R. N. Carter, S. S. Kocha, F. Wagner, M. Fay, H. A. Gasteiger, ECS Trans. 11 (2007) 403–410.

[27] Y. Ishigami, W. Waskitoaji, M. Yoneda, K. Takada, T. Hyakutake, T. Suga, M. Uchida, Y. Nagumo, J. Inukai, H. Nishide, M. Watanabe, J. Power Sources 269 (2014) 556–564.

[28] Y. Yamashita, S. Itami, J. Takano, K. Kakinuma, H. Uchida, M. Watanabe, A. Iiyama, M. Uchida, J. Electrochem. Soc. 164 (2017) F181–F187.

Chapter 3

Oscillation mechanism based on *operando p*(O_2) measurement using optical probes

3.1 Introduction

Under certain conditions, the cell voltage and the current density become unstable and even fluctuated because of the instability of the reactions inside PEMFCs. Since the excess liquid water in a cell is one of the main sources of instability, the water management during power generation has been extensively studied [1, 2]. The water generated by the power generation is continuously removed outside the fuel cell through the GDLs. However, when the water generation is too large, the flooding is inevitable. Therefore, a proper water management is of paramount importance for PEMFCs. Materials must be developed, and the operating conditions and the cell configurations must be optimized. Barbir et al. investigated unexpected increases in pressure and cell resistance of a PEMFC stack during power generation [3]. They pointed out that the increase in pressure could be indicative of the increased liquid water in the stack, while the increase in cell resistance is of a membrane dry-out. Hirakata et al. investigated the effect of pore size of GDL on the periodic instability of the cell voltage accompanied by the synchronized change in gas pressure, which were conclude to be caused by the water droplets blocking/releasing the cathode flow channel [4].

Recently, the oscillation phenomena during the power generation have been reported in running PEMFCs. Sanchez and coworkers reported an oscillatory fluctuation when the cathode was dry and the anode was wet at a nominal humidity of 152% with the cell temperature of 70 ^{o}C [5]. The current density first decreased slowly from 650 to 610 mA cm^{-2} within 1000 s at a constant cell voltage of 500 mV. Subsequently, a fluctuation in

current density started, followed by a continuous oscillation between 600 and 60 mA cm^{-2} accompanied by a gradual decrease in average current density resulting in the decrease in cell performance. During the oscillation, the transition from the lowest current to the highest current took place in 20 s, and the transition from the highest to the lowest slightly longer than 20 s. The change of the coefficient of the electro-osmotic drag accompanied by that of the liquid-vapor permeation at the interface of the membrane was suggested as a major feedback mechanism for the oscillatory behavior [5,6]. The change in the properties at the membrane interface was visualized by current-sensing atomic force microscopy showing the oscillatory behaviors after the activation of the membrane [5]. The fluctuations were related to the water shortage at the anode, too. A combination of the limited water available at the anode, the electroosmotic drag transporting water from the anode to the cathode, and the insufficient water back diffusion from the cathode to the anode was proposed to cause the anode to dehydrate. The cell ohmic resistance decreased and the performance recovered by the anode re-humidification [7] Atkins et al. found periodic oscillations in current and cell resistance at a fixed cell potential of 500 mV [8]. From the initial conditions using sparger bottles for the feed-stream humidification (cell temperature = 100 ºC, sparger temperatures at the anode/cathode = 115 ºC /110 ºC), the temperatures of the sparger bottles were lowered to 80 ºC. Large fluctuations and a significant decrease of the current density, approximately 0.5 A cm^{-2}, were observed. The oscillation period of current was several hundreds of seconds and become larger when the sparger temperature was kept at 80 ºC. The ohmic resistance also oscillated between 50 and 250 mΩ.

I found a new oscillation phenomenon during the power generation at 0.6 A cm^{-2} using a GDL without an MPL at 60 ºC and 60% RH. The differential pressure between the

cathode inlet and outlet was 0 kPa during the oscillation. This phenomenon is very different from the cell voltage fluctuation previously reported to be synchronized with the differential pressure caused by the plugging of flow channels [4]. A different mechanism should have caused this new oscillation phenomenon without the excess liquid water in the gas flow channel. The amplitude and period of this newly-found oscillation were approximately 20 mV and 2 s, respectively, whereas the oscillation or fluctuation of the cell voltage previously reported at the dried cathode showed a period significantly longer than ours, about tens of seconds to hours [5–8]. The oscillation amplitudes of the current-density at constant voltages in previous studies were large, too: 0.05 - 0.55 [5,6], 0.5 - 1.1 [7], and 0.55 - 0.83 A cm^{-2} [8].

In order to elucidate the mechanism of this new oscillation phenomenon, $p(O_2)$ inside the GDLs during the power generation [9–17] was focused on, because $p(O_2)$ is directly related to the fuel cell overvoltage according to Nernst equation as described in Chapter 2.

William et al. developed an *operando* measurement system to obtain the oxygen concentration [18] using a commercially-available micro oxygen-concentration sensor 25 μm in diameter inserted into the GDL at the cathode of an operating PEMFC. The oxygen concentration was measured at different current densities and RHs. By using an X-ray computed tomography (CT) system, the GDL structure was also analyzed to be related to the oxygen transport resistance. In their system, as an current interrupt method for measuring the ohmic resistance and the current of PEMFC was interrupted [19]. When the current was interrupted, the oxygen concentration returned to the channel level in milliseconds, while the changes in the behavior of the sensor due to RH and temperature occurred over seconds [18]. Therefore, for a monitor of $p(O_2)$, at least 5 s was needed. In

addition, the measurements at multiple locations was not easy due to the size and strength of the oxygen sensor made with glass capillaries [18]. The group of the University of Yamanashi has developed a 2-dimensinal visualization system of $p(O_2)$ on the GDL surface and the flow-channel walls inside running PEMFCs using an oxygen-sensitive dye film [9–17]. To monitor $p(O_2)$ inside a GDL, a new apparatus using 5 optical fibers with diameter of 50 μm was developed. The probes can be precisely located with a spatial resolution of 1 μm in depth, and $p(O_2)$ can be simultaneously measured at 5 points both under the flow channel and under the ribs. The time resolution was 100 ms. With using this *operando* monitoring system, the voltage oscillation was found to be synchronized with $p(O_2)$ oscillation at all the locations inside the GDL.

3.2 Instrument

3.2.1 Oxygen-sensitive dye film

As described in Chapter 2, PtTFPP mixed with polyTMSP and toluene was used as an oxygen-sensitive dye to spray onto the GDL surface at the cathode flow channel. The PtTFPP concentration of the dye solution was adjusted to 25 wt%. PtTFPP has absorption peaks at 400 (blue light) and 530 nm (green light), and an emission peak of at 650 nm (red light). In this study, green light was used for the detection of $p(O_2)$ because of the excitation of Si of an optical fiber by blue light.

3.2.2 Optical fiber

Single-mode optical fibers with a clad diameter of 125 μm and a core diameter of 10 μm were immersed in HF solution (pH = 2.9) and etched until the diameter of approximately 50 μm was obtained. Subsequently, the top of the optical fiber was trimmed flat

perpendicular to the fiber axis. On the apex of a fiber, an oxygen-sensitive dye film was coated with a thickness of 2 μm.

The emission intensity as a function of the temperature was negligibly small, with the change in the emission of −0.5% K^{-1} [9]. The influence of the humidity on the oxygen partial pressure in air was negligibly small, too [9]. When the dye film at the apex of a probe was wet with liquid droplets, the emission intensity much increased [10,14]. Under the conditions for the power generation in this study, the apex of the probe was never wet, and the intensity of the emission was steadily monitored.

3.2.3 Oxygen monitoring system

Figure 3-1(a) shows a schematic representation of the $p(O_2)$ monitoring system. In the cathode side of a GDL, 5 holes were created down to the CL both under the flow channels and the ribs. The optical probes were inserted directly into a PEMFC through the holes. The probe position was controlled by a micrometer. The effect of inserting the probe into the manufactured hole to mass fraction of oxygen was simulated. Figures 3-2(a) ~ (c) show an X-ray CT image of a GDL, a 3-dimensional numerical simulation of mass fraction of oxygen inside the GDL, and a cross-sectional numerical simulation of mass fraction of oxygen inside the GDL without a hole, respectively. Figures 3-2(d) ~ (f) show an X-ray CT image of a GDL with a hole (90 μm in diameter) and an optical probe (50 μm in diameter) inserted, a 3-dimensional numerical simulation of the mass fraction of oxygen inside the GDL, and a cross-sectional numerical simulation of the mass fraction of oxygen inside the GDL with a hole and an optical probe, respectively. The oxygen concentrations at the surfaces of the GDL at the CL side were set at the values expected at the current density of 1.0 A cm^{-2}. The colors shown in the images represent the mass

fraction of oxygen and are defined with the associated color bar. The oxygen mass fraction was calculated inside the GDL based simply on the diffusion and the difference was less than 1% with/without a hole and a probe. Figures 3-3(a) and (b) are calculated oxygen mass fraction at the apex of the probe at different depths at 0.2 and 1.0 A cm^{-2}, respectively. With and without the virtual probes, the differences were approximately 1%.

For measuring the distance between the probe apex and the CL, a super luminescent diode light with a wavelength of 830 nm was introduced to the probe to obtain an interference light from the CL and the probe apex (Fig. 3-1(b)). The spectrum of reflection light out from the optical probe was Fourier-transformed to measure the distance with an error of 1 μm.

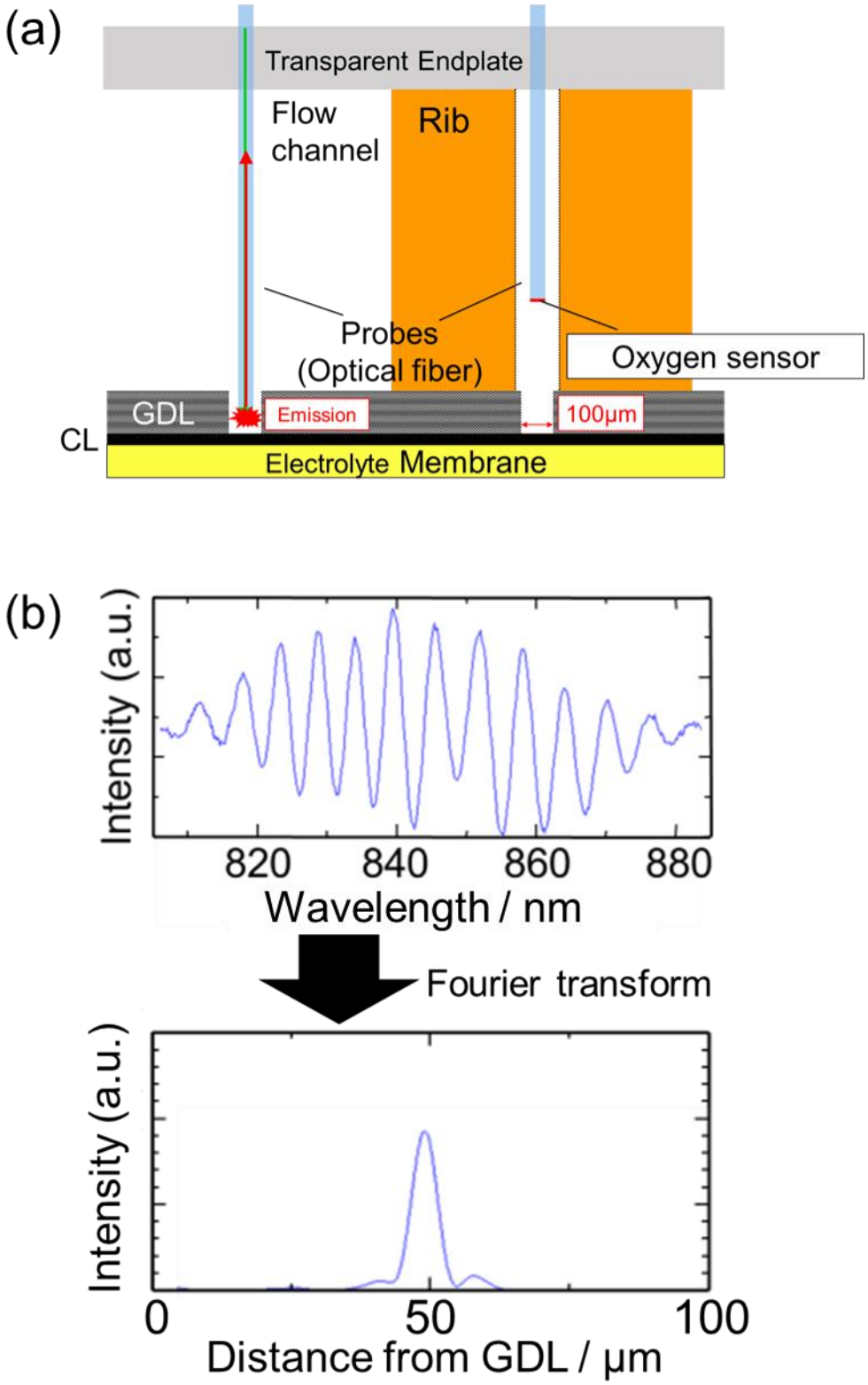

Fig. 3-1 (a): Schematic representation of $p(O_2)$ measurement inside GDL. (b): Interference between the lights from the probe tip and the surface of catalyst layer Fourier-transformed to determine distance from catalyst layer.

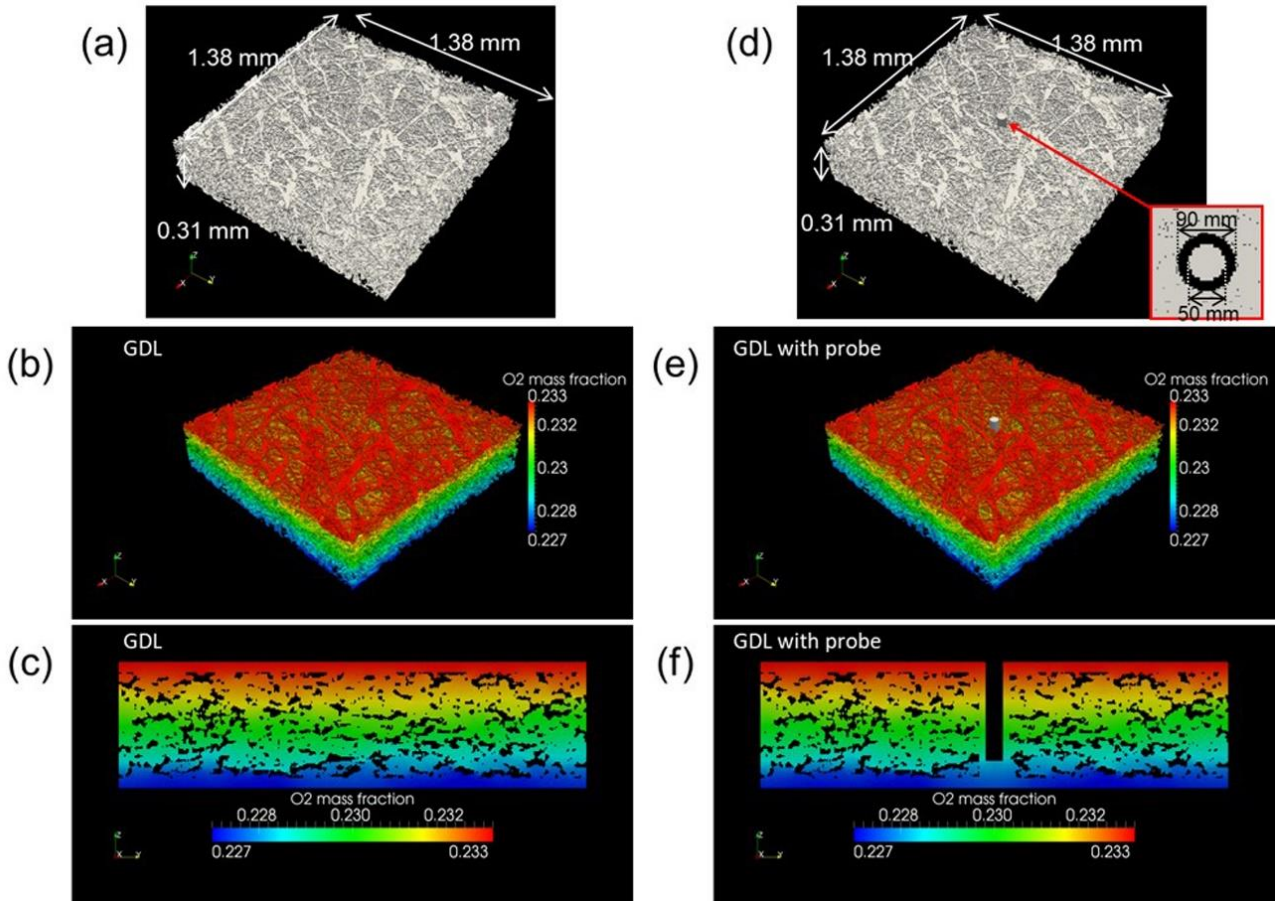

Figure 3-2 (a): X-ray CT image of GDL without a hole. (b): 3-dimensional numerical simulation of mass fraction of oxygen inside GDL without a hole. (c): Cross-sectional numerical simulation of mass fraction of oxygen inside GDL without a hole. (d): X-ray CT image of GDL with a hole (90 μm in diameter) and an optical probe (50 μm in diameter). (e): 3-dimensional numerical simulation of mass fraction of oxygen inside GDL with a hole and an optical probe. (f): Cross-sectional numerical simulation of mass fraction of oxygen inside GDL with a hole and an optical probe. The data are provided from Mizuho Information & Research Institute.

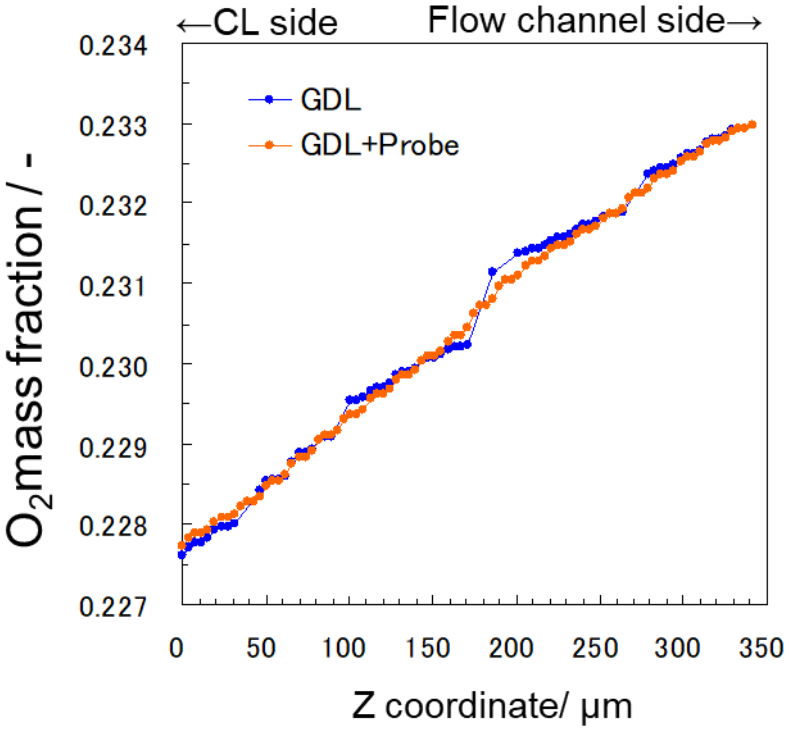

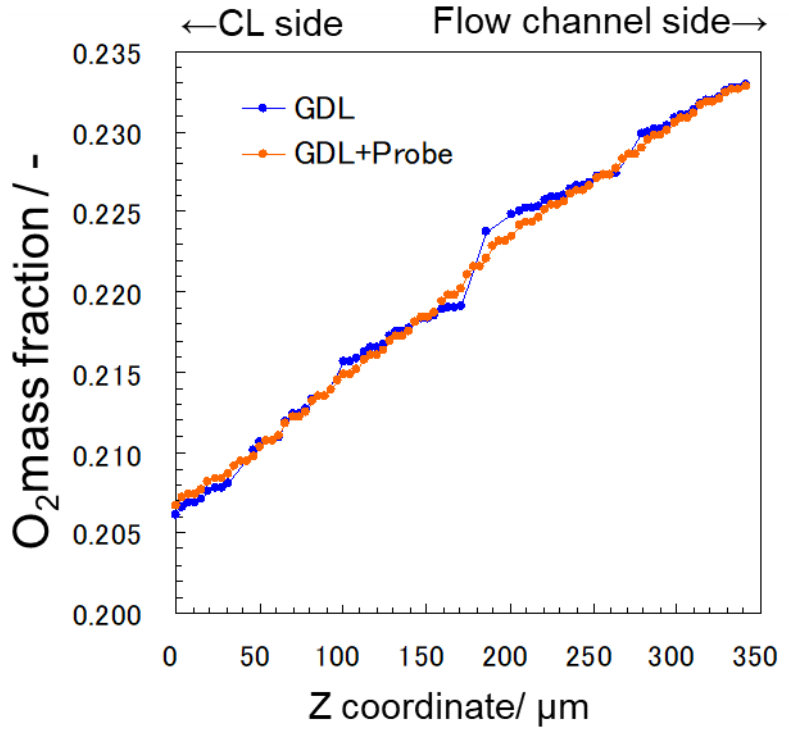

Figure 3-3 Calculated oxygen mass fraction at probe apex at different probe positions at 0.2 (a) and 1.0 A cm^{-2} (b). The data are provided from Mizuho Information & Research Institute.

3.2.4 Cell for the oxygen monitoring

Figure 3-4(a) shows the structure of a cell with 10 straight flow channels for $p(O_2)$ monitoring. At the cathode side of a stainless endplate, a window was created for the insertion of the optical probes. An acrylic insulator plate with 5 holes was inserted between the endplate and the current collector for the probe positioning. The cathode and the anode gases were supplied as parallel flows. The channel length was 30 mm. The ribs and the cathode and the anode were at the overlapping positions. The active catalyst area was 20 mm × 20 mm. Figure 3-4(b) shows the positions of the holes created through the GDLs under the central rib, located at 2.5, 10.0, and 17.5 mm from the edge of the GDL and 5.0 and 15.0 mm under the flow channels from the GDL edge.

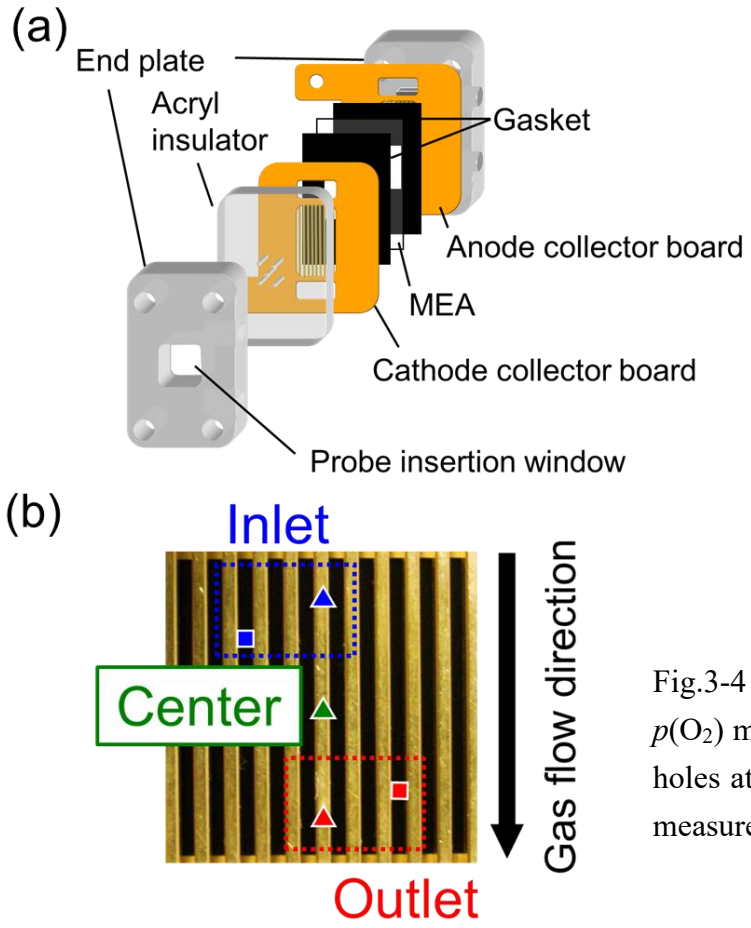

Fig.3-4 (a): Cell used for *operando* $p(O_2)$ measurement. (b): Positions of holes at GDL, or locations for $p(O_2)$ measurement.

3.2.5 Optical diagrams

As shown in Fig. 3-5(a), a 532 nm diode laser light was divided into 5 by beam splitters to 2 μW. Each light was irradiated onto the oxygen-sensitive dye film at the apex of the probes. The excitation light and the 650 nm emission were separated by a dichroic mirror, and the emission was detected by a CCD camera with a filter for the reflective excitation light placed in front of the camera. An optical diagram of the probe positioning is shown in Fig. 3-5(b). The probes were positioned as described in Section 3.2.3.

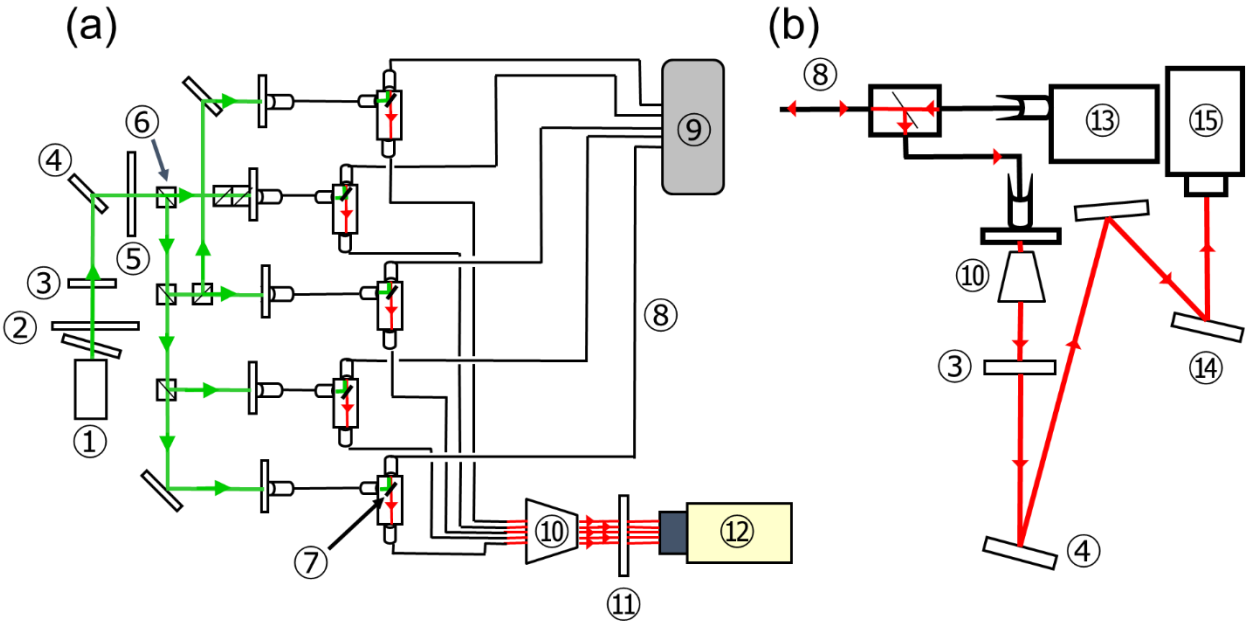

Figure 3-5 Schematic diagrams of $p(O_2)$ (a) and distance (b) measurement systems. Optical components are allotted as 1: Diode laser (532 nm), 2: Quarter-wave plate, 3: Extinction filter, 4: Mirror, 5: Shutter, 6: Beam splitter, 7: Dichroic mirror, 8: Optical fiber, 9: Fuel cell, 10: Objective lens, 11: Reflection exciting light filter, 12: CCD camera, 13: SLD (830 nm), 14: Diffraction grating, 15: CCD camera.

3.3 Experiment

3.3.1 Cell preparation

Figure 3-6 shows the X-ray CT images of the GDLs without (SIGRASET 28BA, SGL Carbon Group Co., Ltd., Germany) and with (28BC) an MPL used in this study. The measurement were carried out at the beamline BL46XU of Spring-8, Japan, where the X-ray energy was 12.39 keV with a specific resolution of 0.37 μm voxel^{-1}. The GDLs (20 mm × 20 mm) were processed to have holes (100 μm created with the laser ablation) for inserting the optical probes (Section 2.4). To prepare the CCMs, a catalyst paste mixed with commercial Pt/CB (46wt%-Pt, TEC10E50E, Tanaka Kikinzoku Kogyo K. K., Japan.), pure water, ethanol, and 5wt% Nafion ionomers (ion exchange capacity = 0.9 meq g^{-1}, D-521, DuPont, U.S.A.) with an ionomer/carbon volume ratio of 0.7 was spray-coated on both sides of a Nafion membrane (NRE212, E.I. Du Pont Nemours & Company, Inc.) by using a pulse-swirl-spray apparatus (Nordson), and then dried at 60 ºC for 12 hours in an electro oven. The CCM was hot-pressed at 140 ºC and 2.5 kN for 3 minutes to form a MEA with the geometric area of 4.0 cm^{-2} and the Pt loading of 0.5 mg cm^{-2} on both the anode and the cathode. The PEMFC was assembled by using CCMs and a GDL (28BA or 28BC) with holes. The tightening pressure was 2.5 kN.

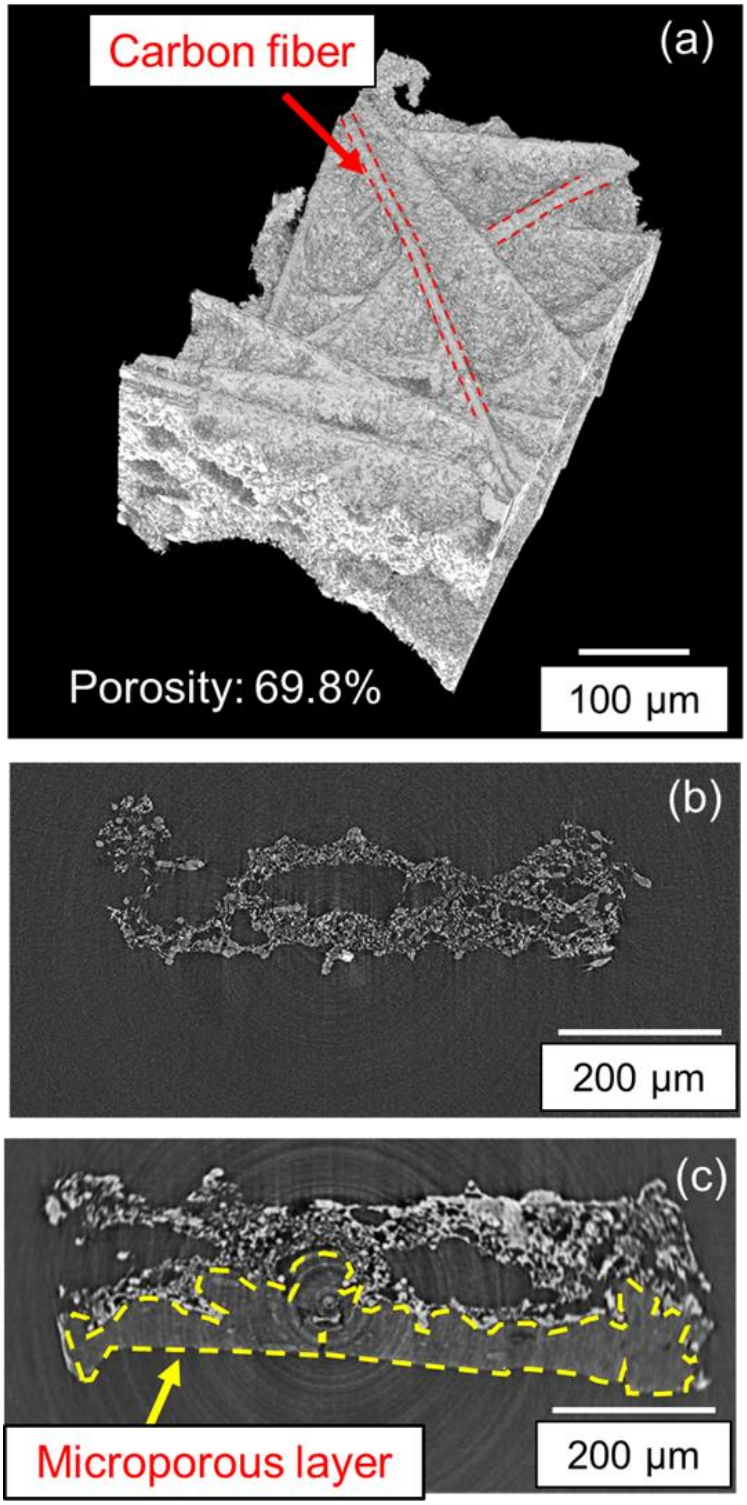

Fig. 3-6 X-ray CT image of 28BA (a), cross-sectional images of 28BA (b) and 28BC (c).

3.3.2 $p(O_2)$ measurement

For the power generation, a fuel cell evaluation system (As-510-340PE, NF Corp.) was used. The gases flew parallel and in the same direction at the cathode and the anode. Prior to $p(O_2)$ monitoring, the current density was held at 1 A cm^{-2} for 3 hours and 0.2 A cm^{-2} for 12 hours at the gas flow rates of hydrogen/oxygen = 400/200 mL min^{-1} at 40 °C and 100% RH for the cell conditioning. Then, the gases were switched to hydrogen/nitrogen = 100/100 mL min^{-1}, and the cell voltage was cycled 40 cycles at 20 mV s^{-1} between 0.075 and 1.0 V for measuring the electrochemical surface area. Subsequently, the cell temperature was changed to 60 ºC and 60% RH. The optical probes were inserted and positioned at a distance from the CL. For obtaining a calibration curve, mixed gasses with nitrogen and air at different concentrations were supplied to both the anode and the cathode first at 250 mL min^{-1} for 10 min. During the acquisition of the emission for 100 ms, the flow rate was reduced to 100 mL min^{-1} in order to minimize the pressure loss. At each gas-mixture rate, the emission was measured three times by a CCD camera at each probe to be averaged. The emission intensity of the oxygen sensitive dye was deteriorated by the laser irradiation linearly at approximately 0.03% s^{-1}. In order to obtain $p(O_2)$ using this dye film, the deterioration coefficient was taken into account after obtaining the emission data. A calibration curve is shown in Fig. 3-7 as an example.

For the power generation, the gas-flow rates were set at hydrogen/air = 400/200 mL min^{-1} and the current density at 0.2 A cm^{-2}. The current density was kept for 20 min and stepped to 0.6 A cm^{-2}. During power generation, the differential pressure was continuously monitored (DT-8890, CEM, Shenzhen Everbest Machinery Industry Co., Ltd.) between the inlet and outlet.

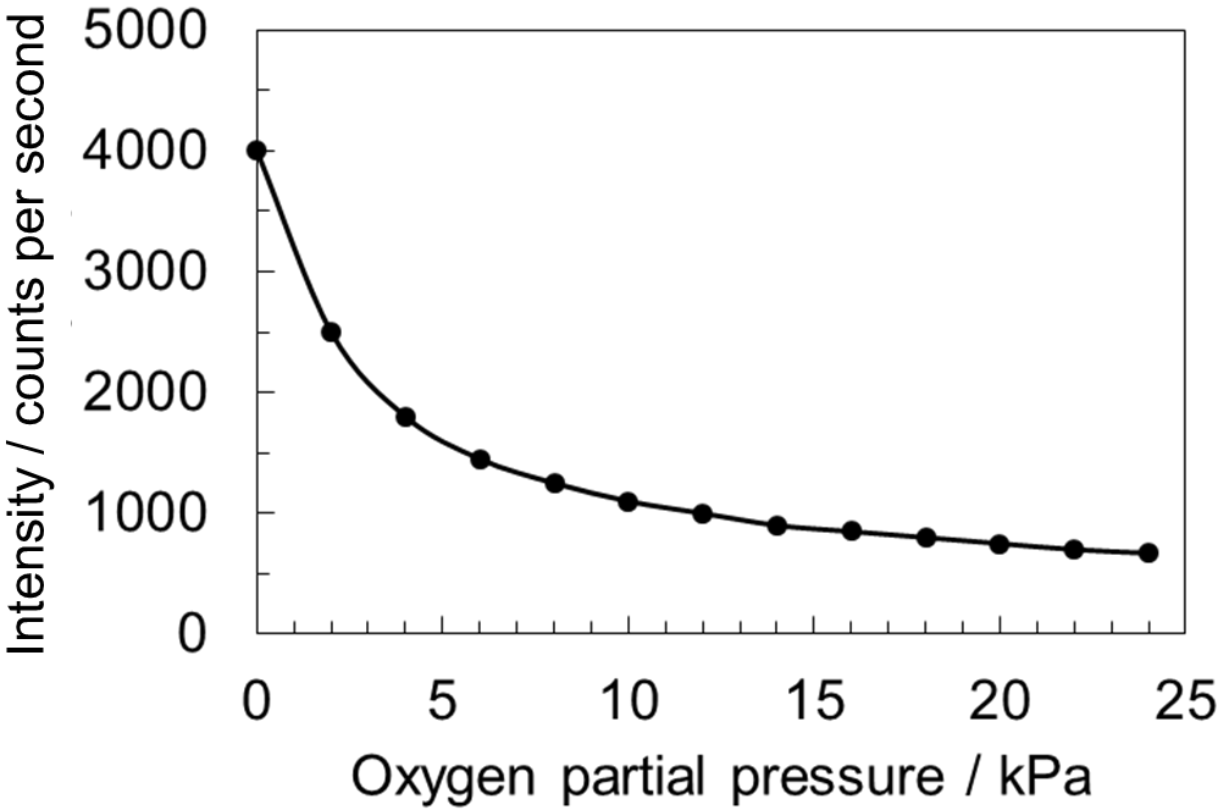

Fig. 3-7 Calibration curve for oxygen using sensitive dye (PtTFPP).

3.4 Results and discussion

3.4.1 Period and amplitude of voltage oscillation

With using a cell illustrated in Fig. 3-4 with/without probes, the power generation was carried out at 60 °C, 60% RH, 0.6 A cm^{-2}, and hydrogen/air = 400/200 mL min^{-1}. Figures 3-8(a) and (b) show the cell voltage and the differential partial pressure between the inlet and the outlet, respectively, at the cathode. Under these conditions, the voltage oscillation was clearly observed, whereas the differential pressure was lower than the detection limit (<0.01 kPa). In a previous report [4], a fluctuation of the cell voltage was accompanied by the differential pressure at the cathode by water plugging [10, 14], which cannot

explain this oscillation. The period of the cell voltage was approximately1.5 s and the amplitude (ΔV) 20 mV. Figures 3-9(a1) and (a2) show the period and amplitude, respectively, with respect to the air flow rate at 60 ºC, 60% RH, and 0.6 A cm^{-2}. Both the period and the amplitude decreased as the air flow rate increased. Figures 3-9(b1) and (b2) show the period and amplitude, respectively, with respect to the current density at 60 ºC, 60% RH, and the air flow rate of 200 mL min^{-1}. The period continuously decreased from 4.7 to 3.6 s at 0.6 A cm^{-2} as the current density increased from 0.3 to 0.6 A cm^{-2} (Fig. 3-9(b1)). The amplitude monotonously increased with the increase in current density (Fig. 3-9(b2)). In order to investigate the voltage oscillations in a different cell, a single-serpentine cell (JARI cell [20]) was used with a GDL without an MPL (28BA). As shown in Fig. 3-10, the oscillations were also observed in a JARI cell with periods rather irregular.

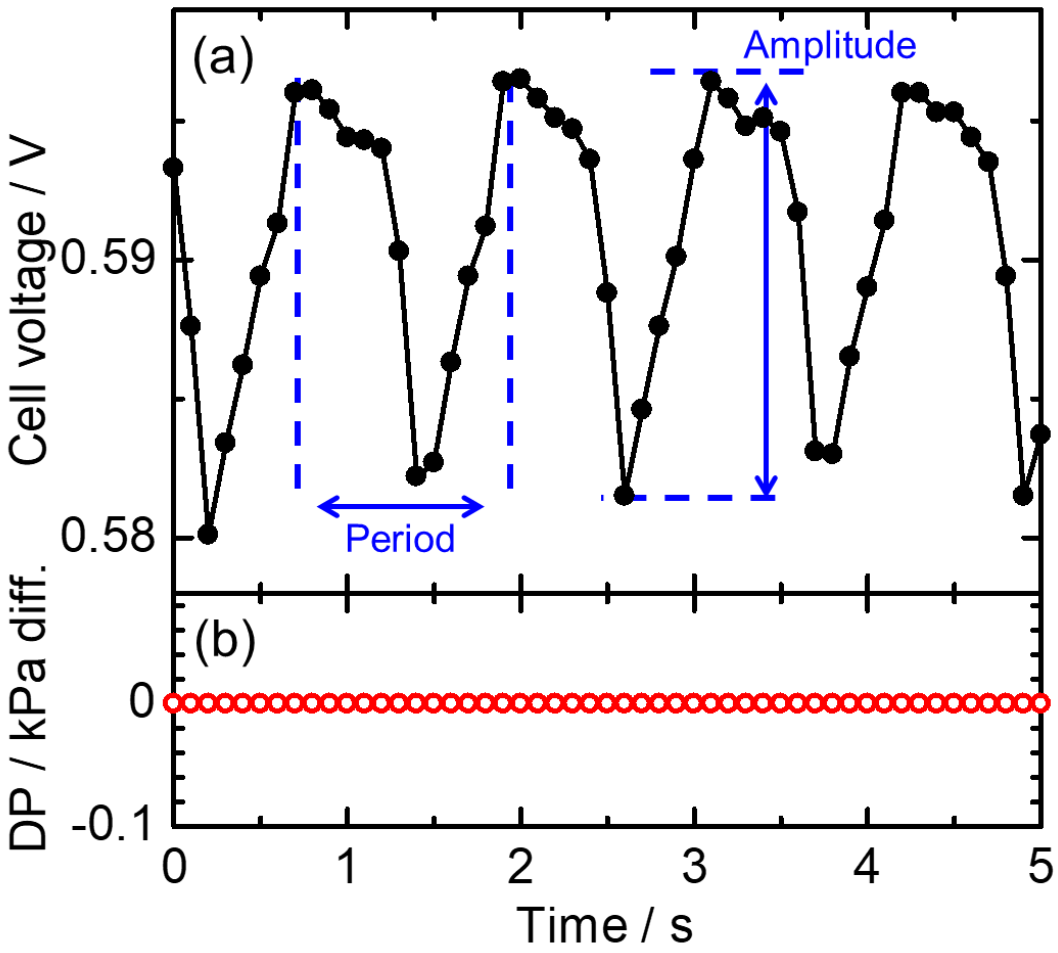

Fig. 3-8 Cell voltage (black filled circles) (a) and differential pressure (DP, red open circles) (b) between cathode inlet and outlet of cell with 28BA (without MPL). Amplitude and period are indicated by blue arrows.

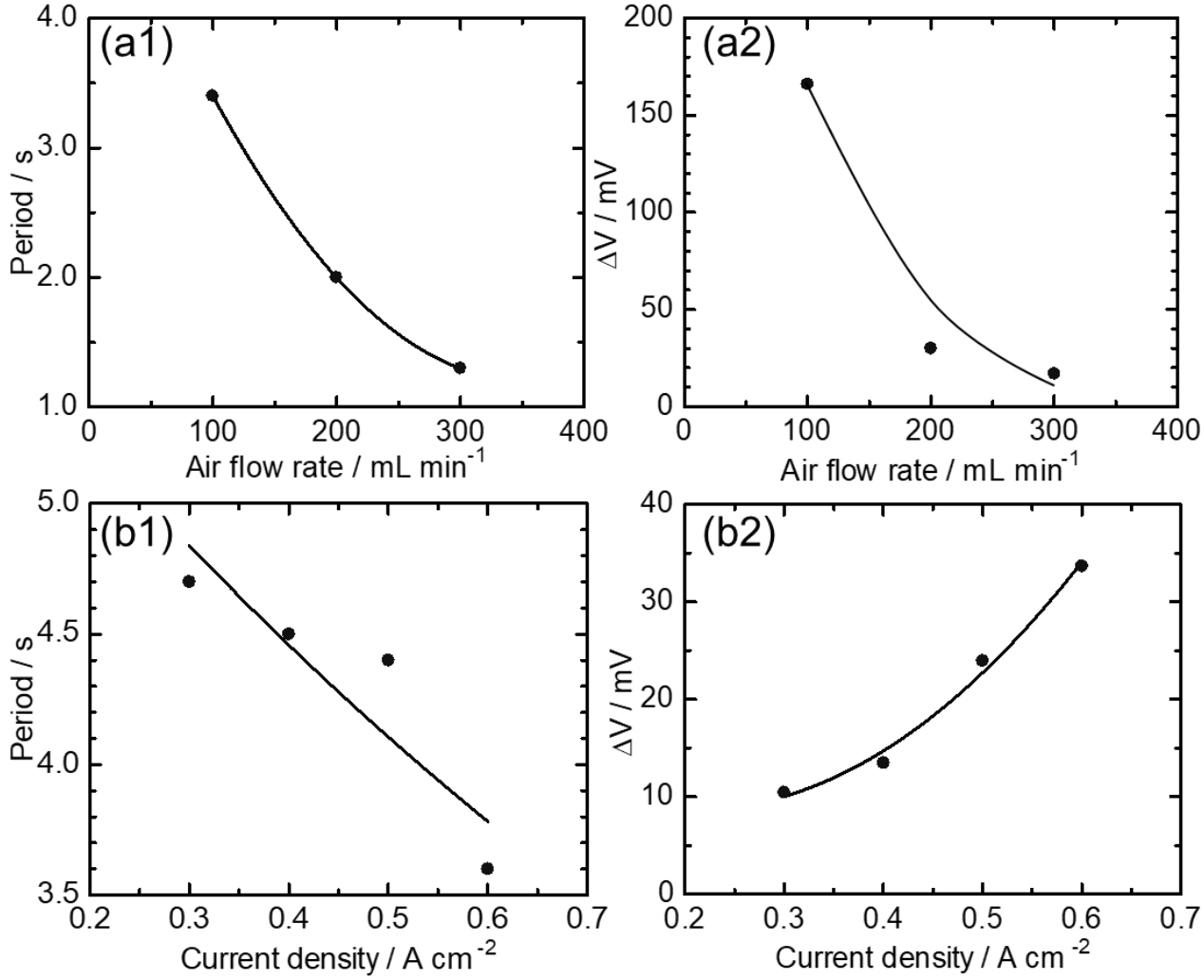

Fig. 3-9 Period (a1) and ΔV (a2) of oscillation vs. air flow rate at cathode. Hydrogen/air = 400/100, 200, and 300 mL min^{-1}. Current density = 0.6 A cm^{-2} (U_{O2} = 19.9%). Period (b1) and ΔV (b2) vs. current density. Hydrogen/air = 400/200 mL min^{-1}. T = 60 ºC and RH = 60% for all measurements. 28BA was used.

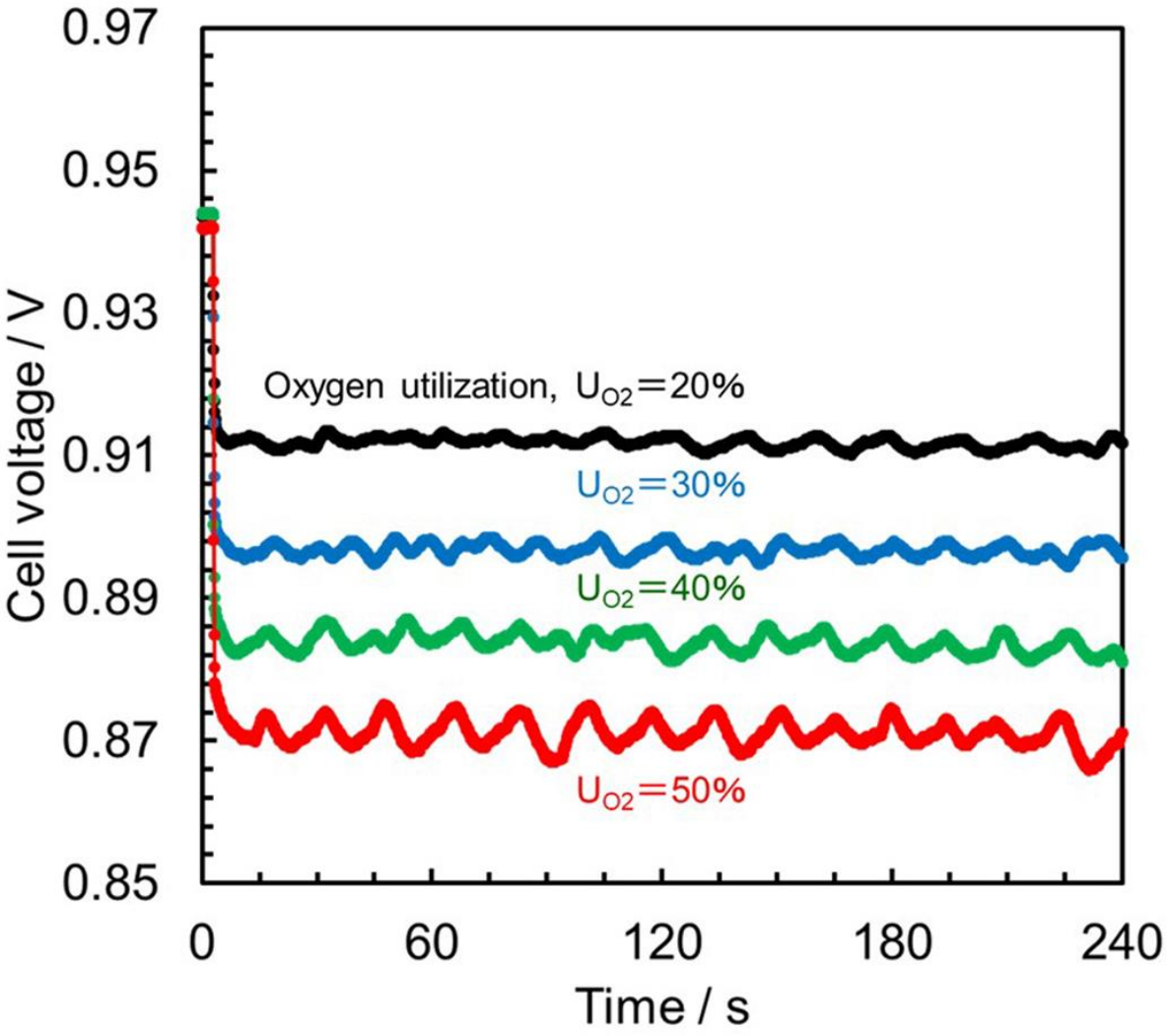

Figure 3-10 Cell voltage oscillated in JARI cell at different U_{O2}. Hydrogen/air = 40/20 mL min^{-1}. Linear velocities of hydrogen/air = 0.66/0.33 m s^{-1}, the same as the linear velocities with 10-straight channel cell. T = 60 °C, RH = 60%.

3.4.2 $p(O_2)$ measurement in gas diffusion layers (GDLs) at different distances from catalyst layer

Figure 3-11 shows $p(O_2)$ inside a GDL without an MPL (28BA) (a) and that with an MPL (28BC) (b), respectively, in a cell obtained at different lateral/vertical probe positions (Fig. 3-4(d)) at 0.6 A cm^{-2} and hydrogen/air = 400/200 mL min^{-1}. The U_{O2} was 19.9%. The measurement points near the inlet are shown in blue, at the center in green, and near the outlet in red, and the measurement points under the flow channels and the ribs are shown by squares and triangles, respectively. The distances between the probe apex and the CL was changed from 100 to 50, 10, and 5 μm, closer to the CL. $p(O_2)$ was measured three times at each location and the averaged value was plotted with bars showing the highest and the lowest values that comes from the oscillation. In 28BA (Fig. 3-11(a)), $p(O_2)$ near the inlet under the flow channel (blue squares, 5.0 μm from the edge of the catalyst area) was nearly constant, 18.6 kPa, regardless of the depth. $p(O_2)$ near the outlet under the flow channel (red squares, 15.0 μm from the edge of the catalyst area) was also nearly constant, 17.0 kPa. The decrease in $p(O_2)$ was 18.6 – 17.0 = 1.6 kPa between the two holes (5.0 and 15.0 mm from the edge of the catalyst area). Since the U_{O2} was 19.9%, the calculated decrease in $p(O_2)$ would be 1.8 kPa assuming the linear consumption of oxygen along the flow channel. Therefore, the consumption of oxygen at nearly a fixed rate along the flow channel was confirmed [15]. Near the inlet under the rib (blue triangles), $p(O_2)$ decreased from 11.5 to 11.2 kPa as the probe approached to the CL (100 to 5 μm). At the center under the rib (green triangles), $p(O_2)$ decrease largely from 11.3 to 9.6 kPa as the probe approached to the CL. Near the outlet under the rib (red triangles), $p(O_2)$ slightly decreased from 13.4 to 13.1 kPa as the probe approached to the CL. Surprisingly, $p(O_2)$ near the outlet under the rib was much higher than that near the

inlet, and $p(O_2)$ at the center was the lowest.

In the case of 28BC (Fig. 3-11(b)), $p(O_2)$ near the inlet under the flow channel (blue squares) were 19.6, 18.7, 17.4, 16.8, and 15.5 kPa at 100, 50, 25, 10, 5 μm from the CL, respectively. $p(O_2)$ clearly decreased as the probe approached to the CL. $p(O_2)$ near the outlet under the flow channel (red squares) decreased from 17.5 to 12.7 kPa as the probe approached to the CL. $p(O_2)$ near the inlet under the rib (blue triangles) slightly decreased from 14.9 to 13.9 kPa as the probe approached to the CL. $p(O_2)$ near the outlet under the rib (red triangles) decreased from 10.2 to 6.6 kPa as the probe approached to the CL.

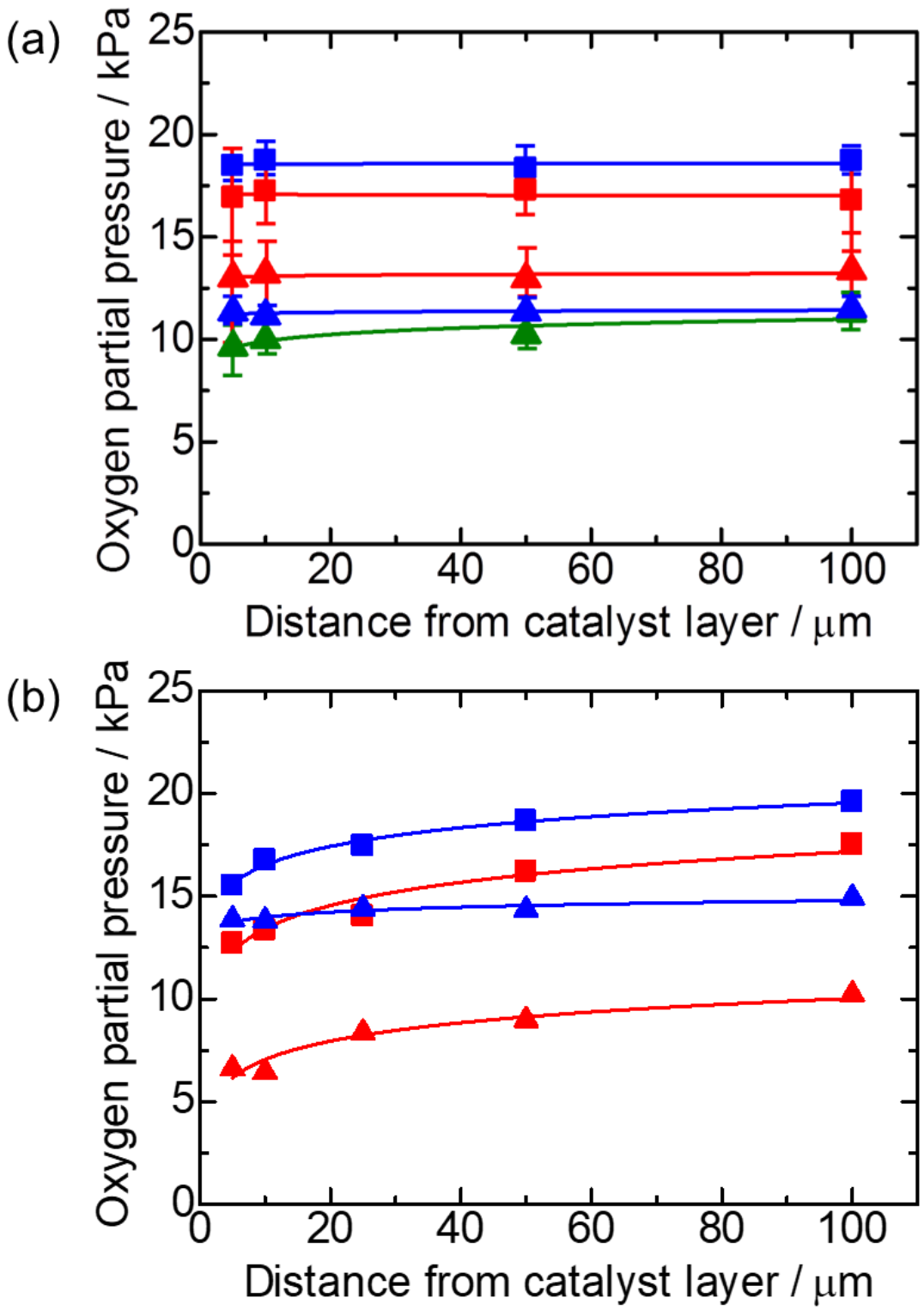

Fig. 3-11 $p(O_2)$ at different locations with different distances from catalyst layer with 28 BA (a) and 28BC (b) at 0.6 A cm^{-2}. $p(O_2)$ at inlet, center and outlet of channels are shown in blue, green and red lines, respectively. $p(O_2)$ under flow channels and ribs are shown by squares and triangles, respectively. See Fig. 3-4 (b).

3.4.3 Oscillated $p(O_2)$ measured in GDLs without/with a micro porous layer (MPL)

Subsequently, the cell voltage and $p(O_2)$ were continuously measured for 20 s at 60 °C, 60% RH, and hydrogen/air = 400/200 mL, before and after the change in current density. The locations of the holes were the same as those shown in Fig. 3-4(b). The apices of the probes were set 10 μm from the CL. The cell voltage are shown by black circles. The $p(O_2)$ values under the flow channels and under the ribs are shown in squares and triangles, respectively, whereas those near the inlet, center, and near the outlet are shown in blue, green, and red, respectively. The current density was abruptly changed from 0.2 to 0.6 A cm^{-2} during the measurements (dashed perpendicular lines) in Fig. 3-12. Figure 3-12(a) shows $p(O_2)$ and the cell voltage with 28BA. At 0.2 A cm^{-2}, the cell voltage was approximately 730 mV with the oscillation amplitude of 2.2 mV and the period of 2.0 s. When the current density was increased to 0.6 A cm^{-2}, the cell voltage suddenly decreased to 534 mV. At the same time, the voltage oscillation became larger with the oscillation amplitude of 16 mV and the period of 2.5 s. The cell voltage gradually increased with the oscillation with the same amplitude and the period. At the increase in current density, $p(O_2)$ abruptly decreased. Under the flow channel near the inlet (blue square), $p(O_2)$ changed from 18.3 to 17.3 kPa and gradually increase up to 19.4 kPa at 20 s.

Under the flow channel near the outlet (red square), $p(O_2)$ changed from 18.5 to 16.2 kPa and gradually increased to 18.6 kPa at 20 s. The average amplitude of $p(O_2)$ under the flow channel and the rib near the outlet were 3.0 kPa. Under the rib near the inlet, $p(O_2)$ decreases from 16.3 to 11.7 kPa and gradually decreased after changing the current density to 0.6 A cm^{-2}. The average amplitude of $p(O_2)$ was 0.1 kPa at 0.6 A cm^{-2}. Under the rib at the center, $p(O_2)$ changed from 15.2 to 10.5 kPa. These values were lower than those near the inlet under the rib both at 0.2 and 0.6 A cm^{-2}. Under the rib near the outlet,

the amplitude of $p(O_2)$ was 1.3 kPa at 0.2 A cm^{-2}. When the current density was changed from 0.2 to 0.6 A cm^{-2}, $p(O_2)$ under the rib near the outlet was significantly decreased from 16.9 to 11.9 kPa and the amplitude became larger from 1.3 to 2.7 kPa. The amplitude became larger from the inlet to the outlet along the flow channel length. Also, the voltage oscillation became larger from 2.2 to 20 mV after the current-density increase. The oscillations of the cell voltage and $p(O_2)$ all synchronized.

The $p(O_2)$ measurement with 28BC is shown in Fig. 3-12(b). After increasing the current density, the voltage and $p(O_2)$ abruptly decreased. The cell voltage decreased from 740 mV to 569 mV. $p(O_2)$ near the inlet under the flow channel and rib and near the outlet under flow channel and rib decreased from 18.3 to 16.4 kPa, from 15.6 to 13.4 kPa, from 17.4 to 14.8 kPa, and from 11.0 to 7.1 kPa, respectively. Subsequently, $p(O_2)$ under the flow channels gradually increased and $p(O_2)$ under the ribs slowly decreased. The voltage and the $p(O_2)$ did not oscillate. The cell voltage became about 0.59 V at 0.6 A cm^{-2}. In comparison to the GDL 28BA, the overvoltage became smaller by 0.02 V. The oscillation of $p(O_2)$ was not observed under any condition.

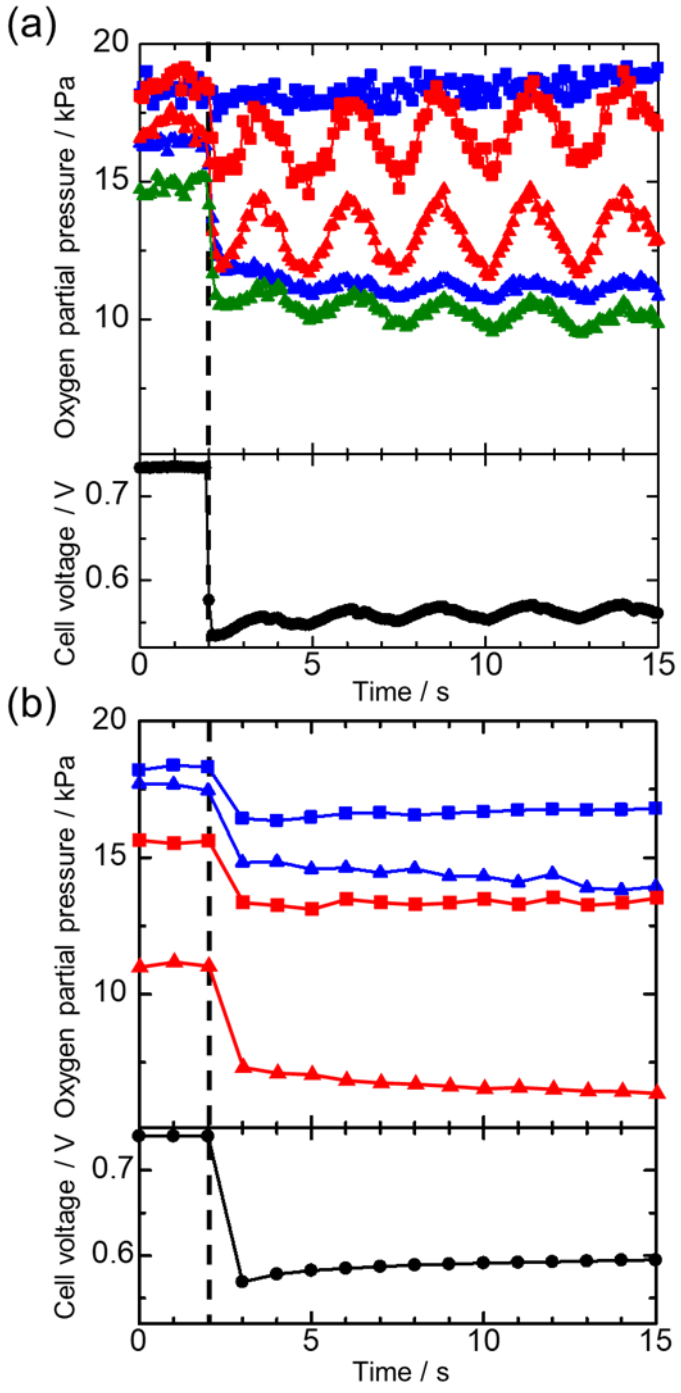

Fig. 3-12 Cell voltage and $p(O_2)$ at different measurement points using 28BA (a) and 28BC (b). Cell voltages are shown by black circles. Optical probe was located at 10 μm from catalyst layer. Current density was changed from 0.2 to 0.6 A cm^{-2} (U_{O2} was 6.6 to 19.9%, respectively) at 2 s in graphs. T = 60 °C and RH =60%. Hydrogen/air = 400/200 mL min^{-1}. $p(O_2)$ at inlet, center and outlet of channels are shown in blue, green and red lines, respectively. $p(O_2)$ under flow channels and ribs are shown by squares and triangles.

3.4.4 Increase in $p(O_2)$ near outlet under the rib

Interestingly, under the rib, $p(O_2)$ was higher near the outlet (triangle, red line) than those near the inlet (triangle, blue line) and at the middle (triangle, red line) as shown in Figs. 3-11(a) and 3-12(a), whereas $p(O_2)$ under the flow channels gradually decreased along the flow channel by the oxygen consumption. $p(O_2)$ under the rib was naturally lower than that under the flow channel, because the oxygen diffusion from the flow channel beneath the rib was lowered by the existence of the rib itself.

It should be noted that the amount of oxygen is generally determined by the oxygen supply from the flow channel and the consumption at the CL. The U_{O2} was only 19.9 % even at 0.6 A cm^{-2}, and $p(O_2)$ in the flow channel accordingly decreased from the inlet to the outlet under this operating condition. Under the rib, $p(O_2)$ decreased from the inlet to the middle and increased near the outlet along the channel length (Figs. 3-11(a) and 3-12(a)). This might be indicating that the oxygen consumption at the CL near the outlet was very small, probably because of the accumulation of liquid water in the CL. The model is illustrated in Fig. 3-13. For understanding the oscillation phenomena, the existence of liquid water must be taken into account.

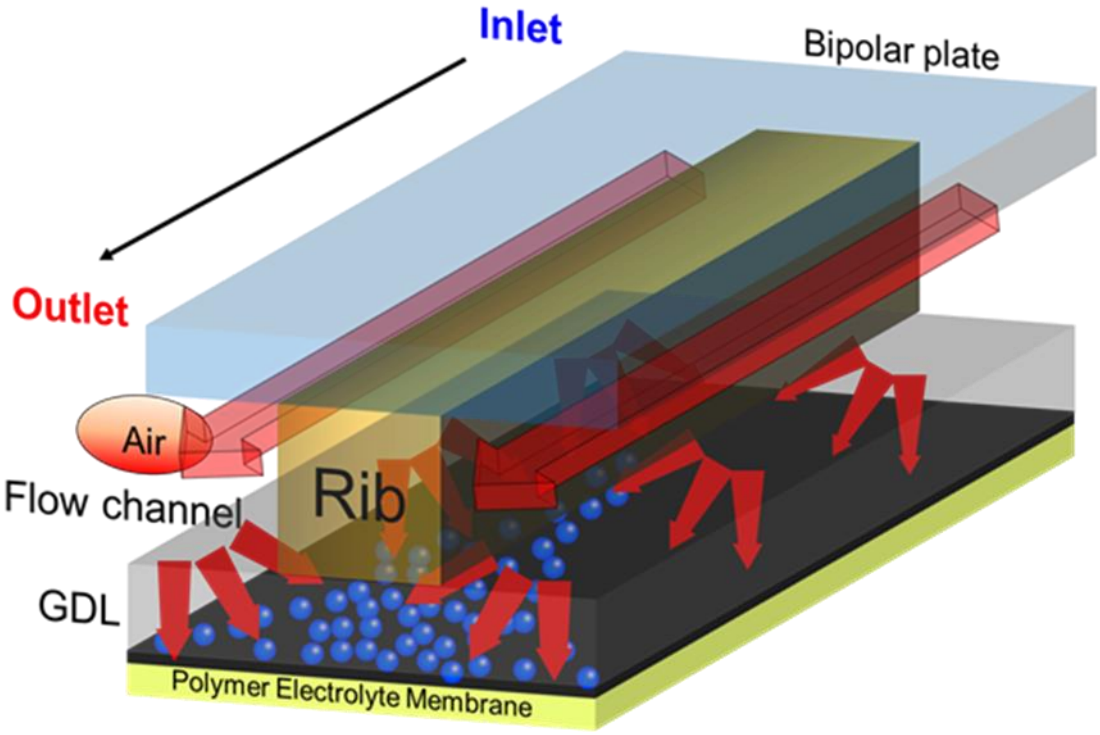

Figure 3-13 Schematic illustration of accumulation of water under rib near outlet.

3.4.5 Mechanism of synchronized oscillation of cell voltage and $p(O_2)$

As shown in Fig. 3-12(a), the cell voltage was oscillated clearly and distinctly in a cell with 28BA, and $p(O_2)$ synchronized with voltage under the flow channel and under the rib. However, the differential pressure was lower than the detection limit, which means that the excess water did not exist in the flow channels. Therefore, the amplitudes of the oscillations of both voltage and $p(O_2)$ became larger at 0.6 A cm^{-2} than at 0.2 A cm^{-2}. The amplitude of the $p(O_2)$ oscillation became larger from the inlet to the outlet. As discussed in the previous section, the accumulation of water in the CL could be the key to understand those oscillations. The mechanism of the oscillation of the cell voltage and $p(O_2)$ in a PEMFC with a GDL without an MPL is depicted in Fig. 3-14(a). The cell was operated at a constant current density. The generated water increased and accumulated in the CL especially near the outlet, and the air permeation was lowered. In order to keep a constant current density, the overvoltage became larger and the heat was generated at the CL. Subsequently, the liquid water in the CL was removed as water vapor from the CL to the GDL. The temperature at the CL was then lowered by the heat of evaporation. By repeating this cycle, the voltage oscillated. When liquid water turned into vaper, $p(O_2)$ in the GDL decreased. $p(O_2)$ inside PEMFC is determined by the total pressure, $p(N_2)$, and $p(H_2O)$. Therefore, when $p(H_2O)$ oscillates, $p(O_2)$ accompanies. In my model, the temperature of the CL should oscillate during voltage oscillation, which should be examined separately.

To explain a dynamical system, the van der Pol equation (eq. 3-1) is commonly used.

$$\frac{d^2x}{dt^2} - \mu\,(1 - x^2)\,\frac{dx}{dt} + x = 0 \qquad \text{(eq. 3-1)}$$

where x is the state variable (a function of the time t) and μ is a scalar parameter indicating the nonlinearity and the strength of the damping. There are three cases depending on the

sign of μ.

(1) $\mu > 0$ Limit cycle

(2) $\mu = 0$ Single oscillation (harmonic oscillation)

(3) $\mu < 0$ Damped vibration

In the oscillation phenomena of this thesis, $\mu > 0$ because voltage oscillation took the limit cycle state. The limit cycle must have a zero-energy balance. In this case, the voltage might oscillate by the balance of amount of accumulation water and generated heat in the CL. Liquid water accumulates in the catalyst layer and the effective catalyst area for the power generation decreases, as a result the voltage decreases. In other words, the current density distribution in the MEA might oscillate. When the voltage starts to increase, the amount of heat generated increases as the current density increases, then the accumulated liquid water in the CL evaporates. The influence of oxygen at the CL on the cell voltage was recently reported by using *operando* coherent anti-stokes Raman scattering spectroscopy during power generation [21].

A schematic model of the water evacuation from the CL using a GDL with an MPL is shown in Fig. 3-14(b). Liquid water was easily removed from the CL by the capillary phenomenon of the MPL, so the voltage oscillation was not observed. The overvoltage was also kept low compared to that with the GDL without an MPL.

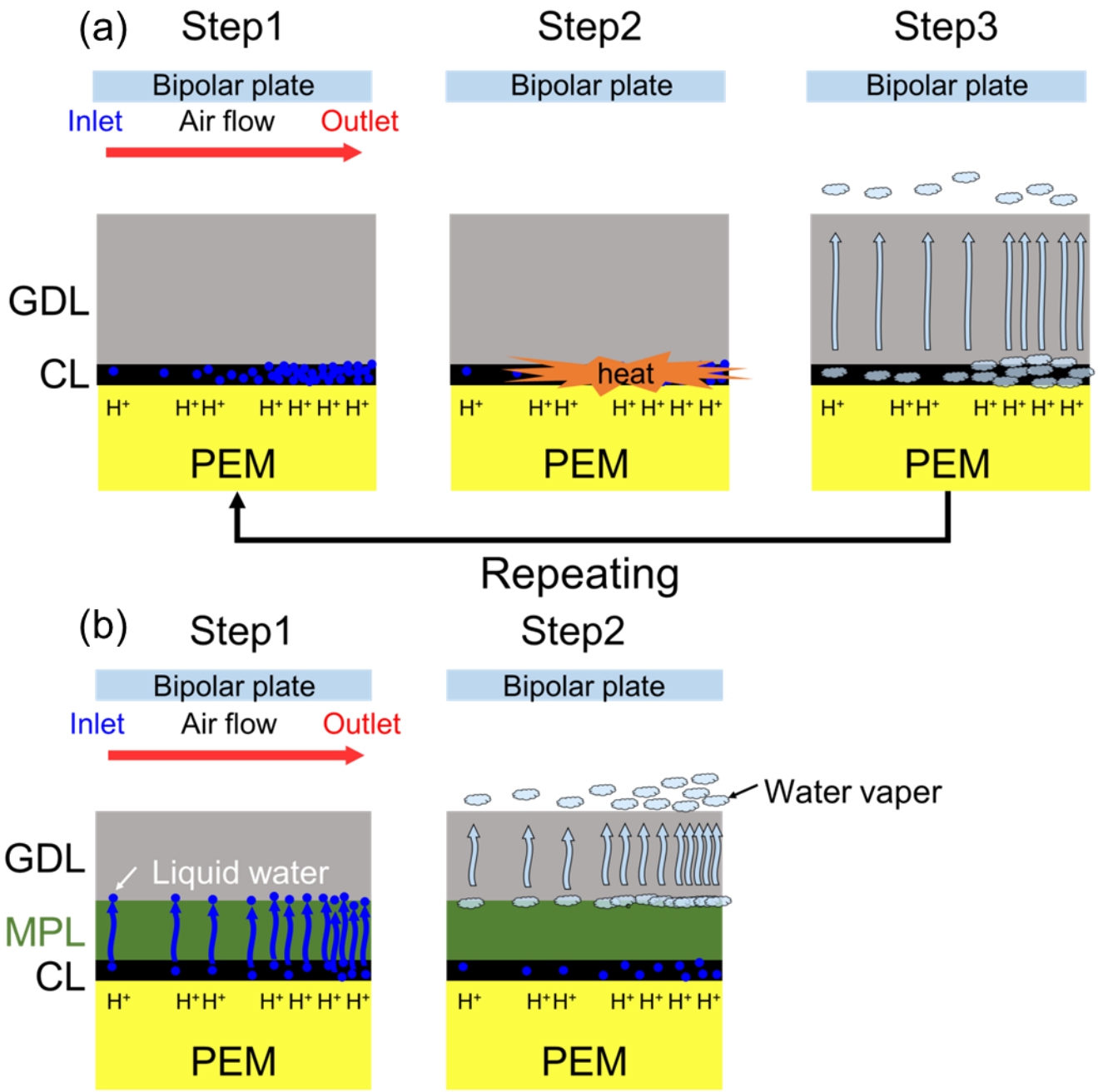

Fig. 3-14 Schematic illustrations of oscillation mechanism inside the PEMFCs using 28BA (a) and 28BC (b).

3.4.6 Oscillations under different conditions

When water accumulates too much in the cathode CL, the oxygen reduction reaction (ORR) is inhibited, and the ORR proceeds where water does not accumulate. The period and amplitude of the voltage oscillation depended on the balance between the amount of generated water and heat by the power generation. Figures 3-9(a1) and (a2) show the dependency of the period and amplitude of the oscillating voltage on the air flow rate. Both the period and the amplitude decreased with increasing the air flow rate. This can be explained by an easier removal of the accumulated water at a high air flow rate; at a constant current density, the amount of generated water was constant, so the region of the accumulation and the amount of water in the CL changed. At high flow rates, the region of accumulated water might be limited only near the gas outlet. In contrast, under low flows, the amount of accumulated water became larger and the accumulation region was expected to expand near to the center of the MEA. Especially under the ribs, water accumulation was more likely to occur, because the gas diffusion was limited by the existence of ribs. In this way, the period of the voltage oscillation at high flow rates was shortened, because the accumulated region was smaller than that at low flow rates. In addition, the amplitude of the voltage oscillation at high flow rates decreased due to the smaller concentration overvoltage because of the decrease in the accumulation of water.

As seen in Figs. 3-9(b1) and (b2), the period and amplitude depended on the current density. As explained in Fig. 3-9(a2), the concentration overvoltage increased probably due to the increase in generated water in the CL. Therefore, the generated heat also increased with the increase in overvoltage with the current density increase. The accumulated water was rapidly removed by the generated heat, thus the period was shortened. The voltage oscillation amplitude increased with current density. As explained

with Figs. 3-9(a2), the ORR should be inhibited more as the water accumulation regions increased by the generated water in the CL at high current densities, where the concentration overvoltage increased and the amplitude of cell voltage oscillation became larger. In these ways, the cathode air flow rate and current density were understood to influence the period and amplitude of the voltage oscillation.

3.5 Conclusions

A new oscillation phenomenon was found, when a PEMFC with 10 straight channels was operated at 60 °C and 60% RH using a GDL without an MPL. The cell voltage oscillated periodically under a constant-current operation; the period and amplitude were approximately 2 s and 20 mV, respectively. The pressure difference between the inlet and the outlet of the cathode was not observed during the voltage oscillation. Therefore, the influence of liquid water was not the origin of the oscillation [4,10,14]. The period and amplitude of the voltage oscillation were investigated by changing the cathode air flow rate and the current density. The period and amplitude decreased as the air flow increased. The period became a volcano shape when the current density increased. The amplitude monotonously decreased with increasing current density.

In order to study this voltage oscillation, an *operando* system was developed for detecting $p(O_2)$ using optical probes. $p(O_2)$ during the oscillation synchronized with the cell voltage. The amplitude of the oscillation of $p(O_2)$ was the largest under the rib and near the outlet. During the oscillation, the generated water was proposed to increase and accumulate in the CL of the cathode, accordingly inhibiting the transport and reduction reaction of oxygen. The cell voltage was lowered with a larger overvoltage, resulting in the heat in the CL, by which the liquid water having accumulated in the CL was removed

as water vapor to the GDL. The oscillation phenomena is likely to be more pronounced in the future operation of PEMFCs at high current densities. The mechanisms proposed in this paper could be applied to the water management in the CL and the GDL, as well as for optimizing the PEMFC operation.

References

[1] N. Yousfi-Steiner, P. Moçotéguy, D. Candusso, D. Hissel, A. Hernandez, A. Aslanides, J. Power Sources 183 (2008) 260–274.

[2] W. Schmittinger, A. Vahidi, J. Power Sources 180 (2008) 1–14.

[3] F. Barbir, H. Gorgun, X. Wang, J. Power Sources 141 (2005) 96–101.

[4] S. Hirakata, T. Mochizuki, M. Uchida, H. Uchida, M. Watanabe, Electrochim. Acta 108 (2013) 304–312.

[5] D. G. Sanchez, D. G. Diaz, R. Hiesgen, I. Wehl, K. A. Friedrich, J. Electroanal. Chem. 649 (2010) 219–231.

[6] D. G. Sanchez, A. Ortiz, K. A. Friedrich, J. Electrochem. Soc. 160 (2013) 636–644.

[7] P. A. García-Salaberri, D. G. Sánchez, P. Boillat, M. Vera, K. A. Friedrich, J. Power Sources 359 (2017) 634–655.

[8] J. R. Atkins, S. C. Savett, S. E. Creager, J. Power Sources 128 (2004) 201–207.

[9] J. Inukai, K. Miyatake, K. Takada, M. Watanabe, T. Hyakutake, H. Nishide, Y. Nagumo, M. Watanabe, M. Aoki, H. Takano, Angew. Chemie - Int. Ed. 47 (2008) 2792–2795.

[10] K. Takada, Y. Ishigami, J. Inukai, Y. Nagumo, H. Takano, H. Nishide, M. Watanabe, J. Power Sources 196 (2011) 2635–2639.

[11] Y. Ishigami, W. Waskitoaji, M. Yoneda, K. Takada, T. Hyakutake, T. Suga, M. Uchida, Y. Nagumo, J. Inukai, H. Nishide, M. Watanabe, J. Power Sources 269 (2014) 556–564.

[12] K. Nagase, H. Motegi, M. Yoneda, Y. Nagumo, T. Suga, M. Uchida, J. Inukai, H. Nishide, M. Watanabe, ChemElectroChem 2 (2015) 1495–1501.

[13] K. Nagase, T. Suga, Y. Nagumo, M. Uchida, J. Inukai, H. Nishide, M. Watanabe, J. Power Sources 273 (2015) 873–877.

[14] K. Takanohashi, T. Suga, M. Uchida, T. Ueda, Y. Nagumo, J. Inukai, H. Nishide, M. Watanabe, J. Power Sources 343 (2017) 135–141.

[15] T. Kobayashi, M. Uchida, J. Inukai, Y. Nakama, T. Ohno, Y. Nagumo, M. Teranishi, M. Yoneda, J. Takano, T. Saiki, T. Suga, H. Nishide, M. Watanabea, 226th Meet. Electrochem. Soc. (2014) 1158.

[16] K. Takanohashi, M. Uchida, A. Iiyama, J. Inukai, J. Surf. Finish. Soc. Jpn. 68 (2017) 338–343.

[17] Y. Kakizawa, C. L. Schreiber, S. Takamuku, M. Uchida, A. Iiyama, J. Inukai, J. Power Sources 483 (2021) 229193.

[18] W. K. Epting, S. Litster, J. Power Sources 306 (2016) 674–684.

[19] W. K. Epting, S. Litster, 224th Meet. Electrochem. Soc. (2012) 1541.

[20] Y. Hashimasa, T. Numata, K. Moriya, S. Watanabe, J. Power Sources 155 (2006) 182–189.

[21] H. Nishiyama, S. Takamuku, A. Iiyama, and J. Inukai, J. Phys. Chem. C 124 (2020) 19508–19513.

Chapter 4

Neutron imaging of water distributions inside running PEMFCs with Pt/CB and Pt/Nb-SnO_2 as cathode catalysts

4.1 Introduction

As describe in General Introduction, improving the catalyst durability of is still mandatory to reduce the cost of fuel cell stacks. Platinum-based catalysts supported on carbon undergo degradation under operating conditions of low pH, high humidity, and high potential [1,2]. One of the degradation reactions is corrosion of the carbon support by oxidation [3,4] resulting from the thermodynamic instability [5–7]. The corrosion also accelerates the aggregation of Pt metal particles on the carbon support and/or the actual loss from the support [8]. In order to avoid the carbon corrosion, Pt catalyst formed on Nb-doped SnO_2 support (Pt/Nb-SnO_2) was synthesized [9–11]. However, as shown in Fig. 4-1, the I-V performance corrected for IR loss with the Pt/Nb-SnO_2 at the cathode was not as high as that with platinum catalyst supported on carbon black (Pt/CB). The activity of both catalysts was comparable [12]. Therefore, the difference in the I-V performance could be due to the mass transport. Figure 4-2 shows the absorption of water vapor on SnO_2 and CB. From the data, it was understood that the surface of SnO_2 was more hydrophilic than that of CB. In this chapter, the liquid water distributions inside the MEA imaged using neutron beams are analyzed to elucidate the mechanism arising the difference in the I-V performance of the cells with Pt/CB and Pt/Nb-SnO_2 at the cathode. Compared to X-ray, neutron has a higher penetration ability. The cross section of H atoms is also high, which makes neutron a suitable source to be used for visualizing water inside PEMFC.

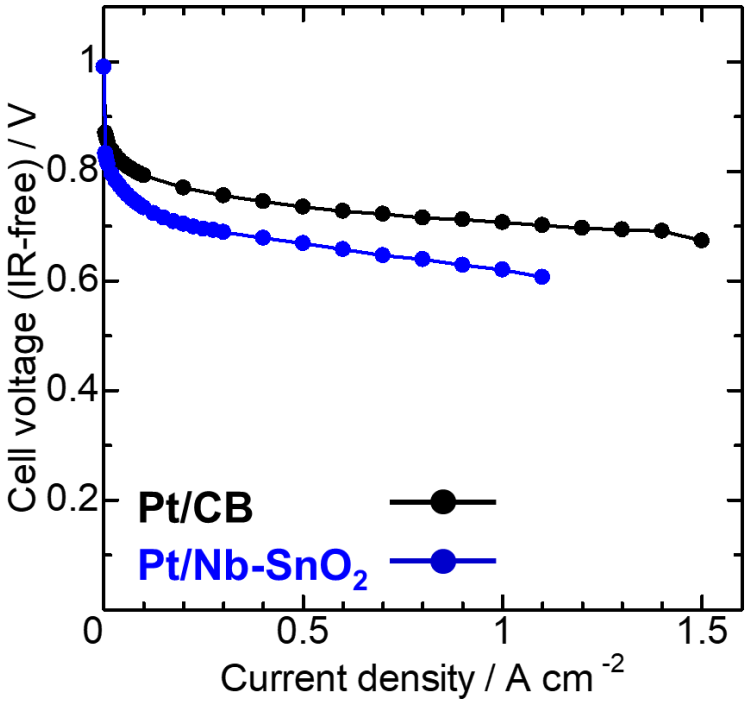

Fig. 4-1 IV performances with Pt/CB and Pt/Nb-SnO_2 catalysts at cathode. Cell temperature = 80°C, relative humidity = 80%, hydrogen/oxygen flow rates = 100/200 L min^{-1}.

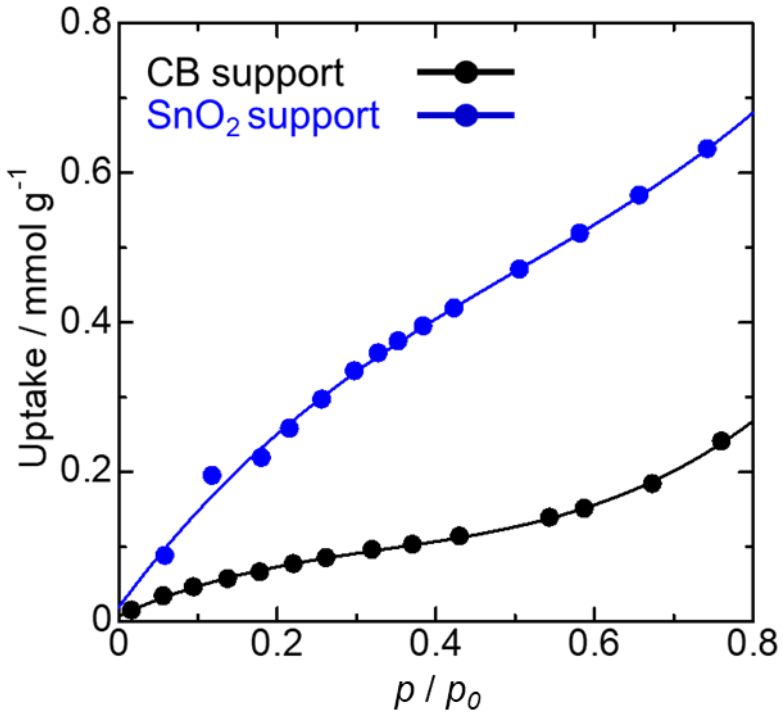

Fig. 4-2 Water vapor adsorption in CB and SnO_2 powders. Temperature = 25°C.

4.2 Experimental

4.2.1 Transmission electron microscopy (TEM) and scanning ion microscopy (SIM)

Pt/CB and Pt/Nb-SnO_2 catalysts covered with Nafion were observed using a transmission electron microscope (TEM, HT7700, Hitachi High Technologies Co.) operated at 80 kV. The scanning ion microscopy (SIM) images of the CLs were obtained using a FB2200 (Hitachi High Technologies Co.) operated at 40 kV using Ga ions. The CLs were cut out by focused ion beam. The extreme surfaces of CLs were coated by carbon and tungsten to suppress the corrosion of CL surfaces during the cross-section processing.

4.2.2 Fuel cell assembly, activation, and cyclic voltammetry

For neutron transmission, the end-plate and current collectors were made of aluminum alloy (A7075). The current collectors were plated with gold with the thickness of 10 μm. The width and height of a single-serpentine flow channel were both 1.0 mm formed by carving the current collector. The width of ribs was 1.0 mm. A Kapton® film, 200 μm in thickness, isolated the end-plate and the current collector. The catalyst-coated membrane consisted of a Nafion membrane (NRE 212, 50 μm thickness, DuPont, U.S.A.) sandwiched by layers of Pt catalysts mixed with a 5wt% Nafion solution (ion exchange capacity = 0.9 meq g^{-1} D-521, DuPont, U.S.A.). For the cathode catalysts, commercial Pt/CB (46.3 wt%-Pt, TEC10E50E, Tanaka Kikinzoku Kogyo K.K., Japan) and Pt/Nb-SnO_2 synthesized by the colloid method in our laboratory [9-12] were used. For the anode catalysts, Pt/CB was used. The volume ratios of Nafion ionomer (dry basis) to the support (I/S) were adjusted to 0.7 and 0.24 for Pt/CB and Pt/Nb-SnO_2, respectively. As the GDL

with an MPL, 29BC of SIGRACET (SGL Carbon Group Co., Ltd., Germany) was used. The active area of the catalyst layer was 20 × 20 mm^2. The compression pressure of the MEA was 10 kgf cm^{-2}. A ceramic heater (WALN-14, SAKAGUCHI E.H VOC Corp., Japan) was used to control the PEMFC temperature.

During the I-V performance tests before neutron imaging at the beamline, the cell temperature and RH were set at 80 ºC and 80%, respectively, with oxygen and hydrogen gas flow rates at 200 and 400 mL min^{-1}, respectively, using a fuel cell evaluation system (As-540-340PE, nF Corporation, Japan). Before measuring CVs at the cathode, both hydrogen and nitrogen gases were supplied at 200 mL min^{-1} at the anode and cathode, respectively; only the nitrogen gas was stopped during the CV measurements between 0.075 and 1.000 V (vs. the hydrogen electrode) with a scan rate of 20 mV s^{-1}.

4.2.3 Calibration curve for water

For quantifying water inside PEMFC, a calibration curve was obtained by using quartz cells (Stana scientific Ltd., U.K.) with different optical pass lengths of 0.5, 0.1 and 0.01 mm, located beside the PEMFC. At BL22 of MLF, J-PARC, Japan, the neutron beam was supplied as 25-Hz pulses and captured by a CCD camera. 8000 pulses of neutron beam were integrated for a neutron transmission image, or the exposure time was 320 s/image. The neutron transmission images of the quartz cells with/without water inside were obtained, where the images without water were used to subtract the background. Details of the image processing are described in Section 4.2.5.

4.2.4 Water imaging during power generation

Neutron beam power was 600 kW. The wavelength of 5-13.5 Å was used for imaging.

The imaging area was 5×5 cm^2 (2048×2048 pixels). Therefore, 1 pixel corresponded to 24 μm. The overall special resolution was 100 μm [13].

During the imaging, the cell temperature and RH were set at 80 ºC and 80%, respectively. The gases were supplied as in Table 1. The current density was set at 0.1, 0.5, and 1.0 A cm^{-2} by an electric road (PLZ164WA, Keisoku Giken, Japan). The gas flow rate was controlled by a fuel cell evaluation system (HPE-1000, FC development Co, Ltd., Japan). Unused hydrogen was exhausted from the beamline hatch after diluted by nitrogen below the explosion limit. A digital ac milliohmmeter at a constant frequency of 10 Hz (Model 365E, Tsuruga Electric. Co., Japan) was used to obtain the cell resistance with Pt/Nb-SnO_2. For a cell with Pt/CB, a digital ac milliohmmeter with a constant frequency of 1 kHz (Model 356, Tsuruga Electric. Co., Japan) was used [11].

Table 1 Gas flow conditions and utilizations.

Current density / A cm^{-2}	H_2 flow rate / mL min^{-1}, utilization	O_2 flow rate / mL min^{-1}, utilization
0.1	30, 9.6%	60, 2.4%
0.5	30, 48%	60, 12%
1.0	40, 70%	166, 40%

4.2.5 Image analysis

ImageJ software was used for the image analysis. The dark current at each pixel of a CCD camera was subtracted. The image was subsequently normalized by the intensity of the proton beam generating the neutron beam and further by the average intensity of the areas of the cell where no MEA existed. From the neutron transmittance images measured

for 6 hours, the standard deviation was calculated at pixels to be 0.35%.

4.3 Results and discussion

4.3.1 Cyclic voltammograms, TEM images, and SIM images

Figure 4-3 shows the cyclic voltammograms of Pt/CB and Pt/Nb-SnO_2 in PEMFCs. The electrochemical active surface areas (ECAs) of Pt/CB and Pt/Nb-SnO_2 calculated from the hydrogen desorption peak (0.4 - 0.075 V) were 62.5 and 45.8 $m^2\ g_{Pt}^{-1}$, respectively. The average Pt diameter of TEC10E50E was 2.1 nm obtained by TEM images [14], whereas that of synthesized Pt/Nb-SnO_2 was 3.2 nm. The calculated surface areas of Pt/CB and Pt/Nb-SnO_2 from TEM images were 133 and 88 $m^2\ g_{Pt}^{-1}$, respectively, both larger than the ECAs. The ratios of the surfaces electrochemically active were calculated as 47 and 52 % for Pt/CB and Pt/Nb-SnO_2, respectively.

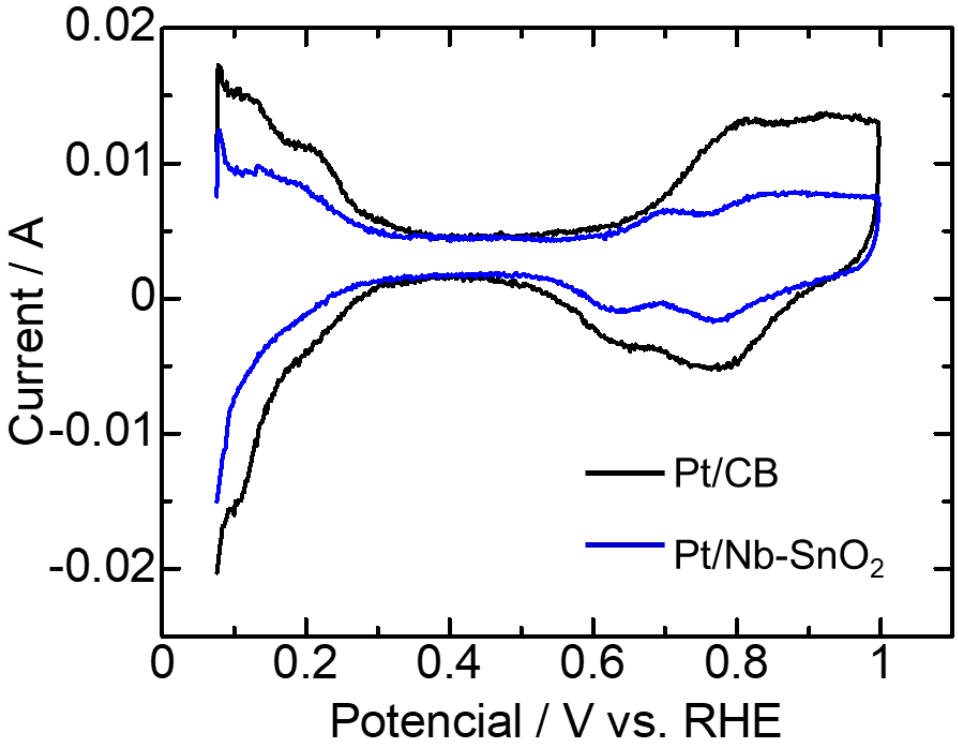

Fig.4-3 Cyclic voltamograms of Pt/CB and Pt/Nb-SnO_2 in PEMFCs at 80ºC 80%RH.

Figures 4-4(a), (b) and (c), (d) show high resolution TEM images of Pt/CB and Pt/Nb-SnO_2 covered with Nafion ionomers, respectively. The red solid lines show the ionomer/catalyst boundaries, whereas the yellow dashed lines the Nafion binder surfaces surrounding catalysts. From these data, the Nafion ionomers covered approximately half the surfaces of Pt/CB and Pt/Nb-SnO_2. In the case of Pt/CB, the binder inhomogeneously covered the catalyst (Fig. 4-4(b)), whereas it covered the Pt/Nb-SnO_2 surface more uniformly (Fig.4-4(d)) as previously reported [15].

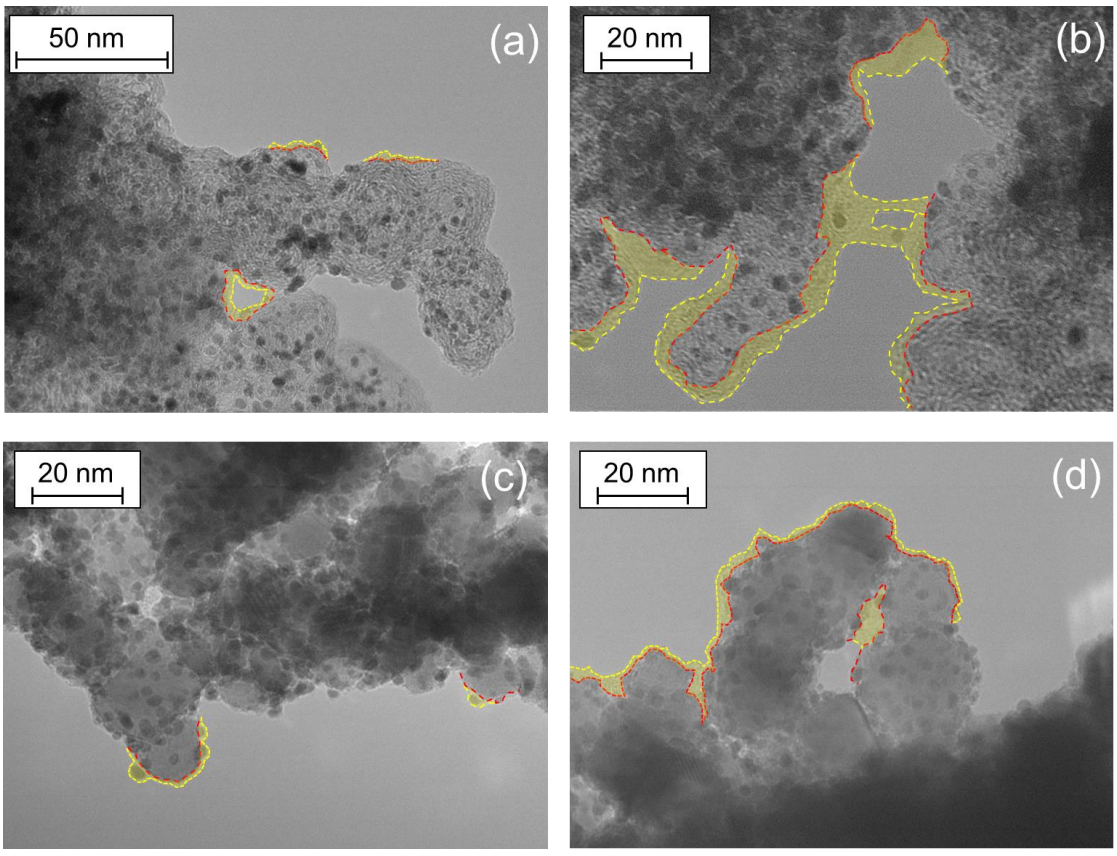

Fig. 4-4 TEM images of Pt/CB (a), (b) and Pt/Nb-SnO_2 (c), (d) with Nafion binders.

The SIM images of the Pt/CB and Pt/Nb-SnO_2 catalyst layers are shown in Fig. 4-5. The average thicknesses of the Pt/CB and Pt/Nb-SnO_2 CLs were 6.2 and 4.4 μm, respectively. Therefore, the pore volume of the Pt/Nb-SnO_2 CL should be smaller than that of Pt/CB [12]. If the same thickness of water is generated at the same current density, the Nb-SnO_2 support should attract a larger amount of water.

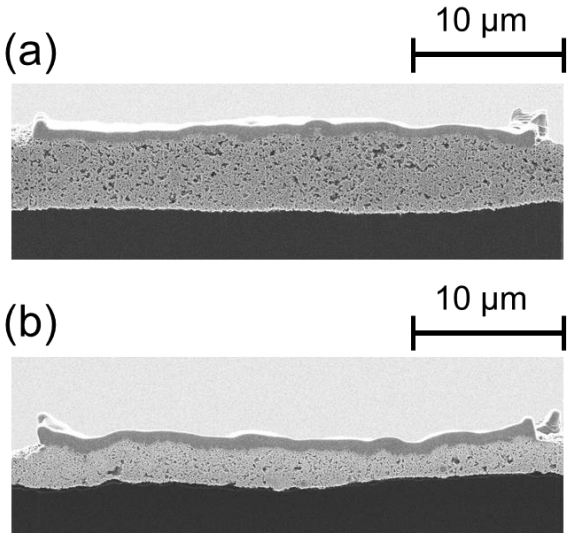

Fig. 4-5 SIM images of cathode CLs of Pt/CB (a) and Pt/Nb-SnO_2 (b).

4.3.2 Neutron imaging during power generation

Figure 4-6 shows the calibration curve obtained by the procedure described in Section 4.2.3. Figures 4-7(a), (b), and (c) are neutron images with Pt/CB at 0.1, 0.5, and 1.0 A cm^{-2}, respectively. The flow channels are indicated by white dashed lines. The thickness of water is represented by color (the color bar on the right). Water at 0.1 A cm^{-2} was observed to be uniformly distributed throughout the cell with the thickness of 16-18 μm (Fig. 4-7(a)). The water thickness contained inside a Nafion NRE212 membrane at 80 ºC and 80% RH was separately calculated as 12 μm by measuring the mass [16], therefore, the water thickness of 16-20 μm at 0.1 A cm^{-2} was reasonable. At 0.5 A cm^{-2} (Fig. 4-7(b)), the

water content increased specifically near the outlet under the ribs with the thickness of 50 μm. Water droplets were generated, as indicated by yellow rectangles in Fig. 4-7(b). Some droplets were seen accumulated on the left side and the bottom edge out of the MEA because of a slight gap between the MEA and the gasket; the sizes of the gasket window and the MEA were 20.5×20.5 mm^2 and 20.0×20.0 mm^2, respectively. In addition, water droplets were seen on the rib walls near the outlet of the flow channel. The generated water droplets may have adhered to the flow channel wall [17]. In the flow channel, water droplets increased in size and number even up to the center of the MEA. At the outlet, the region with the water thickness $\geqq$200 μm appeared, but the flow channel was not blocked.

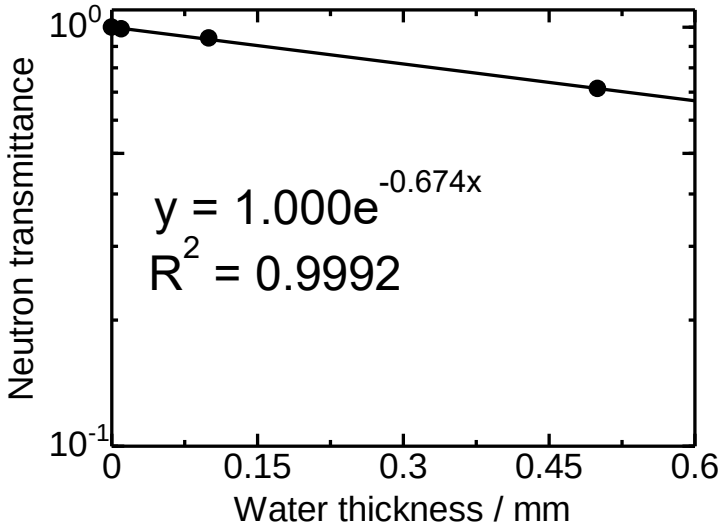

Fig. 4-6 Calibration curve of water inside PEMFC.

Figures 4-7(d), (e), and (f) show transmission images with Pt/Nb-SnO_2 at 0.1, 0.5, and 1.0 A cm^{-2}, respectively. At 0.1 A cm^{-2}, water was uniformly distributed throughout the MEA as with Pt/CB (Fig. 4-7(a)) with the thickness of 18-20 μm. At 0.5 A cm^{-2}, the water droplets were generated on the rib walls near the outlet. At 0.5 and 1.0 A cm^{-2}, the numbers

of water droplets were larger than those with Pt/CB. At 1.0 cm^{-2} , the areas in red (≧200 μm) were relatively smaller than those with Pt/CB. When the current density was increased to 1.0 A cm^{-2}, the differences of water distributions were not obvious between the cells with two different supports because of a large amount of liquid water existing in the flow channel, which practically is determined by the current density and the cell design.

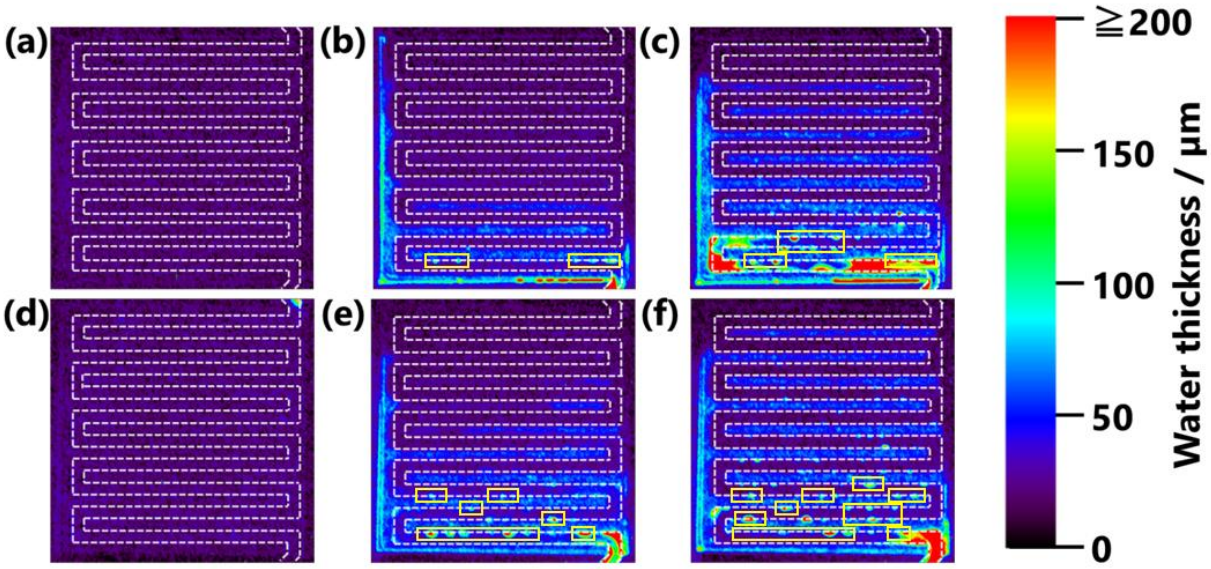

Fig. 4-7 Neutron transmittance images of 4.0 cm^{-2} MEA with Pt/CB during power generation at 0.1 (a), 0.5 (b), and 1.0 A cm^{-2} (c), and with Pt/Nb-SnO_2 at 0.1 (d), 0.5 (e), and 1.0 A cm^{-2} (f). The water thickness is shown by the color bar.

In contrast, at 0.5 A cm^{-2}, the amount of liquid water observed with Pt/Nb-SnO_2 (Fig. 4-7(e)) was clearly larger than that with Pt/CB (Fig. 4-7(b)), even though the current density was the same. To observe the water droplets more carefully, neutron transmittance images with Pt/CB and Pt/Nb-SnO_2 near the outlet at 0.5 A cm^{-2} were enlarged as shown in Figs. 4-8(a) and (b). Water droplets were generally seen on the rib walls, and smaller ones were attached to the intersections of the rib and the flow channel. The number of water droplets and the total water volume are shown in Fig. 4-8(c) and (d), respectively. The numbers of

water droplet with Pt/CB and Pt/Nb-SnO_2 were 9 and 33, respectively. The total water volume of Pt/CB and Pt/Nb-SnO_2 were 7.0 and 31.6 μL, respectively. These water droplets should have been formed under the ribs and the flow channel by the accumulation of liquid water generated at the CL. Therefore, the liquid water accumulations observed by the neutron imaging (Figs. 4-7(b) and (e)) are expected to be influenced by the water absorbed at CLs with different catalysts.

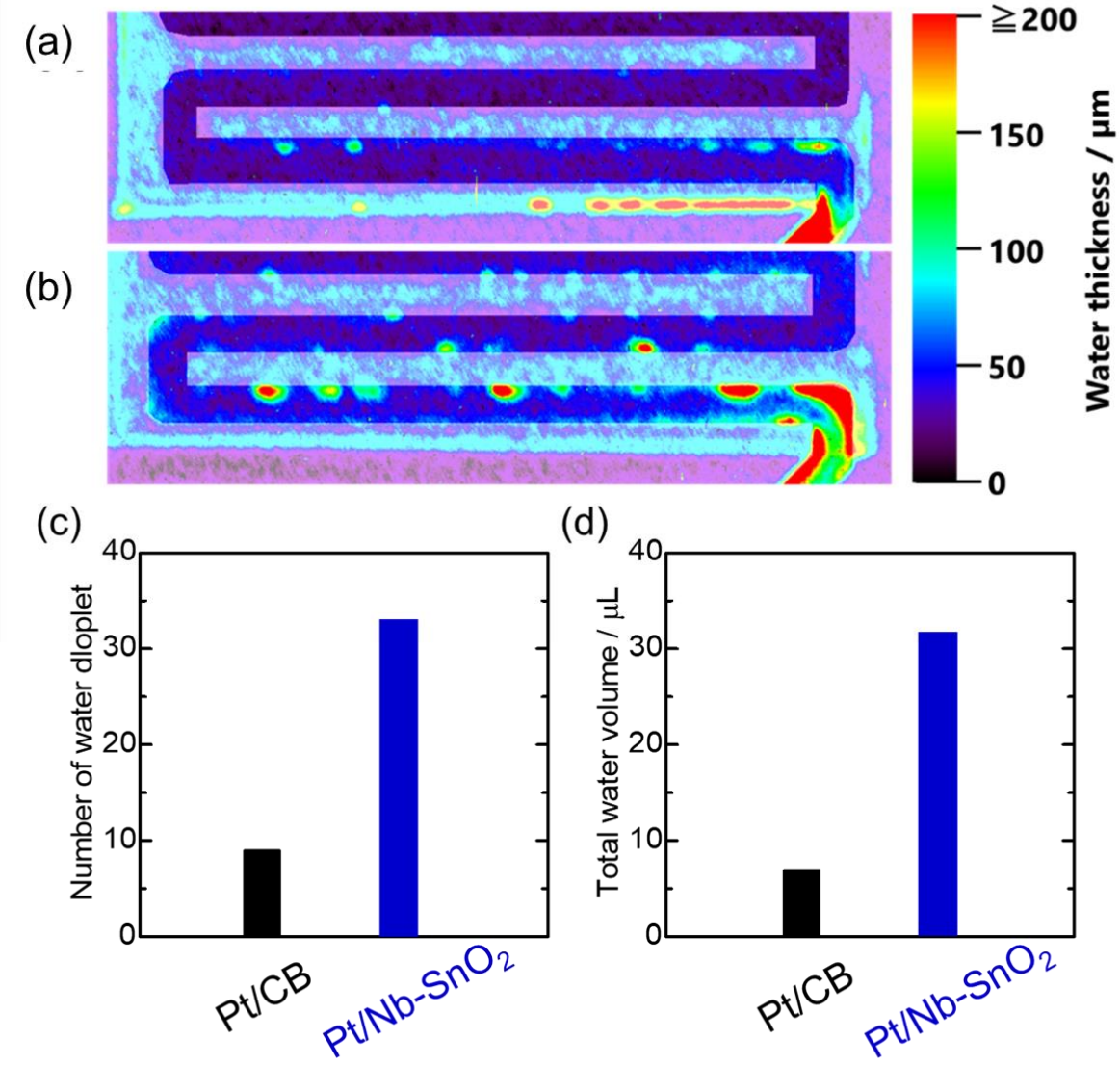

Fig. 4-8 Enlarged neutron images near the outlet using Pt/CB (a) and Pt/Nb-SnO_2 (b) at 0.5 A cm^{-2}, 80°C, and 80% RH. Water thickness was indicated by the color bar. Number of water droplets (c) and total water volume (d).

At 0.1 A cm^{-2}, the water droplets were not observed in either cell. Instead, uniform water distributions with a thickness of 16-18 μm for Pt/CB and 18-20 μm for Pt/Nb-SnO_2. Although the thickness was calculated to be slightly larger for Pt/Nb-SnO_2, the difference was not significant.

Line profiles along the centers of the flow channels from the inlet (0 mm) to the outlet (211 mm) with Pt/CB and Pt/Nb-SnO_2 are shown in Figs. 4-9(a) and (b), respectively. Trendlines of line plots derived from Figs. 4-9(a) and (b) are shown in Figs. 4-9(c) and (d), respectively. As shown in Fig. 4-9(c), the water thickness with Pt/CB was 16 μm at both 0.1 and 0.5 A cm^{-2} near the inlet. At 0.1 A cm^{-2}, the water thickness gradually increased to 19 μm near the outlet. At 0.5 A cm^{-2}, water thickness gradually increased to 30 μm at the outlet along the flow channel length. With Pt/Nb-SnO_2, the water thickness was 18 μm at both 0.1 and 0.5 A cm^{-2} near the inlet (Fig. 4-9(d)). At 0.1 A cm^{-2}, the water thickness gradually increased to 20 μm near the outlet. At 0.5 A cm^{-2}, water thickness increased to 42 μm along the flow channel length, much larger than that with Pt/CB.

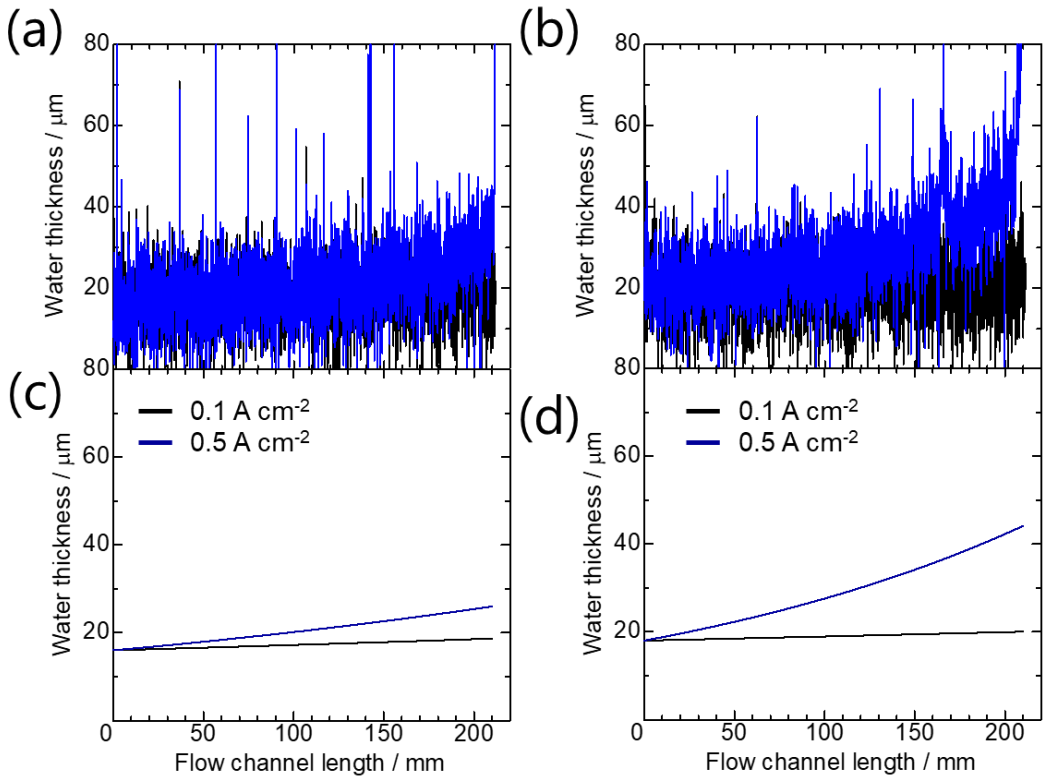

Fig. 4-9 Water thickness along the flow channel lengths with Pt/CB (a) and Pt/Nb-SnO_2 (b). Trendlines of line plots derived from Figs. 4-9(a) and (b) are shown in (c) and (d), respectively.

The ribs were numbered 1-9 from the inlet as shown in Fig. 4-10. Figures 4-11(a) and (b) show the average water thickness under the ribs with Pt/CB and Pt/Nb-SnO_2, respectively. At 0.1 A cm^{-2}, the average water thickness under the ribs was uniform around 18-20 μm with Pt/CB and Pt/Nb-SnO_2. At 0.5 A cm^{-2}, the average water thickness gradually increased along the channel length up to 51 and 68 μm with Pt/CB and Pt/Nb-SnO_2, respectively. In the case of Pt/Nb-SnO_2, water rapidly accumulated under the rib from rib 3 (Fig. 4-11(b)).

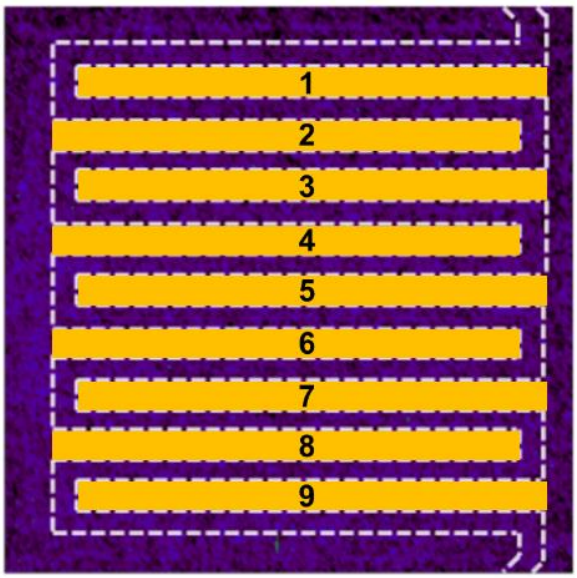

Fig. 4-10 Rib numbers.

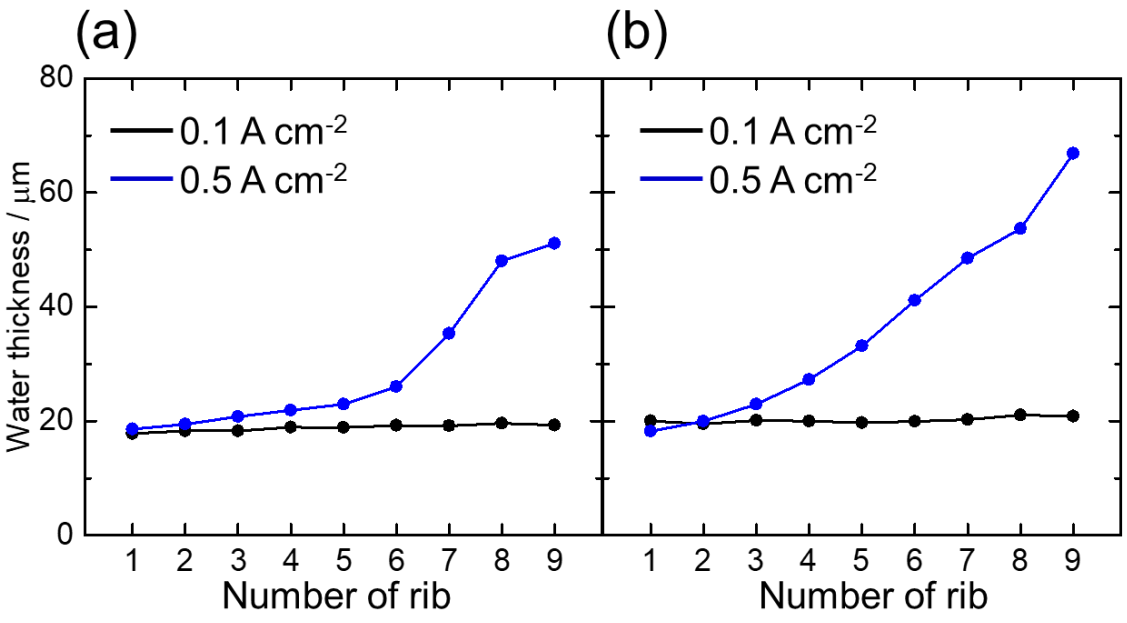

Fig. 4-11 Average water amount under the ribs of (a) Pt/CB and (b) Pt/Nb-SnO_2 cathode catalyst PEMFC.

As seen by the neutron imaging, water accumulated more with Pt/Nb-SnO_2 than with Pt/CB at 0.5 A cm^{-2} both under the flow channels and the ribs. The accumulated liquid water should have gathered to form droplets on the border between the flow channel and the rib. As shown by the CVs (Fig. 4-3) and the TEM images (Fig. 4-4), the catalyst surfaces were not completely covered with Nafion. Therefore, the larger hydrophilicity of the surface of Pt/Nb-SnO_2 (Fig. 4-2) should much contribute to the water in the catalyst layer. The smaller pore volume of the Pt/Nb-SnO_2 CL (Fig. 4-5) had an additional contribution to the larger water accumulation. The oxygen transport should be inhibited by the water accumulation in the CL, which lowered the I-V performance with Pt/Nb-SnO_2 (Fig. 4-1).

4.4 Conclusion

In this chapter, the water distributions inside the MEA using different support materials were imaged by the neutron beams at 0.1 A cm^{-2}, the water thicknesses under the ribs and flow channels in MEAs using both Pt/CB and Pt/Nb-SnO_2 were homogeneous. As increasing current density, liquid water more accumulated inside cells. More water droplets were observed on the flow channel walls with Pt/Nb-SnO_2. The accumulation of water in the CL of Pt/Nb-SnO_2 was explained by the exposure of the support surface, the hydrophilicity of the Nb-SnO_2 surface, and the smaller pore volume of the CL. The excess water in the CL should be the reason for the water accumulation in the flow channel.

The different water management must be employed for the cell with Pt/Nb-SnO_2 as the cathode catalyst.

References

[1] T. Yoda, H. Uchida, M. Watanabe, Electrochim. Acta 52 (2007) 5997–6005.

[2] T. Aoki, A. Matsunaga, Y. Ogami, A. Maekawa, S. Mitsushima, K. Ota, H. Nishikawa, J. Power Sources 195 (2010) 2182–2188.

[3] K. Kinoshita, J.A.S. Bett, Carbon 11 (1973) 403–411.

[4] J. Willsau, J. Heitbaum, J. Electroanal. Chem. 161 (1984) 93–101.

[5] Y. Shao, G. Yin, Y. Gao, J. Power Sources 171 (2007) 558–566.

[6] S. C. Ball, S. L. Hudson, D. Thompsett, B. Theobald, J. Power Sources 171 (2007) 18–25.

[7] S. Takenaka, H. Matsumori, H. Matsune, E. Tanabe, M. Kishida, J. Electrochem. Soc. 155 (2008) B929–B929.

[8] G. A. Gruver, R. F. Pascoe, H. R. Kunz, J. Electrochem. Soc. 127 (1980) 1219–1224.

[9] Y. Senoo, K. Kakinuma, M. Uchida, H. Uchida, S. Dekia, M. Watanabe, RSC Adv., 4 (2014) 32180.

[10] Y. Chino, K. Taniguchi, Y. Senoo, K. Kakinuma, M. Hara, M. Watanabe, M. Uchida, J. Electrochem. Soc. 162(2015) F736–F743.

[11] Y. Chino, K. Kakinuma, D. A. Tryk, M. Watanabe, M. Uchida, J. Electrochem. Soc. 163 (2016) F97–F105.

[12] K. Kakinuma, Y. Chino, Y. Senoo, M. Uchida, T. Kamino, H. Uchida, S. Deki, M. Watanabe, Electrochim. Acta 110 (2013) 316–324.

[13] T. Shinohara, T. Kai, K. Oikawa, T. Nakatani, M. Segawa, K. Hiroi, Y. Su, M. Ooi, M. Harada, H. Iikura, H. Hayashida, J. D. Parker, Y. Matsumoto, H. Sato, Y. Kiyanagi, Rev. Sci. Instrum. 91 (2020) 043302.

[14] T. Ito, U. Matsuwaki, Y. Otsuka, M. Hatta, K. Hayakawa, K. Matsutani, T. Tada, H. Jinnai, Electrochemistry 79 (2011) 374–376.

[15] K. Kakinuma, R. Kobayashi, A. Iiyama, M. Uchida, J. Electrochem. Soc. 165 (2018) J3083–J3089.

[16] S. J. Peighambardousta, S. Rowshanzamira, M. Amjadi, Int. J. Hydrog. Energy 35 (2010) 9349–9384.

[17] X. G. Yang, F. Y. Zhang, A. L. Lubawy, C. Y. Wang, J. Electrochem. Soc. 7 (2004) A408–A411.

Chapter 5

General Conclusions

5.1 Summary of the thesis

In Chapter 1, the current situations/problems of energy and their solutions are first explained. Conventional power generation methods emit CO_2, a greenhouse gas. The promotion of renewable energies, such as hydropower, wind power, solar power, and geothermal power, have been accelerated. The storage system of energy in the society is also needed. The rechargeable battery is widely used, but for large scale and long-term storage of electricity, battery is not suitable. To compensate the use of batteries, hydrogen has been attracting attention as a fuel in decades.

In Chapter 2, the I-V performances under the low $\Phi(O_2)$ of 3, 5, and 10% in air simulating oxygen starvation were reported to abruptly decrease at 0.6 V. The decreases of $p(O_2)$ along the flow channel length at lower U_{O2} were similar at $\Phi(O_2)$ = 10, 5 and 3% but started to differ at U_{O2} > 91%. The low $\Phi(O_2)$ and high U_{O2} lead to a significant decrease of $p(O_2)$ near the outlet. During power generation, the $p(O_2)$ distribution on the GDL surface at the cathode was directly visualized with a nondestructive real-time/space visualization system. At very low $\Phi(O_2)$ and very high U_{O2}, there was no oxygen present on the GDL surface near the gas outlet possibly because of a generation of hydrogen at the cathode due to the local low voltage. Direct oxygen consumption by the hydrogen evolution reaction at the cathode was proposed. The existence of both hydrogen and oxygen at the same electrode surface could lead to the degradation of catalyst and support, and in the worst-case scenario to explosion. The results reported in Chapter 2 should be important for the stable and safe operation, as well as for the durability.

In Chapter 3, new oscillation phenomena were reported, where the cell voltage oscillated

periodically under a constant-current operation. The differential pressure between the cathode inlet and outlet was 0 kPa during the oscillation, very different from the cell voltage fluctuation previously reported to be synchronized with the plugging of flow channels. The amplitude and period of this oscillation were approximately 20 mV and 2 s, respectively, shorter than those previously reported. The period and amplitude decreased as the air flow increased. The period became a volcano shape when the current density increased, whereas the amplitude monotonously decreased. An *operando* system was developed for detecting $p(O_2)$ using multiple optical probes. $p(O_2)$ during the oscillation synchronized with the cell voltage. In particular, the amplitude of the oscillation of $p(O_2)$ was the largest under the rib near the outlet. During the oscillation, the generated water was proposed to increase and accumulate in the CL, accordingly inhibiting the transport and reduction reaction of oxygen. This oscillation could be more pronounced at higher current density. The oscillation phenomena are likely to be more pronounced in the future operation of PEMFCs at high current densities. The mechanisms proposed in this paper could be applied to the water management in the CL and the GDL, as well as for optimizing the PEMFC operation.

As describe in Chapter 1, improving the durability of catalyst is still mandatory to reduce cost of PEMFC stacks. Platinum-based catalysts supported on carbon generally used undergo degradation under the operating condition of low pH, high humidity, and high potential. One of the degradation reactions is corrosion of the carbon support by oxidation resulting from the thermodynamic instability, which becomes an impediment to long-term durability. The corrosion also accelerates the aggregation of Pt particles on carbon support and/or actual loss from the support, thereby decreasing the effective Pt content. For preventing the corrosion of support, Pt/Nb-SnO_2 was synthesized. In Chapter 4, the I-V

performance of a cell with Pt/Nb-SnO_2 at the cathode was reported to be lower than that with Pt/CB. The water distributions inside PEMFCs with Pt/CB and Pt/Nb-SnO_2 were visualized by neutron beam. With Pt/Nb-SnO_2, the amount of liquid water accumulated inside the PEMFC was found larger than with Pt/CB, explained by the hydrophilicity of the surface of Nb-SnO_2. Therefore, water must be managed with new operating conditions, such as cell temperature, pressure, and relative humidity, optimized for Pt/Nb-SnO_2. The cell configuration must be optimized, too, for the catalysts using new supports.

By analyzing mass transport, the mechanisms of phenomena inside PEMFC were understood. Following are the proposals:

On oxygen starvation

Forced shutdown at low-potential regions by dividing the current collector plates.

To prevent hydrogen evolution at the low potential region of the cathode, the current collector plate should be subdivided, and the current circuit at the low potential region be closed, which will stop the proto-electron transport.

On voltage oscillation

Development and optimization of materials for the GDLs and MPLs.

Under the high current-density operations, liquid water accumulates in the CL and the oscillation described in this thesis is likely to occur. Toward the higher current-density operation, the importance of the GDLs for efficiently removing water from the CL was demonstrated.

On water management with ceramics supports.

Improvement of the structure of CLs and binders.

Liquid water generation in the CL was affected by the characteristics of the support. In order to solve this problem, he structure of the catalyst layer, such as binder coverage and

porosity by using spray methods and ink adjustment techniques are necessary to optimize the water management.

The *operando* analytical method played an important role in elucidating the various mechanisms inside the PEMFCs. It is an important factor to accelerate the development of PEMFCs in the future.

5.2 Feasibility & Social significance

For wider use of PEMFC, reducing the stack cost and improving the system durability are still important. The multiple components of PEMFC factors are shown in Fig. 5-1 [5]. The ultimate targeted cost and durability of a PEMFC system are $30 / kW and 8000 h, respectively. However, system durability is still ca. 4,000 h in 2019. In Fig. 5-2, the PEMFC stack cost breakdown is shown [5]. Reducing the cost of catalyst and application, 53% in the stack cost breakdown, is effective for reducing the PEMFC price. In Fig. 5-3, the degradation rates of the PEMFC fuel cell performance caused by different operation conditions are summarized. The catalyst degradations caused by the load changing and start-stop are 57 and 33%, respectively.

To improve the power generation performance and durability of fuel cells, unclear abnormal phenomena mechanisms during power generation must be elucidated and eliminated. For the analyses, I have developed *operando* systems designed to analyze those phenomena. Suitable PEMFCs were newly prepared, but in the manner of maintaining the performance of power generation by keeping adequate sizes and structures of the cells. Three phenomena during the power generation were studied as described in Chapter 1.

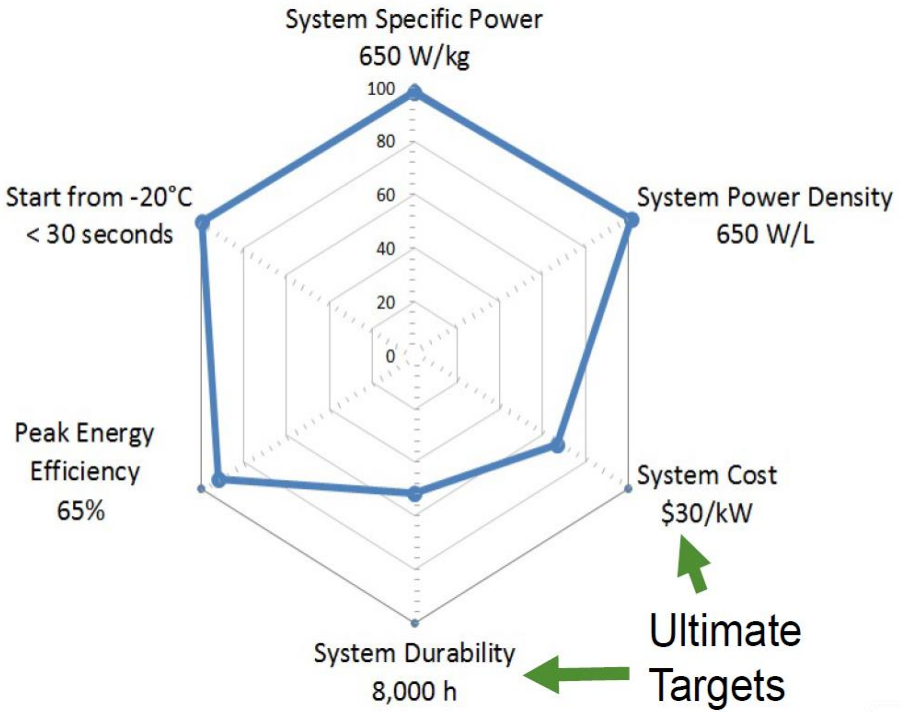

Fig. 5-1 Multiple components to meet targets by DOE Hydrogen and Fuel Cells Program Record [5].

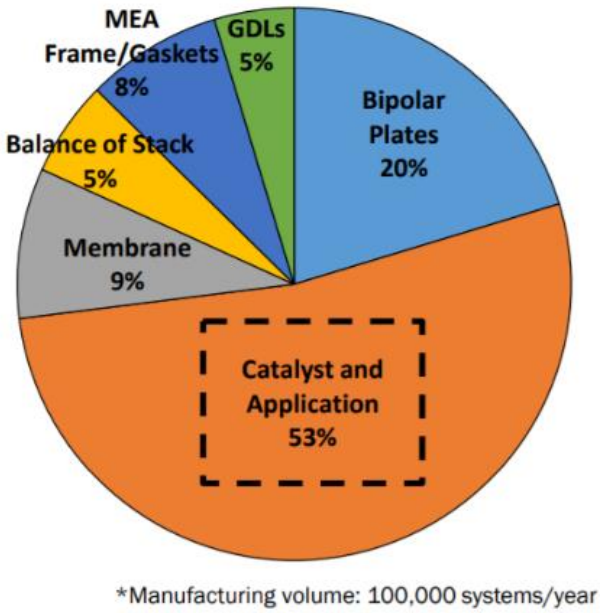

Fig. 5-2 PEMFC stack cost breakdown for manufacturing volume at 100000 system/year reported by DOE Hydrogen and Fuel Cells Program Record [5].

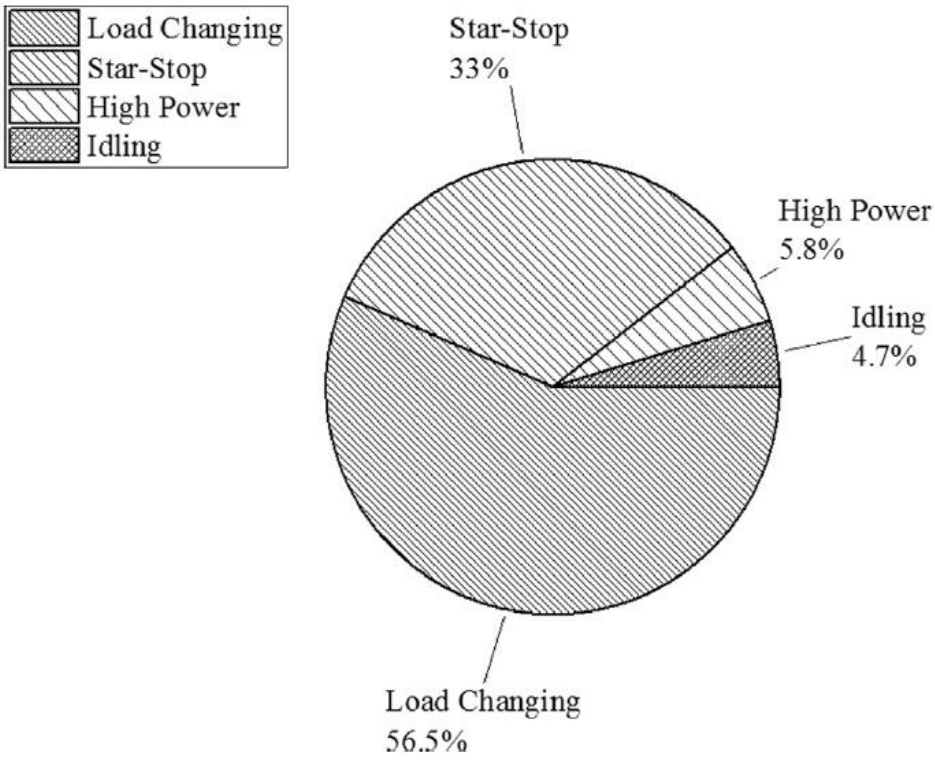

Fig. 5-3 Degradation rates of PEMFC fuel cell performance caused by different operation conditions [6, 7]

As describe in Chapters 2 and 3, an oxygen starvation and oscillation phenomena lead to these degradations. Generally, the oxygen starvation can be easily recovered by supplying enough air to the cathode, when an overall oxygen starvation is observed. In Chapter 2, the local oxygen starvation is also explained caused by the accumulation of excess water. In this case, the oxygen starvation is difficult to be recovered simply by increasing the air flow, because water accumulates where the feed gas flux is low. To solve this local oxygen starvation, a partially forced closed electric circuit or the use of highly tolerant catalysts are used. As described in Chapter 3, the amplitude of a voltage oscillation became larger as increasing the current density. At a high current density, the cell voltage during the oscillation was similar to that during the load change. The cause

of the oscillation was explained as the accumulation of water inside the CL. Therefore, the oscillation should be avoided by improving the water removal from the CL by changing the operating condition or components such as high gas flow flux, optimizing the flow channel structure.

In Chapter 4, the water distributions inside MEAs with Pt/Nb-SnO_2 and Pt/CB at the cathode were imaged during power generation by neutron beam to elucidate the low I-V performance with Pt/Nb-SnO_2 at the cathode. As shown in Fig. 5-3, the start-stop processes occupy 33% of the total degradation. From the durability of I-V performance by the start-stop processes [8], the degradation by start-stop cycle might be decreased to ca. 4.4%.

My research strategy consisted of four steps: 1. phenomenological study, 2. development of analytical system, 3. *operando* measurements, 4. modeling. This strategy was proved to be successful and useful. For wider use of PEMFCs, the developments of new materials and new cells are very important. The *operando* analyses during operation, three examples of which have been demonstrated in the thesis, are important, too, and are expected to be more crucial in the future. I believe that my analytical strategy is useful not only for academic researches but also to the industrial applications.

References

[1] Y. Bao, H. Ming, J. Automot. Safe Energy 02 (2011) 91–100.

[2] Q. Shen, M. Hou, X. Yan, D. Liang, Z. Zang, L. Hao, Z. Shao, Z. Hou, P. Ming, B. Yi, J. Power Sources 179 (2008) 292–296.

[3] C. Wang, S. Wang, J. Zhang, L. Jianqui, J. Wang, M. Ouyang, Prog Chem 27 (2015) 424–435.

[4] G. Mousa, J. DeVaal, F. Golnaraghi, Int. J. Hydrogen Energy 39 (2014) 21154–21164.

[5] DOE Hydrogen and Fuel Cells Program Record, published by U. S. department energy. https://www.hydrogen.energy.gov/pdfs/review19/plenary_fuel_cell_papageorgopoulos_2019.pdf

[6] H. Chena, X. Zhao, T. Zhang, P. Pei, Energy Convers. Manag. 182 (2019) 282–298.

[7] P. Pei, Q. Chang, T Tang, 33 (2008) 3829–3836.

[8] Y. Chino, K. Taniguchi, Y. Senoo, K. Kakinuma, M. Hara, M. Watanabe, M. Uchida, J. Electrochem. Soc. 162 (2015) F736–F743.

List of publications

1. **Visualization of the oxygen partial pressure in a proton exchange membrane fuel cell during cell operation with low oxygen concentrations.**

   Y. Kakizawa, C. L. Schreiber, S. Takamuku, M. Uchida, A. Iiyama, and J. Inukai, Journal of Power Sources 483 (2021) 229193.

2. **Oscillation mechanism in polymer electrolyte membrane fuel cell studied by *operando* monitoring of oxygen partial pressure using optical probes.**

   Y. Kakizawa, T. Kobayashi, M. Uchida, T. Ohno, T. Suga, M. Teranishi, M. Yoneda, T Saiki, H. Nishide, M. Watanabe, A. Iiyama, J. Inukai, J. Surf. Finish. Soc. Jpn. 72 (2021) in print in April 2021.

Meeting Abstracts

1. **Oxygen partial pressures inside gas diffusion layer of polymer electrolyte fuel cell during power generation.**

   ○Y. Kakizawa, K. Takanohashi, M. Ihara, Y. Nagumo, T. Ohno, L. A. Nicolas, F. Buechi, A. Iiyama, J. Inukai, 67th Annual Meeting of the International Society of Electrochemistry (ISE), (s-07-083), the Hague, the Netherlands, August 21st-26th, 2016.

2. **Oxygen partial pressures inside gas diffusion layer of polymer electrolyte fuel cell during power generation measured with multiple optical probes.**

   ○Y. Kakizawa, K. Takanohashi, M. Ihara, Y. Nagumo, T. Ohno, L. A. Nicolas, F. Buechi, A. Iiyama, J. Inukai, The 5th International Seminar for Special Doctoral Program 'Green Energy Conversion Science and Technology', (P78), Koumi, Nagano, Japan, August 31st - September 2nd, 2016.

3. **Optical-probe measurements of oxygen partial pressure at surface of and inside gas diffusion layer of polymer electrolyte fuel cell during power generation.**

   ○Y. Kakizawa, K. Takanohashi, M. Aoki, A. Iiyama, J. Inukai, 36th Meeting of Surface Science Society of Japan, (1Ep09S), Nagoya, Aichi, Japan, November 29th - December 1st, 2016.

4. **Oscillation phenomena inside PEFC analyzed by *operando* oxygen-partial-pressure measurements using optical probes.**

   ○Y. Kakizawa, K. Takanohashi, M. Aoki, F. N. Büchi, A. Iiyama, J. Inukai, 84th Meeting of Electrochemical Society of Japan, (1D32) Hachioji, Tokyo, Japan, March 25th-27th, 2017.

5. **Oscillations of cell voltage and oxygen partial pressures of PEFC analyzed by using optical probes.**

   ○Y. Kakizawa, K. Takanohashi, A. N. Lamibrac, M. Aoki, F. N. Büchi, A. Iiyama, J. Inukai, 68th Annual Meeting of the International Society of Electrochemistry (ISE), Providence, Rhode Island, USA, August 27th - September 1st, 2017.

6. **Synchronized oscillations of cell voltage and oxygen partial pressure inside membrane-electrode assembly of polymer electrolyte fuel cell in operation.**

○Y. Kakizawa, A. Iiyama, J. Inukai, The 6th International Seminar for Special Doctoral Program 'Green Energy Conversion Science and Technology', (P38), Koumi, Nagano, Japan, September 13rd-15th, 2017.

7. **The road to the ultimate energy society.**

○Y. Kakizawa, A. Iiyama, J. Inukai, Program for Leading Graduate Schools Forum 2017, Nagoya, Aichi, Japan, October 20th-21st, 2017.

8. ***Operando* monitoring of the oxygen partial pressures inside the gas diffusion layer of a running polymer electrolyte fuel cell using optical probes.**

○Y. Kakizawa, A. Iiyama, J. Inukai, International Symposium on Novel Energy Nanomaterials, Catalysts and Surfaces for Future Earth, (O2P-30) Chofu, Tokyo, Japan, October 28th-30th, 2017.

9. **Development of analytical system for distribution of oxygen partial pressure using optical probes and application to fuel cell researches**

Y. Kakizawa, A. Iiyama, ○J. Inukai, 37th Meeting of Surface Science Society of Japan, (3Aa06), Yokohama, Kanagawa, Japan, August 17th-19th, 2017.

10. 発電中の固体高分子形燃料電池触媒層界面で生じる振動現象の解析

○Y. Kakizawa, A. Iiyama, J. Inukai, 137th Meeting of Surface Finishing Society of Japan, (P-39), Toyosu, Tokyo, Japan, March 12nd-13rd, 2018.

11. **Voltage oscillation analyzed by *operando* monitoring of oxygen partial pressure inside running polymer electrolyte fuel cell.**

○Y. Kakizawa, A. Iiyama, J. Inukai, Grand Renewable Energy 2018 International Conference and Exhibition, (a91098) Yokohama, Kanagawa, Japan, June 17th-22nd, 2018.

12. **Voltage oscillation during power generation of PEFC synchronized with oxygen partial pressure.**

○Y. Kakizawa, A. Iiyama, J. Inukai, The 8th International Seminar for Special Doctoral Program 'Green Energy Conversion Science and Technology', (P47), August 2018, Kofu, Yamanashi, Japan, August 22nd-23rd, 2018.

13. **Voltage oscillation analyzed by *operando* monitoring system of oxygen partial pressure using multiple optical probes positioned inside running PEFC.**

○Y. Kakizawa, A. Iiyama, J. Inukai, The 8th International Fuel Cell Workshop 2018 – PEFCs: from Basic Science to Application –, Kofu, Yamanashi, Japan, August 23rd-24th, 2018.

14. **Voltage oscillation in running PEFCs Analyzed by monitoring oxygen partial pressure in GDLs**

Y. Kakizawa, A. Iiyama, ○J. Inukai, CARISMA2019, Duisburg, Germany, August 27th-30th, 2019.

15. **Neutron imaging of water inside membrane-electrode assembly of polymer electrolyte fuel cell.**

○Y. Kakizawa, H. Hayashida, A. Iiyama, J. Inukai, International Workshop on Green Energy Conversion, September 2019, Kofu, Yamanashi, Japan, October 24th-25th, 2019.

16. **Voltage oscillation in PEFC during power generation coupled with oxygen partial pressure in GDLs.**

Y. Kakizawa, ○J. Inukai, The 20th National Electrochemistry Meeting of the Electrochemical Society of China, Changsha, China, October 26th-28th, 2019.

17. **Imaging and quantification of water inside membrane-electrode assembly of polymer electrolyte fuel cell during power generation by use of neutron beam.**

○Y. Kakizawa, H. Hayashida, K. Suda, T. Kawamoto, K. Kakinuma, M. Uchida, A. Iiyama, J. Inukai, ECS PRiME 2020 online meeting, October 4th-9th, 2020.

Awards

1. **Presentation Encouragement Award (Students' Division)**

   "Optical-probe measurements of oxygen partial pressure at surface of and inside gas diffusion layer of polymer electrolyte fuel cell during power generation."

   ○Y. Kakizawa, K. Takanohashi, M. Aoki, A. Iiyama, J. Inukai, 36th Meeting of Surface Science Society of Japan, (1Ep09S), Nagoya, Aichi, Japan, November 29th - December 1st, 2016.

2. **Best Poster Presentation Award**

   Voltage oscillation analyzed by *operando* monitoring of oxygen partial pressure inside running polymer electrolyte fuel cell.

   ○Y. Kakizawa, A. Iiyama, J. Inukai, Grand Renewable Energy 2018 International Conference and Exhibition, (a91098) Yokohama, Kanagawa, Japan, June 17th-22nd, 2018.

3. **ISE Poster Award**

   Voltage oscillation analyzed by *operando* monitoring system of oxygen partial pressure using multiple optical probes positioned inside running PEFC.

   ○Y. Kakizawa, A. Iiyama, J. Inukai, The 8th International Fuel Cell Workshop 2018 – PEFCs: from Basic Science to Application –, Kofu, Yamanashi, Japan, August 23rd-24th, 2018.

Acknowledgments

For this thesis, researches have been carried out at Fuel Cell Nanomaterial Center, Clean Energy Center, and Interdisciplinary Graduate School of Medicine, Engineering, and Agricultural Sciences in University of Yamanashi.

The numerical simulations of the mass fraction of oxygen inside a GDL were performed by Mizuho Information and Research Institute, Inc.

The X-ray CT experiments were performed under Proposal 2016A1759 at BL46XU of SPring-8 with the approval of the Japan Synchrotron Radiation Research Institute (JASRI).

The neutron imaging was performed under Proposals 2019A0217 and 2020A0166 of J-PARC.

I would like to express my great gratitude to **Professor Junji Inukai** of University of Yamanashi, academic supervisor of this work, for his continuous guidance, in valuable suggestions, and warm encouragements throughout this work. I'm proud that I have worked with him.

I would like to express sincere thanks to **Professor Hiroshi Irie, Professor Yanagi, Associate Professor Hideyuki Shinmori** of University of Yamanasshi and **Professor Shigenori Mitsushima** of Yokohama National University for their cooperation in reviewing my Ph.D. thesis.

I would like to express sincere thanks to **Professor Makoto Uchida** and **Professor Katsuyoshi Kakinuma** of the University of Yamanashi for his helpful suggestions, excellent technical advices and continuous guidance to this work.

I sincerely appreciate **Professor Hiroyuki Uchida** of University of Yamanashi for his valuable discussions and encouragements.

I would like to express my sincere graduate to **Professor Akihiro Iiyama**, **Professor Kenji Miyatake**, **Professor Kazuhiro Higashiyama**, **Professor Toshihiro Miyao, Professor Donald Alexander Tryk**, **Professor Tomio Omata**, **Professor Manuel Eduardo Brito**, **Associate Professor Shinji Noahara, Associate Professor Junppei Miyake**, **Associate Professor Mitsuru Wakisaka**, **Associate Professor Hiroshi Yano**, **Associate Professor Hanako Nishino** of University of Yamanashi, for valuable support and professional guidance.

I would like to express great acknowledgements to **Mr. Yuzo Nagumo**, **Mr.Takashi Ono**, **Mr. Masahiro Ihara** of Shimadzu Corp. for their valuable discussion and technical advices.

I am grateful to **Dr. Hideto Imai**, **Dr. Masashi Matsumoto** and **all of members of Nissan arc Corp.** for their kindly support in my Internship.

I am grateful to **Dr. Felix N. Büchi**, **Dr. Jens Eller**, **Mr. Adrian Mularczyk**, **Dr. Salvatore De Angelis**, **Mr. Martin Ammann**, **Mr. Stephan Michael Tschumi**, **Mr.**

Yen-Chun Chen, **Mr. Hong Xu**, **Mr. Tobias Schuler**, **Mr. Christoph Paul Csoklich**, **Mr. Christian Peter**, **Mr. Arnaud Schuller**, **Mr. Michael Striednig**, **Mr. Thomas Gloor**, **Ms. Cordelia Gloor** and **all of members of Paul Scherrer Institute** for their kindly support in Switzerland.

I am grateful to **Dr. Shogo Takamuku** of BOSCH Corp., **Mr. Jonas Gutmann and Mr. Christopher Lion Schreiber** of Internship students from BOSCH Corp. for their valuable discussion and encouragements as research collaborator.

My deep appreciate is expressed to **Dr. Katsuya Nagase** of Takahata Precision Co., Ltd, **Dr. Takenao Shinohara** of Japan Atomic Energy Agency J-PARC Center, **Dr. Hirotoshi Hayashida** of Comprehensive Research Organization for Science and Society, **Dr. Norifumi Yamada** of Institute of Materials Structure Science, High Energy Accelerator Research Organizer, **Dr. Kentaro Kajiwara** of Japan Synchrotron Radiation Research Institute for experimental support and constructive discussion.

I am grateful to **Ms. Mika Kodama, Ms. Setsuko Mori** and **Mr. Takayuki Asakawa** of University of Yamanashi for assistance of TEM measurements, **Mr. Tetsuro Tano** of University of Yamanashi for catalyst synthesis.

I am also grateful to **Ms. Nozomi Toyoda**, **Ms. Tomomi Hashizume**, **Ms. Kaori Ichinose** and **all staffs of Fuel Cell Nanomaterial Center and Clean Energy Research Center** for kind support and help.

I am grateful to **Dr. Teppei Kawamoto**, **Dr. Hiromichi Nishiyama**, **Dr. Kohei Suda, Dr. Kazuhiro Takanohashi**, **Mr. Takashi Kobayashi**, **Mr. Ichiro Nagata**, **Mr. Takeshi Kawamura**, **Mr. Yuto Shirase Ms. Fumika Ishihara** and **Mr. Toshiro Iwataki** of Inukai laboratory for their strong assistances to my study.

I would like to thank **Dr. Takashi Mochizuki, Dr. Yuji Chino, Dr. Morio Chiwata, Dr. Yuya Yamashita, Dr. Kento Takahashi, Dr. Kazuki Shimura, Dr. Yoshiyuki Ogihara, Dr. Hideaki Ono, Dr. Manai Shimada, Dr. Ryosuke Nishikawa, Dr. Ryo Shimizu, Dr. Hideaki Ohno, Mr. Takumi Kuroda, Mr. Shigefumi Shimada, Mr. Shota Miyashita, Mr. Ryunosuke Taki, Ms. Chie Arata, Mr. Ikkei Arima, Mr. Jun Fukasawa, Dr. Shun Kobayashi, Dr. Taro Kimura, Dr. Hosaka Ibuki, Mr. Yuma Shimizu, Mr. Seiya Kosaka, Mr. Naoki Hirayama, Mr. Shinya Hanyu Mr. Satoshi Ogawa, Ms. Honami Nishikawa, Mr. Toshiki Tanaka, Mr. Kanji Otsuji, Mr. Ryo Kobayashi, Mr. Shunsuke Ishikawa, Mr. Takahiro Matsumoto, Mr. Shinichiro Tsutsui, Mr. Takayuki Watanabe, Mr. Shuji Nakamura Mr. Shohei Asanuma, Mr, Yuki Miyamoto, Ms. Rutsu Tamura, Mr. Naoki Ogawa, Mr. Takuma Hashimoto** and **Mr. Takafumi Sawano** for their helpful advises and valuable discussion.

I would like to thank my university classmate, **Mr. Koki Ueno, Mr. Kohei Uyama, Mr. Yuta Oishi, Mr. Koki Kubota, Mr. Tsugeru Sano, Ms. Mizuki Hayashi, Ms. Reika Oida, Ms. Yuka Furuhashi** and **Ms. Risa Ochiai** for giving me happy day.

I would like to offer my special thanks to **Mr. Shiino Keishuke, Mr. Ryo Shirasaka and Ms. Mizuki Ozawa** for giving me enjoyable working day.

I would like to thank deeply all members of Clean Energy Research Center, Fuel Cell Nanomaterials Center, Special Doctoral Program for Green Energy Conversion Science and Technology and Power Energy Professionals Waseda University Graduate Program for their kind helps and supports.

Finally, I greatly appreciate the support of my family, **Toshimitsu Kakizawa, Ritsuko Kakizawa, Hiroaki Kakizawa, Hatsue Kakizawa.**

Yu Kakizawa

March, 2021